The Investigation of Haliotis Rufescens (Red Abalone): Mesolayer Growth & Mechanical Behavior

by

Anqi Zhang

A dissertation submitted to the Graduate Faculty of
Auburn University
in partial fulfillment of the
requirements for the Degree of
Doctor of Philosophy

Auburn, Alabama
Dec 16, 2017

Key Words: Haliotis Rufescens, Nacre, Mesolayer, Growth, Nanoindentation test

Approved by

Dr. Bart C. Prorok, Chair, Professor of Material Engineering
Dr. Ruel A. Overfelt, Professor of Material Engineering
Dr. Dong-Joo Kim, Professor of Material Engineering
Dr. Jeffrey C. Suhling, Professor of Mechanical Engineering
Dr. Robert L. Jackson, Professor of Mechanical Engineering

Abstract

Self-assembly is a popular bottom-up process which results in highly-ordered and fine structures in micro- or nano-scale. The special structures produced through the self-assembly are always related to some unique and outstanding properties. Abundant research has been performed to aid in figuring out ideal ways to produce these materials for industrial applications. In the biological world, many creatures develop a self-assembly process in some of their physiological behaviors through millions of years of evolution which could inspire us with innovate ideas to produce the special and specific structure. The nacre of the abalone shell is on such example. Thus, studies of abalone nacre are helpful in learning about the design of such amazing structures, how they are formed, and the mechanical properties they possess.

Nacre, which is also called “mother of pearl”, is an extremely important part of abalone’s shell. With the self-assembly produced structure, which is constructed from aragonite tablets connected by organic thin films, the abalone nacre demonstrates fascinating toughness. While the tidy “brick-wall” structure provides the main body of the nacre, there exists another structure in the nacre which shows obvious differences and appears throughout the nacre, especially in shells of abalone that grow in the seas (the wild abalone). It is called the mesolayer and it can be divided into three separate layers: prismatic layer, organic layer, and columnar layer. Each of them shows their own individual elastic properties. Though there has been much research performed which focuses on the tablets which make up the nacre, very limited attention has been paid to the mesolayer.

The abalone creates a confined space for itself with its shell which it is attached to by a portion of its tissue known as the mantle. Abalone's nacre grows in the colloidal mucus secreted by the abalone itself in that confined space. That colloidal mucus provides the self-assembly nacre growth with an isolated and complicated environment and will ultimately act as the organic matrix in the nacre. As it is hard to observe the in-situ nacre growth, some methods were developed to assist with investigating this biomineralization process such as the Flat Pearl Method. This is the method applied in this research to determine how the seawater environment effects the mesolayer growth.

The California red abalones were purchased from an abalone farm and cultured in artificial seawater. The temperature, water quality, and food were well controlled to guarantee the abalones' health and that the nacre and mesolayer could grow normally. Temperature, pH, Mg^{2+}/Ca^{2+} ratio of the artificial seawater were parameters in need of control, based on literatures describing sea environment and sea creatures. Among these parameters, temperature and pH were controlled to allow the mesolayer to form. The mucus that the nacre grows from has also been observed out of abalone's body and in a mimicked confined space, and shows some interesting dendrite formation.

Elastic modulus is the main mechanical property of concern in this research. Nacre samples were tested with a nanoindenter. The main composition of nacre is calcium carbonate, which can be treated as a ceramic material, and shows excellent high toughness. Both the mesolayer and nacre were tested by the nanoindenter. For the mesolayer, each sublayer was tested to see the individual behaviors. For the nacre, when the test was applied on the nacre sample directly, crack formation began around the nanoindentation sites, which will influence the test result. Thus, the well developed Chen-Prorok method, which introduces a ductile metal film to the sample surface in order to avoid the substrate cracking, was applied in this research. As the nacre has a nano-scale architecture, a distinctive anisotropic modulus is present. The nacre samples tested in different

architecture orientations were included in thois research. The data was collected, analyzed, and presented, here in. Nanoindentations on several nacre samples with different architecture orientations were milled using focused ion beam in order to show the behavior beneath the surface. In addition, a bending experiment was applied on the nacre sample to see its behavior. With the combination of this information, reasonable assumptions were developed to explain the anisotropic modulus of the nacre structure. The nacre was also prepared into cantilever beams for additional testing. The results were compared with the nanoindentation test results. The cantilever project has recently just begun, and future progress is to be expected.

Although the nacre structure has been under investigation for quite some time, debates still exist as to how the nacre growth process functions and how the mechanical properties influence the structure. The work stated in this dissertation seeks to advance the knowledge of how the isolated biomineralization is effected by the outside environment and why this special architecture introduces a material with highly anisotropic mechanical properties.

Acknowledgments

Firstly, I would like to express my most sincerely thanks to Dr. Bart Prorok -- my committee chair and Ph.D program advisor. I came to Auburn as a young student who just got the Bachelor degree. Being fresh in the real research and started in a field that I was not familiar with, I was confused a lot and had hard time to completely join the research. Dr. Prorok's patience and guidance courage and support me so much that help me to grow up to a mature researcher today. Many thanks would also be given to my committee members Dr. Ruel Overfelt, Dr. Dong-Joo Kim, and Dr. Jeffrey C. Suhling and my outside-department dissertation reader Dr. Robert L. Jackson for offering me great research suggestions.

Thanks to the staffs in Materials Engineering. During my three years and a half research life, our technician Mr. Steven Moore offered me so much help. The instruments training, research items purchasing, and the preparation for my TA work, Mr. Steven Moore is always there for helping me. And, Ms. Cheryl Rhodes is so patient and kind that she is always there for helping me with solving problems.

I feel so lucky for being one member in Dr. Prorok's research group. So appreciate the help offered by Dr. MariAnne Sullivan and Dr. Naved Siddiqui, who are the senior Ph.D students in our research group when I first join in and are great engineers right now. I learned a lot from them. And, the new members in our group also do me a great favor. Anna Kate Osborn and Hayden Price are so patient for reading through and modifying the grammar mistakes in the draft of this dissertation for me.

I obtained such precious friendship which will stay with me for the rest of my life. Thanks to my dear friends: Dr. Yuanyuan Zhang, Dr. Jinglie Zhou, Fuling Yang, Dr. Jing Dai, Dr. Zhizhi Sheng, Dr. Honglong Wang, Liangxi Li, Xingxing Zhang, Cheng Chen, Songtao Du, Pu Deng, Yuzhe Sun, Wen Yang, Lang Zhou, Xin Sha, Yuzhe Liu, Hossein Talebinezhad, Yang Tong, etc. I will remember all the great days spent with you.

At last, my best and deepest love and thanks are sent to my parents and my fiancé. Although my parents are so far away from me, they are always the strongest support. Whenever I got confused, tired, or upset, they are there and ready to comfort me and hearten me. My fiancé, Yan Chen, is the one always be there with me and help me overcome difficulties. The best for me is that I could be the proud of them.

The three and a half years in Auburn teaches me and give me so much. This is the place that left me so many wonderful memories. I met the great advisor and professors, the amazing colleagues, the lovely friends, and my fiancé in Auburn. I am so lucky that Auburn University accepted me more than three years ago, and, I am so happy that I selected Auburn University. Auburn has been and will always be one important part of my life.

Table of Contents

List of Tables

List of Figures

Equation List

Equation 7. Et – The tested elastic modulus from nano-indenter, Ef' – Metal thin film's elastic modulus, Es – Substrate's elastic modulus, νs – Substrate's Poisson's ratio, νf – Metal thin film's Poisson's ratio, h' – The nanoindentation displacement over thin film thickness ratio. 83

$$\frac{1}{E_t}\frac{1}{(1 - e^{-\nu_s/h'})} \approx \frac{1}{E_f'} + \frac{1}{E_s}(0.5 - \frac{\nu_f}{\nu_s} + \frac{h'}{\nu_s})$$

Equation 8. θ = The tablet inclination angle, t = The average tablet thickness, d = The adjacent tablet line distance..... 94

$$\theta = \arcsin\frac{t}{d}$$

Equation 9. w – Beam deflection, P – Load, L – Complete beam length, A – Cross-section area, G – Shear modulus, E– Elastic modulus, I – The second moment of area, x – The location of the load (free end of the beam: x=0; constrained end of the beam: x = L), κ – The Timoshenko shear coefficient (κ =5/6 for the rectangular cross-section beam). 126

$$w(x) = \frac{P(L - x)}{\kappa AG} - \frac{Px}{2EI}\left(L^2 - \frac{x^2}{3}\right) + \frac{PL^3}{3EI}$$

Equation 10. s – The stiffness, L – Complete beam length, A – Cross-section area, G – Shear modulus, E– Elastic modulus, I – The second moment of area. 126

$$\frac{1}{s} = \frac{L}{\kappa AG} + \frac{L^3}{3EI}$$

List of Abbreviations

ACC	Amorphous Calcium Carbonate
BSE	Backscattered Electron
CSM	Continuous Stiffness Measurement
EDS	Energy Dispersive Spectrometry
FIB	Focused Ion Beam
OM	Optical Microscope
SE	Secondary Electron
SEM	Scanning Electron Microscopy
TEM	Transmission Electron Microscopy
XRD	X-Ray Diffraction

1. Introduction and Research Motivation

Haliotis Rufescens (Red Abalone) nacre has long been a focus of comprehensive investigation due to the distinct micro-structure it possesses. The excellent mechanical behavior of *Haliotis Rufescens* nacre is believed to be related to the unique structure.

In this dissertation, multiple directions of research based on this composite material are examined. The biomineralization process of nacre growth as well as the mechanical behavior is investigated.

Studies based on the *Haliotis Rufescens* nacre reveals the advantages of its unique structure. These analyses could provide a new method to control and improve the structure of composite materials, which possess an outstanding mechanical capacity.

The research stated in this dissertation is based on the California *Haliotis Rufescens* (red abalone) shell and concentrates on the following:

- The control of the formation of a specific structure that appears during the growth of nacre, which is called mesolayer. This is believed to act as an "interruption" of the self-assembly nacre growth process.
- The mechanical properties of the nacre and mesolayer, which are tested using nanoindentation.

In this section, crucial concepts of this research will be introduced, such as *Haliotis Rufescens* nacre, experimental method, and the research motivation.

Live abalone and nacre samples involved in this research are obtained from California red abalone. These are chosen due to their accessibility and large size, which allows for easy experimentation.

1.1. Self-assembly and Biomineralization

Two types of self-assembly process are defined and widely discussed: the dynamic self-assembly and the statics self-assembly [1]. In this dissertation, only the statics self-assembly process will be discussed.

As a typical bottom-up process, the self-assembly mechanism is an attractive technique due to the autonomous formation of highly-ordered and well-controlled structures at the nanoscale. The highly-ordered structure attracts researchers' attention due to the possibility of the unique and outstanding properties of the materials being strengthened by this structure in specific orientations [1-4]. Crucial factors for self-assembly are: an environment that enables components to move freely and a "template" [1,4]. There are various types of "templates". For example, the attraction between chemical bonds [5] and kinetics control in the colloidal environment [6] are all thought determine the complex and highly ordered nanoscale structures. To approach a self-assembly, templates need to be introduced appropriately [7-10].

Self-assembly makes a great contribution in building the nanoscale structure details for devices and structures in the industry by controlling the mechanism of this process. The precision of self-assembly structures is greater than the conventional mechanical technique. This process should be controlled as much as possible and should produce the exact structure needed to meet requirements. Thus, applications of this technique are expected in comprehensive technology fields [11-14]. So, learning the mechanisms of this process is important.

In fact, self-assembly is a common process in the biological world. After millions of years of evolution, many creatures use a self-assembly process called biomineralization, which is a crucial part of their survival in the natural environment. This fascinating mechanism generates complex

structures in many organisms, and, so far, some products of the biomineralization process still cannot be accomplished by artificial work. Besides producing extremely fine structures with favorable mechanical properties, biomineralization also provides the self-assembly process with a biological non-toxic environment. A popular and important example is the abalone nacre growth in the colloidal organic liquid it produces by itself. This liquid is believed to include liquid crystal and has quite a complicated composition [15].

A considerable amount of research has been done regarding calcium carbonate ($CaCO_3$). This compound has been thoroughly studied by various researchers not only due to its comprehensive application in the industry, but also because it is an extremely crucial product of the biomineralization process. Numerous crystalline formation experiments methods have been done for $CaCO_3$ formation using chemical techniques. These experiments and the mechanisms were closely reviewed, concluded and then developed by Dr. Cölfen in his work [16].

However, the biomineralization for producing the $CaCO_3$ is much more complicated than the chemical synthesis process. All the conditions are deliberately arranged in chemical synthesis experiments, yet a lot of factors are unknown and uncontrollable by people in the biomineralization process. It is hard to obtain the *in-situ* observation of the physiological activities responding to the outside environment change. The complex biological system brings forth a lot of challenges to the biomineralization investigation based on live creatures.

1.2. *Haliotis Rufescens* (Red Abalone) Nacre

As mentioned above, *Haliotis Rufescens* nacre, which is also called “mother of pearl” is a product of biomineralization. In macro-scale, the *Haliotis Rufescens* shell could be divided into two parts: the outside portion facing the seawater environment with a rough surface and the inside portion

facing the abalone's soft body with an iridescent surface, which is much smoother than the outside shell (**Figure 1**). This inside section is the leading factor of the research – the nacre.

When the shell is cut into pieces, the cross-section shows the boundary of the two parts (**Figure 2**). This boundary is very clear due to the different colors and fracture traces of the two parts. Thus, these two parts could be easily distinguished without using any microscopy through the cross-section of a cleaved shell piece. In *Haliotis Rufescens nacre,* the outside calcite part has a red color, while the nacre is white. The boundary between the two is distinguishable from the cleaved cross-section side.

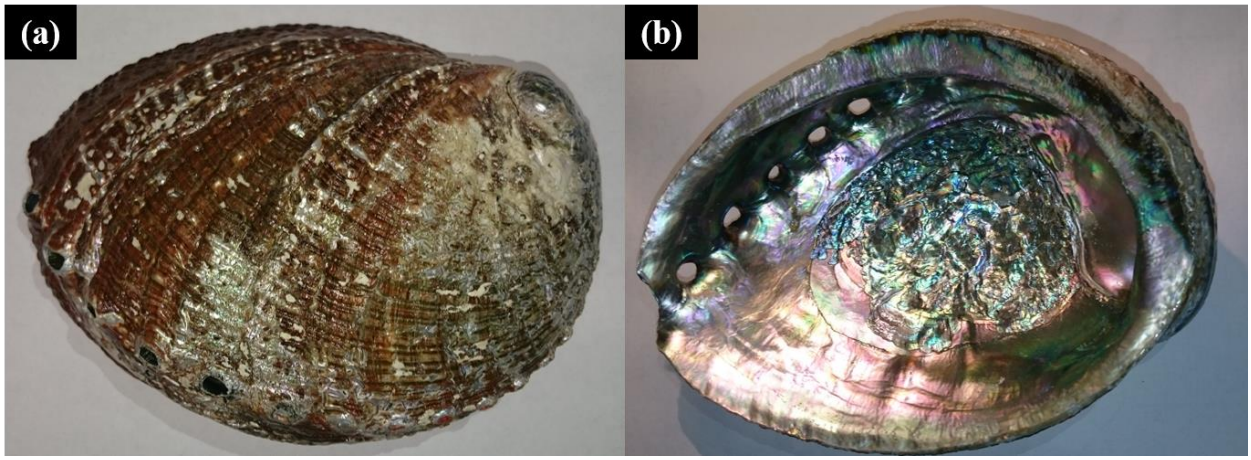

Figure 1*. Camera photos of California red abalone shell. (a) Outside part of abalone shell which is facing to seawater environment and showing rough surface. (b) Inside part of abalone shell which is facing to the soft body of abalone and showing the iridescent and smooth surface.*

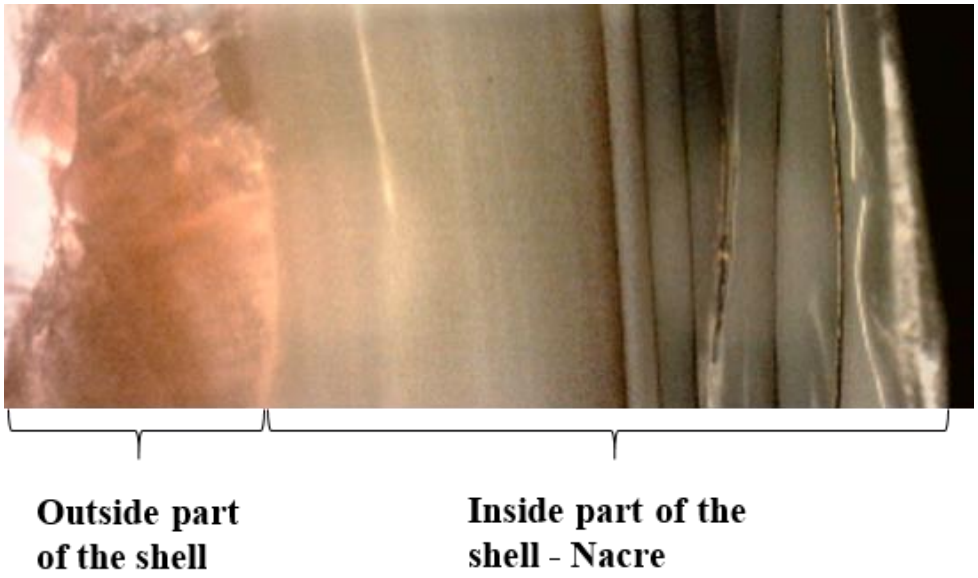

Figure 2. *The optical microscope image of the cross-section of a cleaved Haliotis Rufescens shell. The two parts of the shell could be easily distinguished as the boundary is clear.*

To avoid being confusion and misunderstanding, the view shown by **Figure 1 (b)** is defined as the "top-side", "top-side view", and "top-side sample". The view shown by **Figure 2** is defined as the "cross-section-side", "cross-section-side view", and "cross-section-side sample". More details concerning the "top-side sample" and "cross-section-side sample" will be provided and explained in the Experiment section.

1.2.1 Nacre Composition

The *Haliotis Rufescent* shell is mainly made of calcium carbonate. The outside is calcite and the inside nacre portion is aragonite. Calcite and aragonite are different types of calcium carbonate with a slight difference in crystalline structure. The calcite and aragonite belong to the trigonal and orthorhombic crystal structures, respectively. In fact, both calcite and aragonite are common mineral compositions in organisms [17]. For the *Haliotis Rufescent* nacre, more than 95wt% of it is aragonite and less than 5wt% of it is organic composition [18].

The composition of the mineral portion of nacre is relatively simple and pure, while the composition of the organic portion in nacre is quite complicated. The β-chitin, silk fibroin-like proteins, and acidic macromolecules have long been speculated to be the organic composition in nacre [19]. Many detailed types of the organic components isolated from the nacre have been concluded [18]. Among those organic components, the β-chitin is the most confirmed one. It consists of 2-acetamido-2-deoxy-β-D-glucose through a β (1 4) linkage and known as a natural and common structural polysaccharide and heteropolymer material with very low solubility in either water or most other types of the organic solution [20]. Chitin is a common organic composition which acts as the structural material in marine organisms.

1.2.2 Nacre Structure and Growth

The structure that shows diverse features along a different length scale is defined as the hierarchical structure. Engineers believe this structure to be the structure resulting in the outstanding and unique mechanical behavior such as the negative Poisson's ratio [21]. A classic example of a hierarchical structure is the famous Eiffel Tower.

This structure is not only important to the civil engineers but also popular in the materials science and engineering area. Polymer, crystal, and composite materials all show the hierarchical structure. It is a very important structure in the world of biology. The bone, tendon, and bamboo all show the hierarchical structure. The importance of the structure's ability to enhance the toughness and strength of the hierarchical structure has already been discussed in detail [22-24].

The leading factor of this research, the Haliotis Rufescens nacre, is one of the typical examples of the biological material with hierarchical structure. Based on the advantages brought by the

hierarchical structure, it is no wonder that the Haliotis Rufescent nacre has excellent mechanical properties.

There are two types of nacre: columnar and sheet [25]. Although both show the laminated structure, which is built by countless nano-scale aragonite tablets (300nm-500nm thickness, 5μm-10μm diameter), the alignment of these tablets is different in the two types of nacre. The center of the tablets in each layer almost aligns in rows in the columnar nacre while they are randomly distributed in the sheet nacre. This alignment difference was shown by the SEM images taken of the deformation caused by tensile testing each of these two types of nacre [25]. The abalone nacre belongs to the columnar nacre.

SEM measures the thickness of the tablets of the nacre sample included in this research. And, based on hundreds of countless measurements of various samples, the thickness is always shown in the range between 300nm-400nm (**Figure 3**). These aragonite tablets are jointed with each other in both vertical and horizontal directions by an organic thin film. The surface of these tablets is not as smooth as the faces of the mineral single crystal of aragonite. Instead, countless nano-asperities could be observed on the tablets surface, which is believed to be in relation with the excellent mechanical properties of nacre [26-27]. If the nacre is demineralized, the organic thin film connecting the tablets could be observed left as a frame (**Figure 4**) [28]. And, those left organic frames are the insoluble organic composition. The EDTA is usually used for demineralizing the calcium carbonate portion [29-30]. Some studies indicate that this organic matrix plays a crucial role in the development of the excellent mechanical behavior of the nacre [26,31,32].

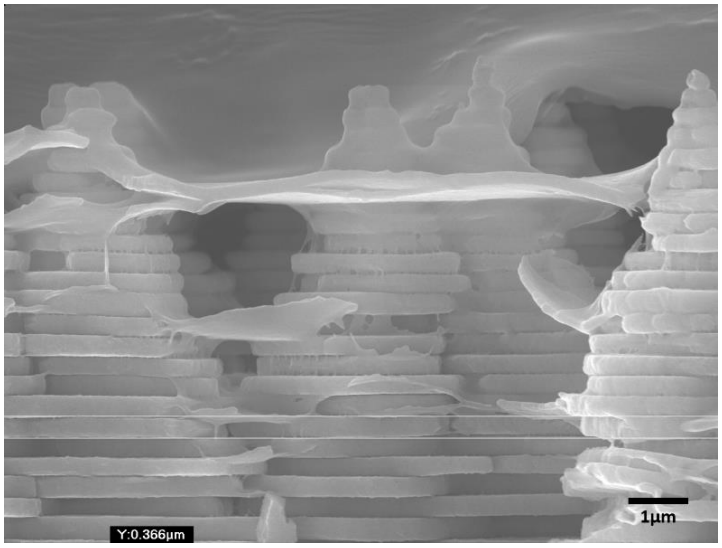

Figure 3*. The measurement of the Haliotis Rufescens nacre tablets thickness by using SEM. The nacre samples included in this research have the tablet thickness varies between 300nm-500nm. The one shown in this SEM image is 366nm.*

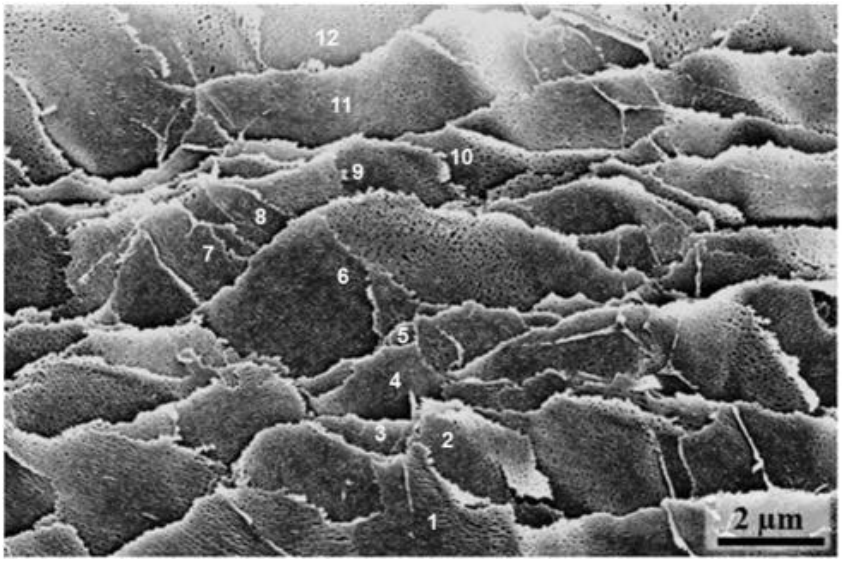

Figure 4. *The organic frame left after applying demineralization on Haliotis Rufescent nacre. There are 12 organic layers are numbered. Reprinted from Materials Science and Engineering: C, Vol 58, López, M. I., & Meyers, M. A., The organic interlamellar layer in abalone nacre: formation and mechanical response, 7-13, Copyright (2016), with permission from Elsevier. [28]*

The microstructure of nacre could be well characterized by SEM. **Figure 5(a)** is a top-side view SEM image of the nacre which is continuously taken along the direction from nascent nacre to the mature nacre (from the left area to the right area in the image). The **Figure 5(b)** is the cross-section-side view of the nascent nacre, while **Figure 5(c)** is the cross-section-side view of the mature nacre (the tablets align in column morphology). The nascent nacre shows the "Christmas tree" morphology and the mature nacre shows the morphology of the aligned tablets in column pattern. With the SEM images taken at the nacre growth front area, i.e. the area of the nascent nacre, as evidence, nacre tablet is believed to initially grows along the c-axis. When a height of 300nm-500nm is approached, it will extend along the a,b-axis until it reaches the adjacent ones.

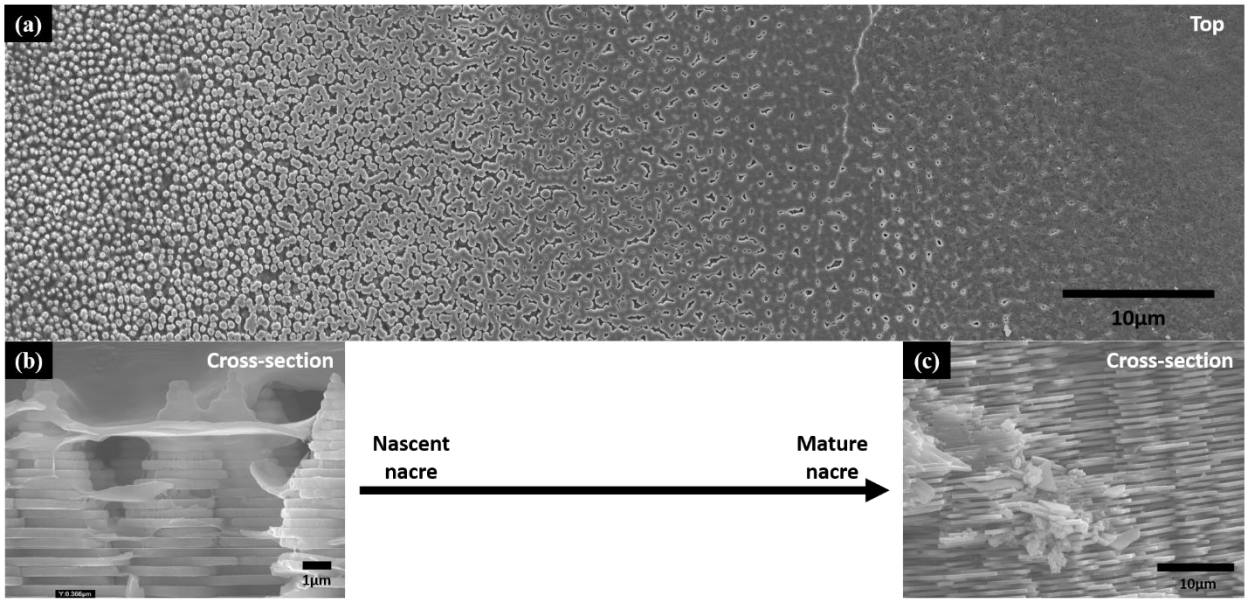

Figure 5*. The nacre structure of different growth phase. (a) The top-side view of the transition from nascent phase (left area) to the mature phase (right area); (b) the cross-section view of the nascent nacre (the "Christmas tree" morphology); (c) the cross-section view of the mature nacre (the column tablets morphology).*

In fact, the nacre growth is a process staying far away from the thermodynamic equilibrium balance which could be described by the Ostwald step rule (**Figure 6** [33]). Based on this rule, the crystallization process starts from forming the thermodynamically most unstable phase and finally ends at the most stable phase step by step. What should be noticed here is that, during the whole crystallization process, not all the intermediate crystals will appear [16]. The crystallization process of calcium carbonate is the specific one that will be discussed here. There are three types of calcium carbonate: the calcite (the most stable), aragonite (metastable), and vaterite (the most unstable). Among those three, the aragonite is the intermediate phase which is not preferred in the crystallization process. It could nucleate in the special medium. For the nacre, the main mineral composition is aragonite. The mucus environment which the nacre grows in is the key point for this biomineralization process. The supersaturation and the nucleation active free energy of the aragonite transforming from amorphous solid working together to determine the existence of it [16].

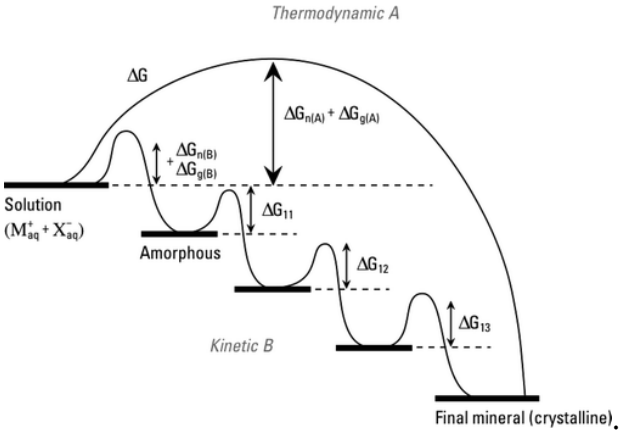

Figure 6. *The comparison between the thermodynamic control and kinetic control pathway. Reprinted from Angewandte Chemie International Edition: Volume 42, Issue 21, Helmut Cölfen, Stephen Mann, Higher-Order Organization by Mesoscale Self-Assembly and Transformation of Hybrid Nanostructures, 2350–2365, Copyright (2003), with permission from Wiley- VCH.[33]*

As such a highly-ordered and fine structure is produced by a completely natural process, the investigation of the growth mechanism of this structure could contribute to developing the technique of producing composite materials. Details of this biomineralization process are studied and demonstrated by various studies to assist with the synthesis of materials with complex structures. For the nacre growth, the organic composition such as the proteins has long been believed to play a key role. Also, the relation between the organic composition and nacre growth has been investigated on numerous occasions [34-37].

Besides the organic molecule, the amorphous calcium carbonate (ACC) is another crucial component during the nacre growth. Although nacre is made of aragonite and all the aragonite tablets are in the same orientation, its appearance has no similarities to the needle-like mineral single crystal aragonite. In the nacre, the ACC gradually accumulated together and transferred to the aragonite crystal structure with the precipitation of organic molecules. Finally, the aragonite tablets form, and is defined as belonging to the mesocrystal [38-39].

Abalones have the nacre growing in a confined space formed by its shell and a tissue of its body called the mantle. The mantle attaches on the shell closely, thus the space between the two is isolated from the outside environment. The mucus secreted by the abalone fills up this space and the nacre grows in this isolated environment.

1.2.3 Mechanical Property

Although the abalone has a soft and vulnerable body, it has survived on earth for millions of years due to being protected in the shell.

The mechanical properties of nacre have been extensively investigated since the outstanding toughness was first observed [40]. Many different mechanical tests were applied on nacre to study

its mechanical properties, such as the tensile test [41-42], 3-points bending [42], 4-points bending [43], nanoindentation test [44-45], and compression test [46]. The nacre is now commonly known for behaving with 1000 times higher toughness than the mineral aragonite single crystal [47]. Amazingly, the nacre shows a high toughness despite the composition comprising largely of brittle material. Different test methods could produce difference values even for the same property. For example, within the same research group, the elastic modulus tested by tensile test (~8GPa) is much lower than the value tested through 3-point bending (Face-on elastic modulus 69 ± 7 GPa, Edge-on elastic modulus 66 ± 2 GPa) [42]. In the same literature, the failure strain tested through tensile test is also different from what was obtained from the bending test. As the research stated in this dissertation is mainly based on the nanoindentation test, only the elastic modulus tested through the same or similar test method will be used as reference and discussed. Some of the nanoindentation tested elastic modulus of the red abalone nacre were collected and listed in **Table 1.**

Sample Type	**Elastic Modulus Tested by Nanoindentation Test**
Face-on [42]	69 ± 7 GPa
Edge-on [42]	66 ± 2 GPa
Freshly Cleaved Nacre (Single Tablet) [44]	114 GPa - 143 GPa
Artificial Seawater-soaked Nacre (Single Tablet) [44]	101 GPa - 126 GPa
Red Abalone Sample Single Tablet [48]	79 ± 15 GPa
Red Abalone Sample [49]	55 – 75 GPa
Polished Red Abalone Sample [52]	60 – 80 GPa

Table 1. *The collected elastic modulus of the red abalone nacre tested by nanoindentation test.*

As the facts mentioned above, the fine and unique nanostructure of the abalone nacre is the key to explaining the fascinating mechanical behavior. The SEM images of the nacre sample tested by tensile test supports the idea that the tablets sliding is the important mechanism strengthening the toughness (**Figure 7**) [50]. The fracture always appears at the connection between two adjacent tablets. The similar phenomenon was also reported in other tensile tests applied on red abalone nacre sample [42].

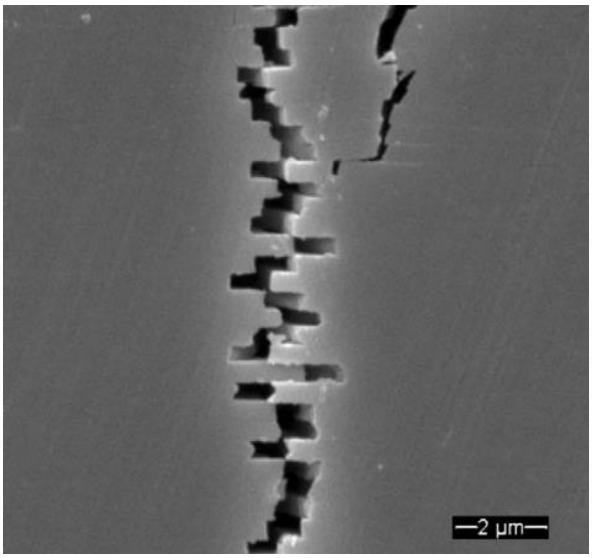

Figure 7. *The red abalone nacre tablets sliding (separation) after the tensile testing. Reprinted from Materials Science and Engineering C, Volume 26, Issue 8, Yu, Albert, Lin, Min, Andre, Marc, Vecchio, Kenneth S, Mechanical properties and structure of Strombus gigas , Tridacna gigas , and Haliotis rufescens sea shells : A comparative study, Pages No.1380-1389, Copyright (2006), with permission from Elsevier.[50]*

Some data from the mineral single crystal aragonite could be used to compare with the nacre to show the differences brought by the structure. The modulus of different crystal planes of a single crystal aragonite was collected from the nanoindentation test with a Berkovich tip as listed in **Table 2** [51]:

Crystal Plane	Modulus (GPa)
(0 0 1)	102.8 ± 2.4
($\bar{1}$ 1 0)	100.1 ± 3.4
($\bar{1}$ $\bar{3}$ 0)	108.1 ± 2.3

Table 2. *The nanoindentation tested modulus of different crystal planes of a single crystal aragonite.*

The modulus values of the two planes which are perpendicular to each other, such as the (0 0 1) and ($\bar{1}$ 1 0), are close to each other in the single crystal aragonite while there is an almost 20 GPa difference in the abalone nacre. The modulus of the plane (0 0 1) in the nacre is around 50 GPa, which is much lower than that of the single crystal. To confirm this using our instruments and samples, in this research, a purchased aragonite single crystal sample is characterized for comparing with a nacre sample. XRD is applied on the planes in both samples (single crystal aragonite and red abalone nacre) and are expected to have the same crystal plane. The spectrums are then plotted together (**Figure 8**). In observation, it was found that the main peaks in these two spectrums overlap. Some extra peaks appear in the spectrum of the abalone nacre sample, which might be caused by the tablets orientation shifting. The nanoindentation test results of the single crystal aragonite are 99.37 ± 2.1534 GPa and it is 45.83 ± 1.5867 GPa for the red abalone nacre. The difference is so distinctive that the architecture of the nacre should be expected to play an important role in influencing its mechanical property.

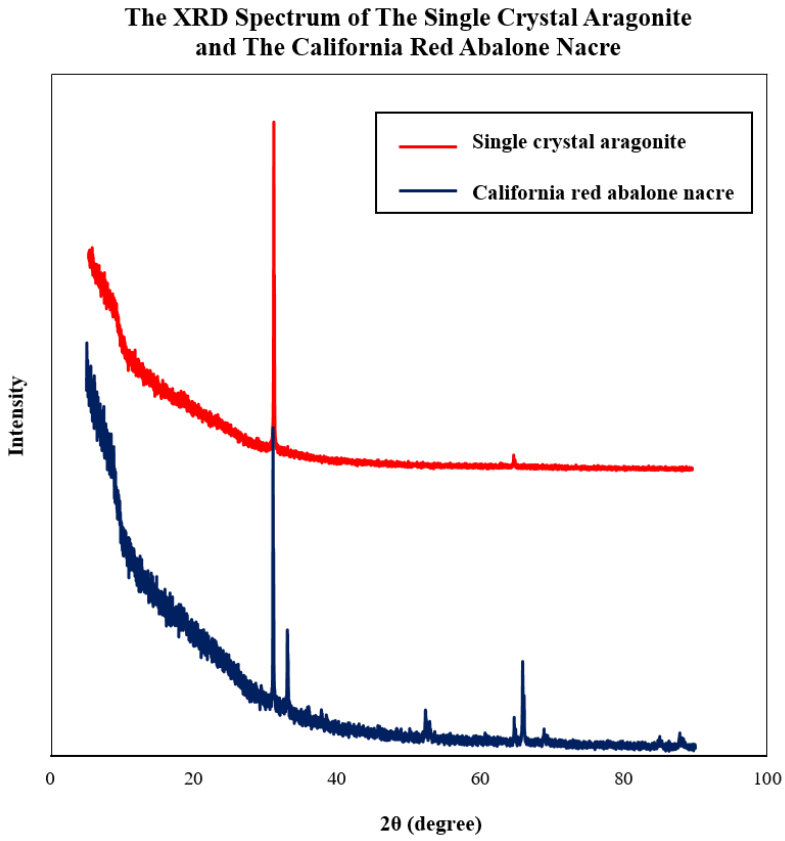

Figure 8*. The spectrum of the XRD applied on the plane of single crystal aragonite and nacre. The plane that is applied the XRD in the two samples are expected to be the plane.*

Besides the single crystal aragonite, the elastic modulus of the individual aragonite tablets of red abalone nacre was also reported [52]. The elastic modulus tested through the nanoindentation test is various between 60 GPa and 80 GPa. This value is lower than the mineral single crystal aragonite. The organic composition involved in each single tablet is the possible reason for explaining this. In fact, this is the elastic modulus range when the nanoindentation test is applied on the surface of nacre sample which is perpendicular to the tablets front surface. At the meantime, when the test is applied on the sample surface which is supposed to have the tablets front surface being exposed on the top, the elastic modulus is much lower than 60-80 GPa. Thus, the hierarchy structure of nacre is crucial in causing the anisotropic elastic modulus of nacre.

When force is applied to the nacre, a common occurrence in the deformation mechanism is tablet sliding. There are many factors, such as nano-asperities on tablets surface, tablets waviness, mineral bridges between the vertically adjunct tablets [53] that can contribute to the interference of the sliding and the fascinating mechanical properties. However, as it is hard to observe the deformation process immediately, the influence brought by these factors are kept under argument. For example, as the nano-asperities were thought to influence the mechanical properties [27], it was disproven by detailed calculation and FEM model analysis [48]. Thus, more investigation about nacre mechanical properties is necessary. With clear knowledge about the mechanism of how the nacre behaves, the production and improvement of the current complex artificial materials with great mechanical properties could then be approached.

The mechanical property test is a crucial part in the research stated in this dissertation. The method used here is nanoindentation test. This test method was selected to investigate the elastic modulus of nacre because the test scale matches the nacre tablets and mesolayer size. It could also help to reveal the deformation behavior of the nacre tablets and mesolayer when tests are applied to them. The nanoindentation test mainly shows the Elastic modulus (E) and Hardness (H) of the sample. Thus, the mechanical property focused on in this proposal is the elastic modulus of nacre and mesolayer.

By combining the structure and mechanical property, abalone nacre could inspire new ideas of producing new types of composite materials.

1.3. Mesolayer

The countless aragonite tablets built structure is not the only structure observed in the nacre. Another structure named the ‘mesolayer’ has been observed. Even raw eyes could determine the

existence of the mesolayer. In a camera photo of the cross-section of a cleaved nacre sample, as shown in **Figure 2**, some distinct black lines are visible in the nacre. These black lines are the mesolayer. And, if camera photos are taken over the surface for the top-side samples, the nacre with and without mesolayer could be easily distinguished (**Figure 9**). In **Figure 9**, the bottom left sample is the one that has the mesolayer while the right one has no mesolayer. In the left sample, the yellow curves represent the edge of the mesolayer, which indicates the underneath mesolayer.

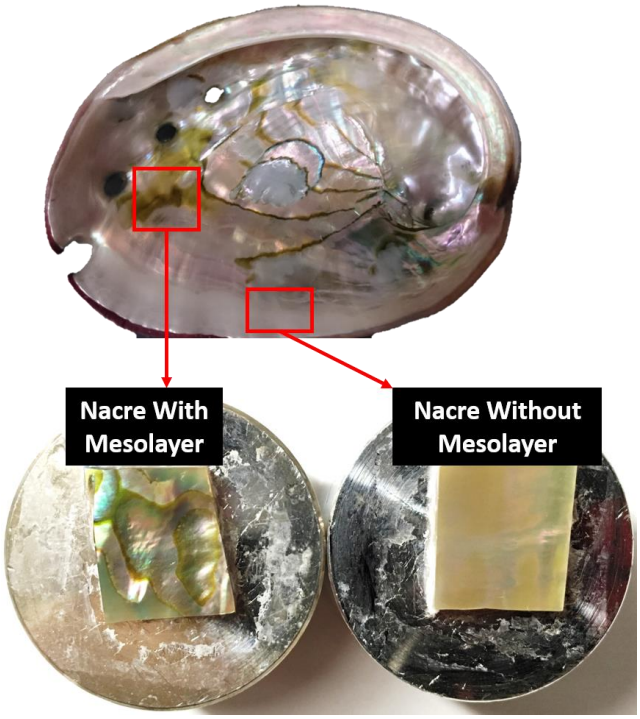

Figure 9*. The camera photo of the nacre samples (a) with mesolayer and (b) without mesolayer.*

The SEM images of the distribution of the mesolayer are shown below (**Figure 10**). From the micro-scale, the mesolayer could be divided into three separate sublayers: the prismatic layer, the organic layer, and the columnar-like layer (**Figure 11**). The structure of mesolayer is significantly different from the tablet built structure. The three sublayers all have their own individual and unique structure morphology, which was easily distinguishable. The SE image and BSE image of

the same area of the mesolayer could be used to compare with each other to learn more details about the morphology and composition contrast of the mesolayer (**Figure 12**). In the BSE image (**Figure 12(b)**), there is no contrast amongst the prismatic layer, columnar-like layer, and the tablets area, which represents the identical composition. However, the organic layer is much darker than all the other parts due to the light elements included in the organic composition. By using the growth direction of the tablet structure as a reference, the growth direction of the mesolayer could be determined as starting from the columnar-like layer and ending at the prismatic layer (**Figure 11**).

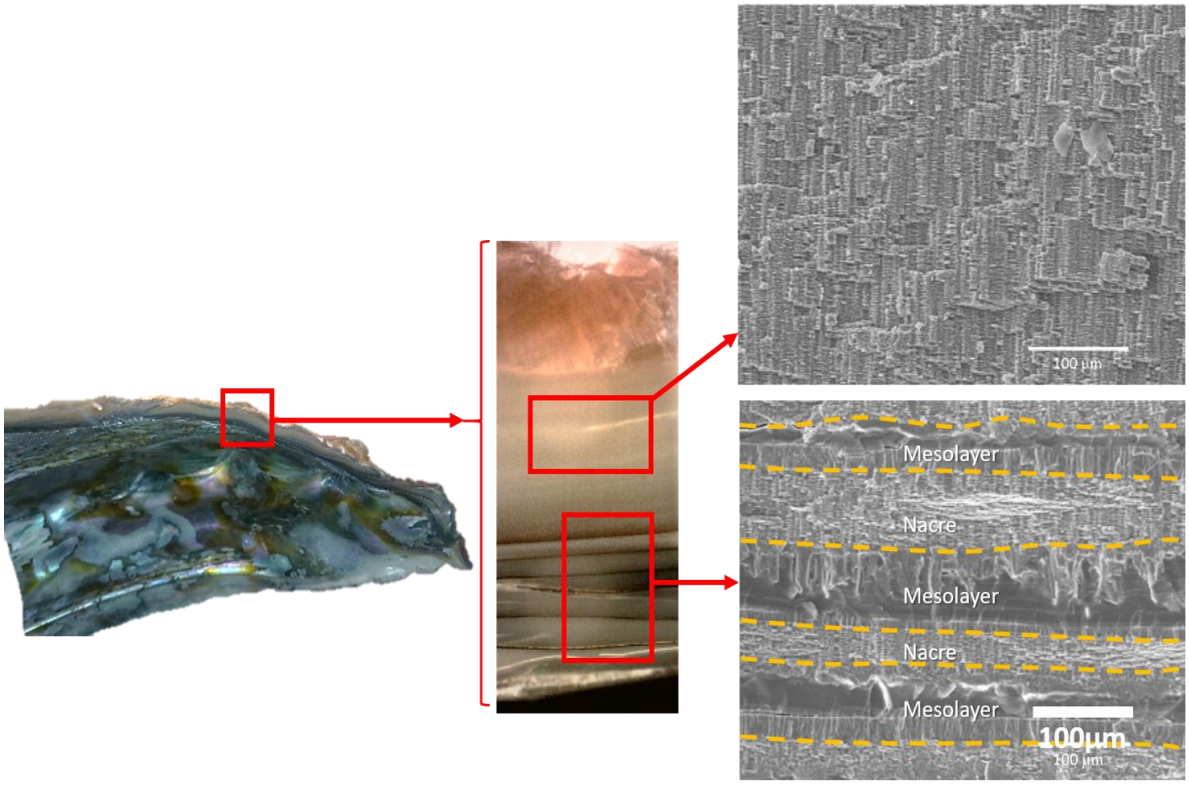

Figure 10. *The black lines observed in the nacre from the cross-section side of the wild abalone nacre has the different structure compared with the tablets architecture.Those are defined as the mesolayer.*

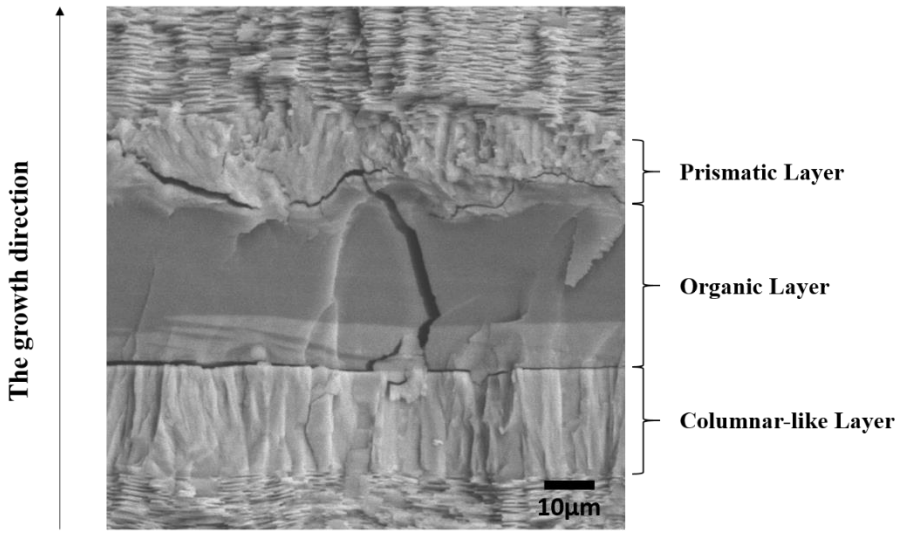

Figure 11*. The mesolayer could be divided into three sublayers: the prismatic layer, the organic layer, and the columnar-like layer. The mesolayer growth starts from the columnar-like layer.*

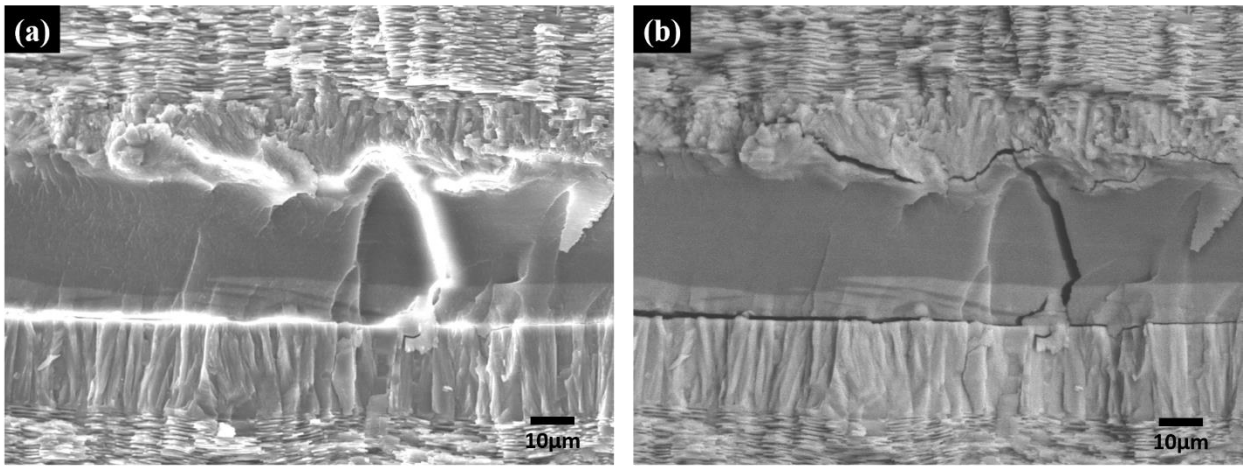

Figure 12. *SEM images of the mesolayer from cross-section side. (a) SE image; (b) BSE image. The morphology and composition difference among the sublayers could be easily distinguished by the SEM images*.

The mesolayer is observed to exist in nacre layer by layer, suggesting a periodically repeated growth. Furthermore, based on the observation of various samples, all the “black lines”, i.e. the

mesolayer, show the same three sublayer structure. Thus, this columnar-like layer – organic layer – prismatic layer structure is treated as a typical structure of the mesolayer.

Although it is a quite unique structure which is different from other parts of nacre, only very limited researches have focused on it. The growth process of the prismatic layer of the mesolayer was characterized week by week [54] but the whole growth process and the start of the growth of mesolayer is still waiting to be revealed. In those literatures describing the mesolayer, different factors were studied to investigate their influence on the formation of the mesolayer. Almost all those researches are based on the observation in the Flat Pearl Method which is helpful for this and will be introduced in section "**1.5 The Flat Pearl Method**". The special water-soluble biopolymer is believed to be one reason for causing the formation of the mesolayer which includes a transition from the aragonite formation to calcite formation [55]. Besides, the different water temperature and feeding supply were also tried to see their effects on nacre growth and the calcite-aragonite transition [77]. So far, there is still no final conclusion of the reason of the mesolayer formation. And, the mechanical property investigation of the mesolayer and its effects on the whole nacre structure is still unknown.

1.4. Seawater Environment and Calcium Carbonate Formation

In the natural environment, abalone lives in the sea. This is quite a complicated system with a strong self-adjust ability. For the creatures, it is normal that their living environment influences the physiological activities. Thus, it is important to learn about the sea environment while investigating the nacre growth.

In our lab, sea salt, sea sand, and some seaweed are used to mimic the sea environment. In the mimicked small sea system, the environment shows the strong self-adjust ability. When some

extraneous, accidental interruption factors were induced into this small system, parameters show the trend to be back to the original level. For example, based on the observation in our lab, when the pH value of the mimicked seawater environment decreased due to new dried sea plant addition (for feeding abalone), it will increase back to the original level in several days. On the other hand, parameters of the seawater always influence each other. In that small mimicked seawater system, the pH value decreases as the temperature increases. In fact, the alga, bacteria, and some chemical reactions all have the possibility to influence the seawater parameters. In the natural sea environment, the relations among parameters are affected by more factors and are more complicated.

In fact, these relations among the parameters of natural seawater have been investigated a lot. In the natural sea environment, seasonal changes, atmospheric pCO_2, the sea floor spreading rate, etc., could possibly change the temperature, pH, Mg^{2+} and Ca^{2+} concentration [56]. Among these parameters, the temperature influences the pH, Mg^{2+} and Ca^{2+} concentration [19][57]. Based on the literature, the Mg^{2+}/Ca^{2+} concentration ratio influences the phase of calcium carbonate formation in seawater directly, such as in reef-building. For the biomineralization process occurring in sea creatures' bodies, which is an environment isolated from the sea, such as the red abalone included in this research, the ion concentration ratio could influence the biomineralization indirectly through affecting physiology process of creatures [58-60]. Thus, the temperature change is expected to influence the calcium carbonate in sea creatures [61]. More importantly, according to these literatures, high temperatures assist in calcite formation and low temperatures assist with aragonite formation. During experiments, many parameters of the seawater are found affecting the physiology process of abalone. For example, according to the observation in our lab, when the temperature increased to a too high level (around 20ºC), the abalone reduced the consumption of

food. And if the temperature is kept at that high level for too long (2-3 weeks), some abalones might even die. The fluctuation of pH between 7 and 8 at low temperature (around 12-14 ºC) does not influence the abalone in an observable way. The artificially decreased pH at high temperature causes abalone death within several days.

1.5. Flat Pearl Method

Since it was first developed, the Flat Pearl Method has been a quite common method used in many different types of research involving abalone nacre growth [48, 54, 62]. In this method, some substrates are fixed by super glue in the confined space built by the inner side of abalone shell and part of its mantle tissue (**Figure 13**). After several weeks, these substrates are taken out. The nacre grown in these weeks could then be observed without slaying the abalone. And, the live abalones could participate in more experiments.

Figure 13*. Pieces of micro cover glass slides were implanted in abalone as substrates based on conventional Flat Pearl Method.*

In this research, ϕ12mm circle VWR micro cover glass and calcite slides (prepared with the outside calcite part of abalone shell) were used as substrates. These substrates were fixed on the inner side of abalone shell (the side facing abalone's body) with super glue. Within several days, the mantle covered and enveloped the substrates in the confined space between the shell and

mantle. After several weeks, these substrates were taken out from abalone. By taking Scanning Electron Microscopy (SEM) images, the structure formed during these weeks could be analyzed.

The Flat Pearl Method is an appropriate way to investigate the nacre growth. Fresh samples, especially for these nascent nacre samples, could be collected from this method and characterized, along with the nacre growth within a specific period

1.6. Nanoindentation Test

Nanoindentation testing has been considerably developed in the past 50 years and is mainly used to investigate the modulus and hardness of the material. This method is great for testing the materials with random shapes, micro- or nano-scale, and detailed microstructures. Even a quite small piece of a sample could be used for the nanoindentation test through appropriate mounting, grinding, and polishing. Based on these advantages, the nanoindentation test has become a popular and more practical test method used today. It plays an important role in many areas, such as the investigation of the mechanical behavior of irradiated materials and components in the electronic chip.

The instrument system is well described with a schematic draft in early literature (**Figure 14** [63]). One nanoindentation test finishes a cycle of loading and unloading (**Figure 15**). For the Nanoindenter in our lab, due to the viscoelasticity of the sample, a segment of tip holding is there after arriving at the peak load and before starting to unload. And, instead of unloading to zero, the unloading process will start a thermal drifting hold test before that. The nanoindenter involved in this research uses Continuous Stiffness Measurement (CSM) to determine the mechanical properties of samples. In this CSM method, load oscillates during the loading process and the oscillation resolution is 2nm. This oscillation could be shown by the amplified loading curve in

Figure 15. Also, data is collected from the unloading steps in the oscillation. The current going through the coil controls the load applied on the sample, and a specific capacitive sensor records the indentation depth. The stiffness could be recorded dynamically through the oscillation during the loading process shown by the loading curve or be determined through the initial part of the unloading process shown by the unloading curve.

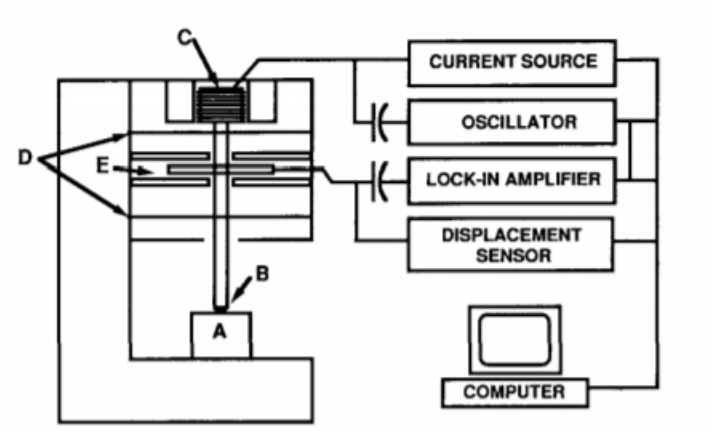

Figure 14. *A schematic draft describes the instrument system. In this draft, A and B represent the sample and nanoindenter tip respectively. C is the coil controlling the load. D is the guide springs, and E represents the indentation depth sensor. Oliver, Warren Carl and George Mathews Pharr, an improved technique for determining hardness and elastic modulus using load and displacement sensing indentation experiments, Journal of materials research, Volume 7, Issue 6, 1564-1583, reproduced with permission [63].*

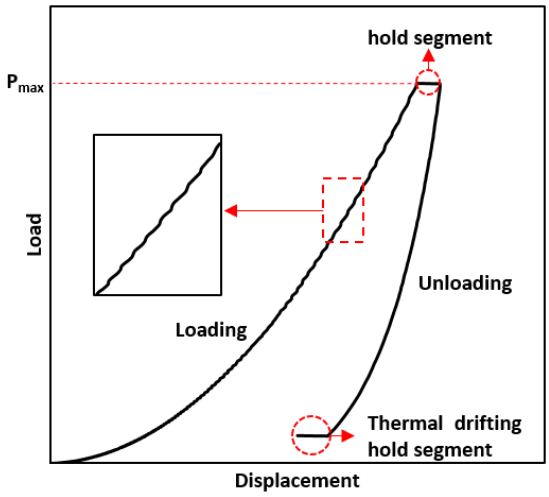

Figure 15*. A practical test diagram of the loading-unloading curve recorded by MTS Nano Indenter (CSM/LFM Control Unit) with Berkovich tip. In this diagram, Pmax represents the peak load.*

The nanoindenter tip used in our lab is a Berkovich tip (diamond), which shows a triangular pyramid geometry (**Figure 16**). Based on the experimental evidence, the contact between the Berkovich tip and the sample surface could be described by the Sneddon contact (**Equation 1**) as an extended solution [64]:

$$s = \frac{dP}{dh} = \frac{2}{\sqrt{\pi}} * E_r * \sqrt{A}$$

Equation 1. *s = The stiffness, P = The load, h = The displacement, E_r = The tested reduced modulus, A = The area function of the nanoindenter tip.*

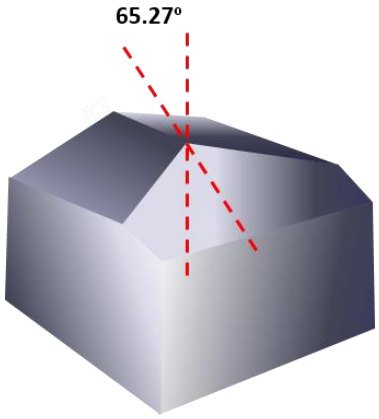

Figure 16*. The schematic draft of the Berkovich tip used in this research. The tip is made of diamond.*

And, the area function of the Berkovich tip is (**Equation 2**) [64]:

$$A = 24.5 * d^2$$

Equation 2*. A = The area function of the nanoindenter tip, d = nanoindentation depth.*

The relationship between the tested reduced modulus and the modulus of the sample could be expressed by **Equation 3** when it comes to a uniform material [64]:

$$\frac{1}{E_r} = \frac{1 - v_i^2}{E_i} + \frac{1 - v^2}{E}$$

Equation 3*. E_r = The reduced modulus, v_i = The Poisson's ratio of the nanoindenter tip, E_i = The elastic modulus of the nanoindenter tip, v = The Poisson's ratio of the sample, E = The elastic modulus of the sample. As the nanoindenter tip included in this research is diamond, the value for E_i and v_i are 1.141GPa and 0.07[65-66].*

When it comes to a sample with a thin film on the top, this relationship is expressed by the more complicated equation [67], which was developed from the empirical relation obtained by Doerner and Nix [68].

As what is mentioned above, the dynamic stiffness is calculated from the loading oscillation (**Equation 4**) [63]:

$$\left|\frac{P_{os}}{h(\omega)}\right| = \sqrt{\left\{\left(s^{-1} + C_f\right)^{-1} + K_s - m * \omega^2\right\}^2 + \omega^2 * D^2}$$

Equation 4*. C_f = The compliance of the load frame (~1.13m/MN), K_s = The stiffness of the column support springs (~60N/m), D = The damping coefficient (~54Ns/m), P_{os} = The magnitude of the force oscillation, $h(\omega)$ = The magnitude of the resulting displacement oscillation, ω = Frequency of the oscillation (69.3Hz), m = mass (~4.7gms).*

In nano-scale, *Haliotis Rufescens* nacre is built by countless aragonite tablets with uniform orientation. In macro-scale, *Haliotis Rufescens* nacre shows a dome shape with random surface waviness. With the advantages of testing mechanical behavior in the nano-scale and preparing the sample with a random shape easily, the nanoindentation test became the first choice for testing.

In this research, depending on the test depth, only 1 to 5 tablet layers were tested. Although the whole nacre structure shows that high toughness, its main composition is calcium carbonate and still could be treated as a ceramic material. Thus, cracks in one or two tablet layers may occur and influence the test results (the cracks are confirmed by applying the FIB on the nanoindentation and the SEM images will be shown in the Experiment section). Thus, the chromium film, which is a rather ductile material, was sputtered on both top and cross-section side of nacre surface at room temperature. The nanoindentation tests were then applied on the chromium film. Using SEM images and the developed thin film model for nanoindentation tests [69-70], more accurate results were obtained without the influence brought by nacre cracking.

1.7. Research Motivation

Due to the outstanding properties brought by the unique structure, the nacre inspires so many innovative researches [71-75]. For the nacre itself, in fact, so many truths are waiting to be revealed. Both the nacre growth and its mechanical behavior are complicated problems and arguments never stopped. For example, for the nacre growth, although the development of the systematic theories is progressing, some other researchers are questioning them with new discoveries. The always believed epitaxial growth mechanism is challenged by the ACC found on the surface of the aragonite tablets, and, this research addressed the importance of the physicochemical effects [76].

The research work stated in this dissertation is intended to move one step forward in the investigation of the structure and elastic property of *Haliotis Rufescent* nacre and the mesolayer.

Abundant research is focused on the synthesis of the nacre-like structure based on different materials to obtain unique and outstanding properties. Study of the natural biomineralization

process occurring inside the abalone could inspire new ways of nacre-like structure synthesis. It is mentioned above that studies rarely concern the mesolayer. However, it should be noticed that studying the mesolayer growth contributes to learning about the relation between the special structure formation and the required conditions, which could reveal more details about the complex biomineralization process and to assist the synthesis of composite materials. Since the mesolayer is a change of structure compared to tablets nacre structure during the outside and inside environmental factors changing, the study of the mesolayer growth process is a way to figure out the roles that these factors are playing in the biomineralization process. The relation among the environment temperature, the food availability, and the nacre growth has been discussed by other researches which are based on the red abalone and many other creatures through the Flat Pearl Method [77-79]. In this research, the relation between the temperature and the mesolayer formation is investigated. Meanwhile, the relation among the temperature, pH, Mg^{2+}/Ca^{2+} concentration of the seawater environment was daily recorded and described.

The mucus in the confined space built by the mantle and shell is the immediate growth environment for the nacre. So far, it is hard to observe the nacre and mesolayer growth process *in-situ*. Thus, the studies related to that mucus might be another possible way to learn more details about this biomineralization process.

For the studies about the mechanical properties of the mesolayer, the work is expected to collect more details about the mechanical behavior of this mesolayer and make a contribution to understanding the role that the mesolayer plays in the whole nacre structure. For the nacre, a lot researches have been focused on its toughness and the ability to resistance the crack growth. In this work, the attentation is paid on another unique property of nacre: the high anisotropic elastic

modulus. It is important to find out how that structure decreases the elastic modulus that much in one direction and less in the perpendicular direction.

The research work included in this dissertation is expected to be one step-forward in understanding this natural composite material and being meaningful in developing, designing, and applying new artificial composite materials based on specific requirements.

2. Experiments Instruments

Only text introduction is included in this section. The images of those instruments are shown in **Appendix I**.

2.1 Optical Microscope (OM)

The Mitutoyo Corporation made optical microscope (Serial No. 300113) is the main one used in the research. It has a digital camera (ZEISS, AxioCam MRc) taking photos. The eyepiece and the camera have the different magnification. Thus, when the software on the computer is used for taking photos, the total magnification set in the software should be determined based on the camera. And, a Nikon SMZ800 optical microscope is also included.

The optical microscope is helpful for taking images of the detail of the structure in macro-scale. Especially, it is a great way to find the position of nanoindentations when they are hard to find by using the SEM.

2.2 Scanning Electron Microscope (SEM)

The SEM used in the research is JEOL JSM 7000F. This field emitting electron microscope is a crucial instrument in this research. With its high resolution, it is mainly used for characterizing the structure of nacre, the nanoindentation applied on the sample, and the dendrites formed in the special environment in this research.

To obtain high resolution SEM image, the conductivity of the sample, the Focus, Working Distance, Electron Alignment, the beam current, and the Probe Current all need to be taken care of. The best working distance for the instrument included in this research is 10mm and the ideal beam current should be around 56μA. When using the tilt function in this instrument, this highest

angle could be done is 40. There are other detectors in the vacuum chamber. Thus, too high tilt angle might cause the crash between the sample holder and the detectors. The IR camera must be open during the tilting and sample holder going up. The voltage used for taking SEM images depends on the property of the sample.

2.3 Energy Dispersive Spectrometry (EDS)

OXFORD Instruments X-Max 20mm^2 detector is used to analyze the composition of samples. The EDS detector is installed in the same vacuum chamber with the SEM. It plays the role for determine the composition of the sample. Although the BS SEM image could show the element difference among different area, the EDS could show the detailed types of element.

2.4 X-Ray Diffraction (XRD)

Bruker D8 Discover X-Ray Diffraction is used to identify the structure of the nacre and the aragonite single crystal in the research.

2.5 Focused Ion Beam (FIB)

The FIB included in this research is the TESCAN LYRA FIB-FESEM in Alabama University at Tuscaloosa. It is used to mill part of the area of nanoindentations on the sample. The sample is tilted to 55º and the ion beam mills the selected part of the material through the stair-step. As the nacre has such detailed nano-scale structure, ion polishing of the milled cross-section is necessary.

By milling part of the material, the behavior of the material under the surface could be characterized by SEM. In this research, this is mean to learn about how the tablets behave underneath after being applied nanoindentation tests.

2.6 Nano-Indenter

MTS Nano Indenter (CSM/LFM Control Unit) with diamond Berkovich tip is used for testing the modulus of materials in the research. The sample used for nanoindentation test must be well polished.

2.7 Sputter

Denton Vacuum, LLC, DISCOVERY 18 Sputter is used in experiments to sputter metal thin film on samples. And the work is done in clean room. The parameters used for sputtering depends on many factors such as the target type, the sample thickness, the power, etc. It is determined by the records of the records of the previous experiments.

2.8 Grinder and Polisher

The Buehler Handimet 2 Roll Grinder is used for grinding and the Leco SS-200 is used for polishing. All the samples used for nanoindentation test need to be well polished. Al-suspension is used for polishing the nacre.

2.9 Haliotis Rufescens (Red Abalone) Lab

Red abalones are purchased from The Abalone Farm at Cayucos in California. They are kept in our lab in the artificial seawater and feed with dehydrated Kelp and many other types of seaweeds.

Instant Ocean Synthetic Sea Salt was used to prepare the artificial seawater. 3-4 California Red Abalones were kept in one 38-gallon tank with the artificial seawater, where the temperature is controlled by AquaEuro USA Max-Chill Titanium Aquarium Chillers (1/13HP). The artificial seawater in the tank is filtered by Penguin BIO-Wheel Power Filters (Model 200) with the Penguin

Rite-Size C Filter Cartridges 24hrs each day. Oxygen is supplied by Eugene Danner Aqua-Supreme Air Pumps (AP-8 Adjustable Air Flow).

Temperature and pH are tested by VWR® pH/Temperature Meter (Pen Style). Ca^{2+} concentration was tested with Salifert Calcium Profi Test Kit and Mg^{2+} concentration was tested was Salifert Magnesium Test Kit.

A Dremel tool was used for incising abalone shell into pieces to prepare the samples.

3. Experiments

3.1 Mesolayer Growth

3.1.1 The Improvement of The Traditional Flat Pearl Method

The Flat Pearl Method is a common method used for investigating nacre growth [54, 59-61]. Thus, it is practiced in our lab to study the mesolayer growth. The micro cover glass slides were used as substrates based on these related literatures. These literatures indicate that the glass substrates could be completely covered by the mantle around the end of the first week after the implantation. Thus, the approximate growth time for nacre could be determined.

In our lab, there are 10 tanks with each tank occupied by 3-4 abalones. Nacre grows through Flat Pearl Method for 5 weeks under different temperatures to make sure the literature recorded Flat Pearl Method is valid in our lab and could be used for the mesolayer growth investigation. Table 1 lists the data collected through different experiments in the lab.

The collected data in **Table 3** shows that, in fact, it is hard to determine when the mantle and the beginning of nacre growth covered the substrates. In the same tank, abalones would not cover the substrates at the same time. Even for the same abalone, the days needed to cover the substrates also varied in different experiments. For example, under 52^{o}F, nothing grew on the glass slides for the 1st week. For the 2nd week, the results from two experiments were very different (19.969μm and 19.031μm in experiment 1 and 0.614μm in experiment 2). The nacre thickness data for the 3rd week from three experiments (Exp1, 2, and 3) are 19.500μm, 69.813μm, 17.156μm respectively. And, some samples under this condition have nacre growth while others do not. A similar condition is there for the 4th-week samples (95.063μm in Exp 1 and 16.781μm in Exp 3). The SEM images of the structures on the glass substrates collected at the end of the 3rd and 4th week under 52^{o}F are

shown in **Figure 17** and **Figure 18** as examples respectively. A similar situation also appears in the experiments with the temperature of 50 °F, 54°F, 56°F, and 58°F.

Thus, the relationship between the nacre growth and time is out of control in an individual experiment with this method. The edge of the round micro cover glass slide is sharp and rough (**Figure 20 (c)**), which might hurt the abalone, mantle and affect their health. This will then influence the nacre growth and finally lead to death. The unhealthy abalones have the mantle retraction problem. The inserted glass substrates are unable to be covered by the mantle. Furthermore, the unhealthy abalones cannot be further used in other experiments. A comparison between the normal, healthy condition of the mantle and unhealthy mantle retraction is shown in **Figure 19**. During the experiments, some abalones died due to the unhealthy condition caused by the inserted glass substrates.

T (°F)	Thickness of grown structure (μm)											
	2nd week			3rd week			4th week			5th week		
	Try 1	Try 2	Try 3	Try 1	Try 2	Try 3	Try 1	Try 2	Try 3	Try 1	Try 2	Try 3
50	-	-	-	6.900	-	-	67.031	-	-	-	-	-
52	19.969, 19.031	0.614	-	19.500	69.813	17.156	95.063	-	16.781	-	-	21.281
54	-	27.295, 32.594	-	20.906, 31.969	10.550	-	-	39.750	-	-	-	-
56	21.938, 20.625, 18.797, 18.891	-	-	60.094, 108.08	-	-	29.063, 22.708	-	-	-	-	-
58	-	-	23.813, 18.375	-	-	22.688, 14.531	-	-	34.063, 38.906	-	-	19.031

Table 3. *The thickness of nacre grown on the glass substrates under different temperature through Flat Pearl Method data collection.*

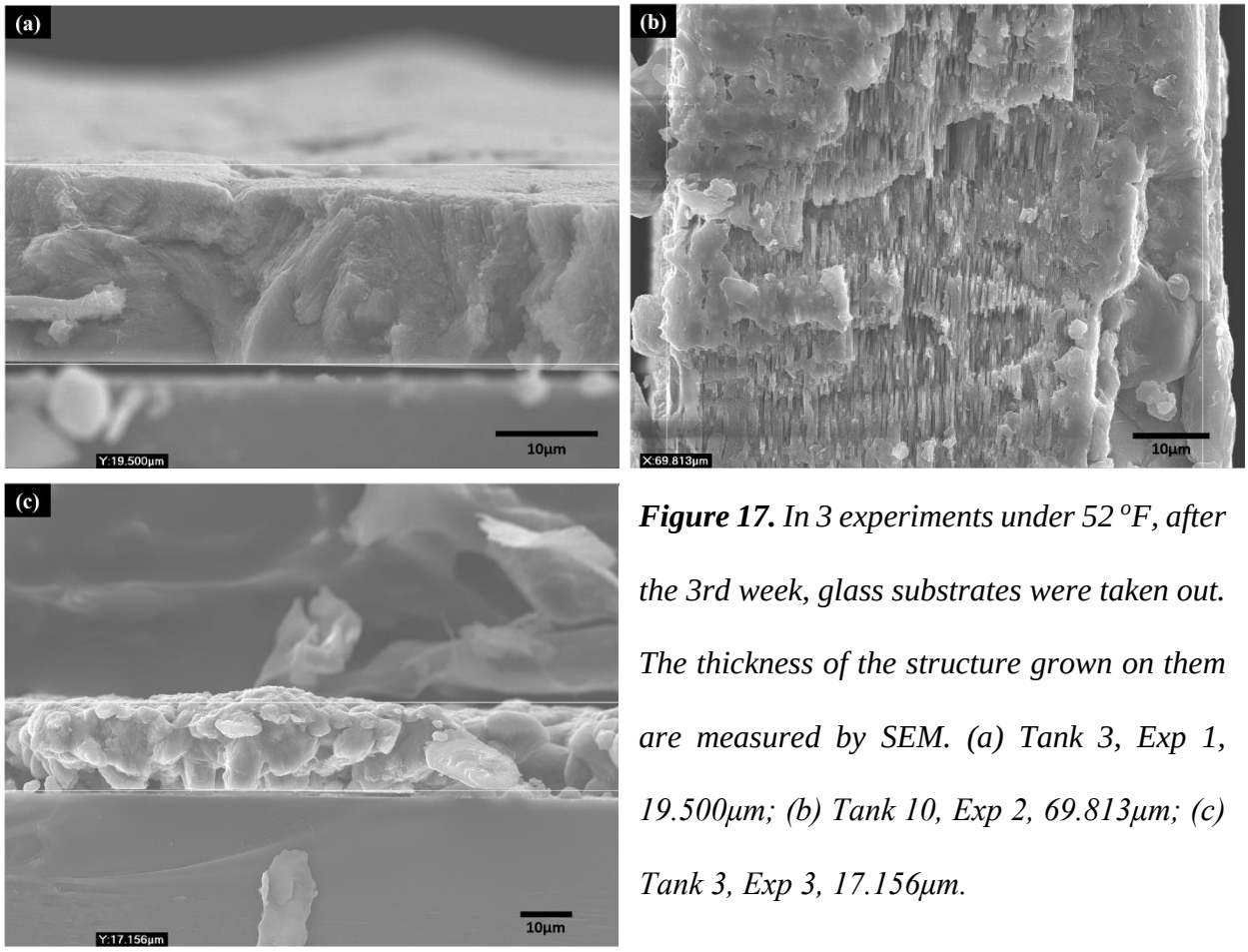

Figure 17. *In 3 experiments under 52 °F, after the 3rd week, glass substrates were taken out. The thickness of the structure grown on them are measured by SEM. (a) Tank 3, Exp 1, 19.500µm; (b) Tank 10, Exp 2, 69.813µm; (c) Tank 3, Exp 3, 17.156µm.*

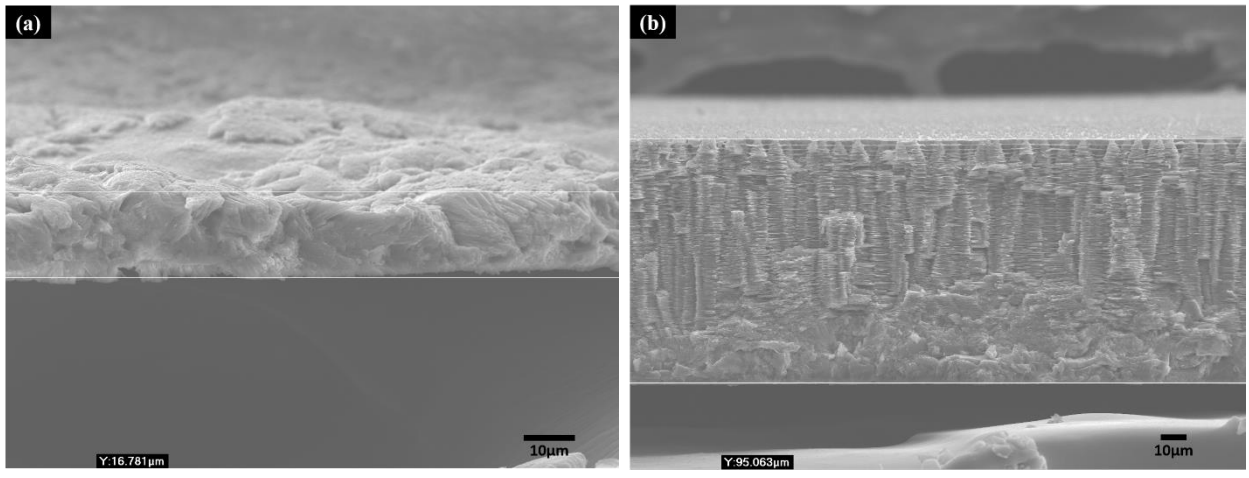

Figure 18. *SEM images of two samples collected after the 4th week from two independent experiments applied on the same tank at 52 °F. The thickness of the structure is measured. (a) Tank 3, Exp1, 95.063µm; (b) Tank 3, Exp 3, 16.781µm.*

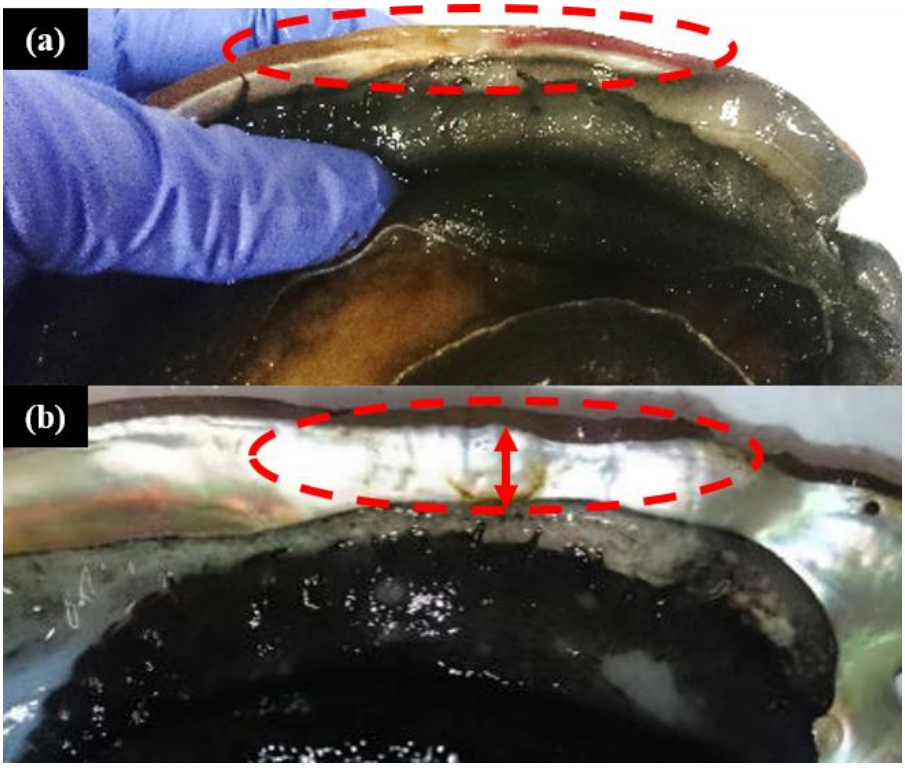

Figure 19*. Comparison between (a) normal mantle in healthy condition and (b) mantle retraction due to an unhealthy condition.*

To improve this situation, a substrate with smaller area and smoother edge which is no hurting to the abalone's body should be introduced into the experiment. In this research, the calcite substrates (**Figure 20 (a)** and **(b)**) prepared with the outside portion of abalone shell was used in this method to replace the glass substrates. The calcite portion of abalone shell is used as the the raw material for the new substrate because that it is easy and low-cost to obtain. With the smooth, sloped edge and controllable size, these substrates did not hurt the abalone and were more easily accepted by them than in the earlier experiments. Thus, more valid nacre growth data could be collected from them.

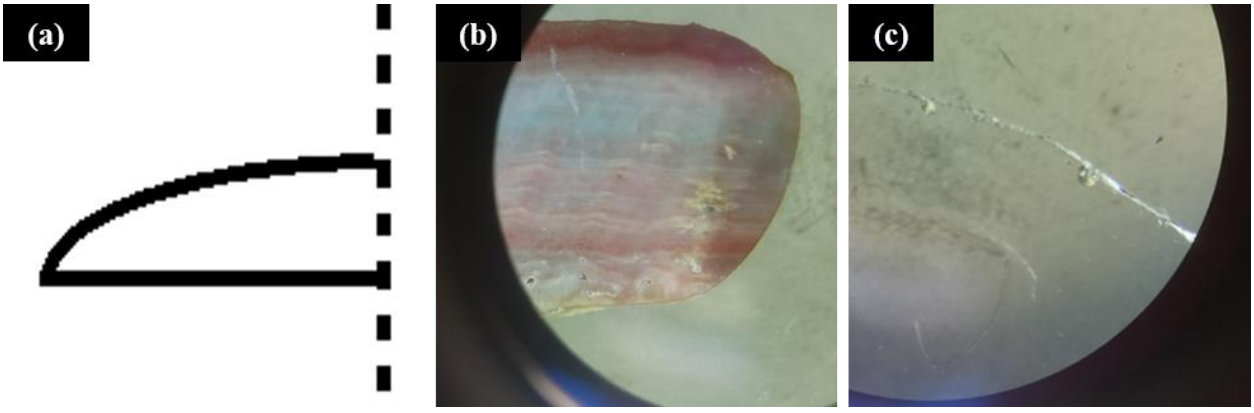

Figure 20. *The material of the slide is improved. (a) Draft of the expected edge of the prepared calcite substrate; (b) the edge of prepared calcite substrate used in experiments; (c) the edge of the glass substrate used in the traditional Flat Pearl Method.*

3.1.2 The Relation between The Environment Factors and The Mesolayer Formation

During the experiments for improving the Flat Pearl Method, grown nacre samples were collected from the constant temperature experiments, which lasted for 4-5 weeks. By characterizing with the SEM, most of them only show the initial block structure and some of them show the tablet built structure. For these that show the tablet structure, no mesolayer structure was found. **Figure 21** shows the examples with the tablets structure collected from the constant temperatures applied in the tanks. Although only one example of each temperature is shown here, all the samples are characterized and no mesolayer could be found.

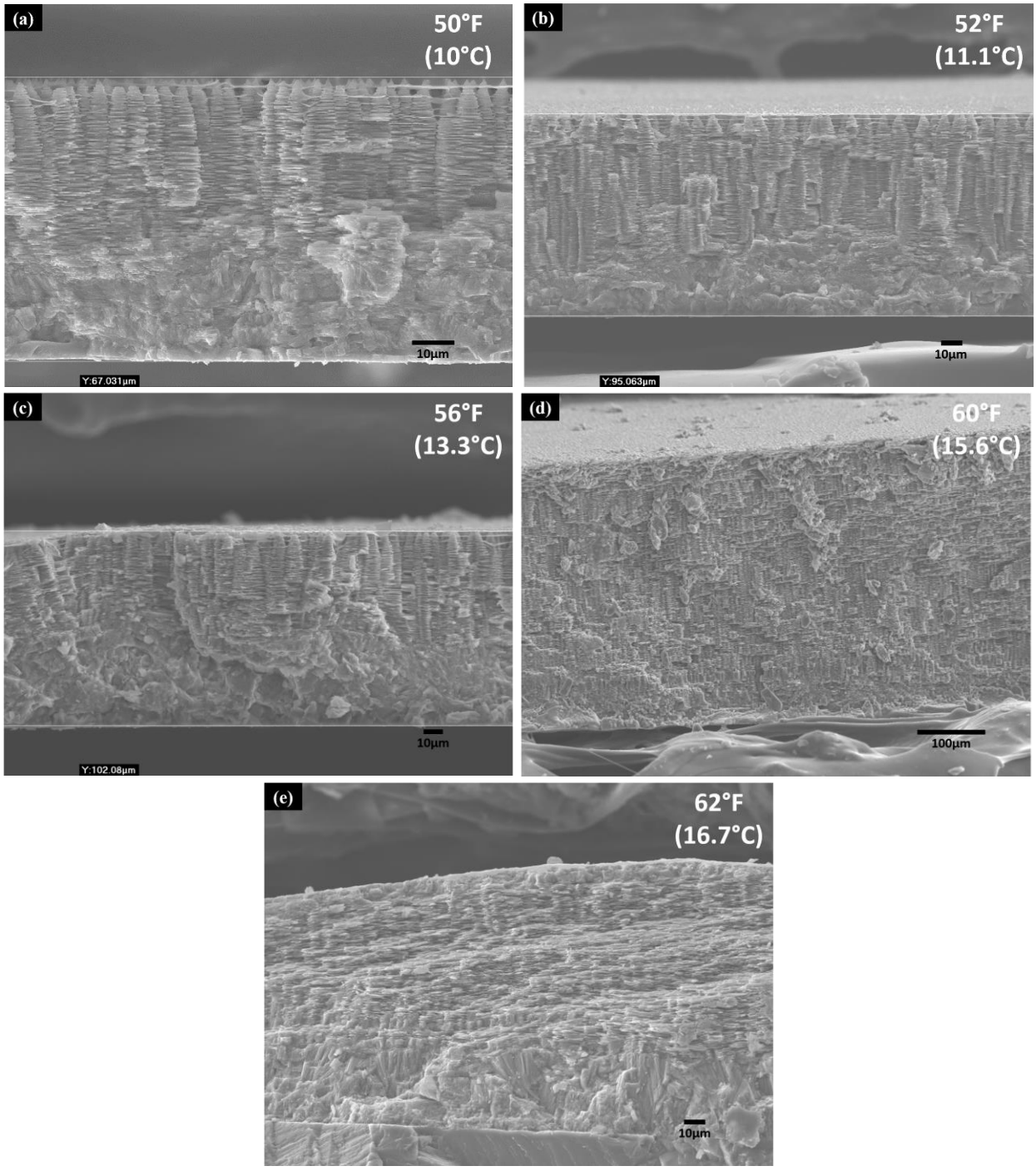

Figure 21. *Nacre samples collected from the constant temperature experiments which is kept at around: (a)50ºF (10ºC); (b)52ºF (11.1ºC); (c)56ºF (13.3ºC); (d)60ºF (15.6ºC); (e)62ºF (16.7ºC).*

3.1.2.1 Mimic the temperature changing in nature

Since there are many layers of the mesolayer appearing in the wild abalone nacre and no such structure found in the constant temperature environment, some periodical repeated physiological change of the abalone is expected. The physiological activities of the abalone could be affected by the environmental conditions. For the mesolayer, it has been determined that the growth starts from the columnar-like layer. And, the columnar-like layer is believed to be made of the calcite rather than the aragonite [25]. Thus, a transition from aragonite to calcite is expected to occur when the mesolayer starts to grow. It has been stated that the temperature, pH, Ca^{2+}, and Mg^{2+} concentration of the seawater all have the possibility to influence the type of calcium carbonate formed in the sea. These parameters influence each other and the concentration of Mg^{2+} and Ca^{2+} is temperature dependent. The Ca^{2+} resource for the abalone could either be the Ca^{2+} in the seawater or the food. As the available Ca content in the food is limited, there is a high possibility that the Ca^{2+} concentration around the abalone in the seawater plays an important role in influencing the nacre and mesolayer growth.

Based on the statement above, it is reasonable that temperature changes caused by seasonal cycles is a possible reason causing mesolayer formation. Abalone could experience several such cycles during its entire life. It is also true that the Mg^{2+}/Ca^{2+} ratio could be changed due to other reasons. For example, geologic events could change the mineral element content of the seawater. However, it is almost impossible for the abalone to live through several geological periods. Another example is that the variation of CO_2 concentration in the air above the sea. But, this CO_2 concentration might not change as regularly as the temperature cycle caused by season change. Thus, the temperature is assumed as the main factor related to the mesolayer growth and it became the main controlled parameter in the lab. Although it has been introduced in the Introduction section that the high

temperature is beneficial for calcite formation while the low temperature has the advantages for aragonite formation in the sea, the nacre grows in a confined environment, which is isolated from the outside sea environment. Thus, the "decrease temperature" and "increase temperature" experiments are both included in the research to determine how nacre growth is affected.

In one of the experiments, the temperature is kept at around 15ºC for 4 weeks and decreased to 9ºC. After 3 weeks, the temperature is increased back to 15ºC and kept at there for another 3 weeks. SEM characterized all the samples and the mesolayer was not found, but some random interruption layers were observed on the top area of the sample such as the structure shown in **Figure 22 (a)(b)**. And, another attempt was done with a narrower temperature change range at a higher temperature level than the previous experiment which was changed from 16.7ºC to 14.4ºC and then back to 16.7ºC. Samples were collected and characterized with SEM. The SEM images of one of the samples is shown in **Figure 22 (c)(d)**. Again, there was no mesolayer structure but some prismatic structure and block structure in calcium carbonate. The results show that the decrease temperature is more likely to produce the block-like interruption structure in the nacre. Then, the opposite temperature change, i.e. the "increase temperature" experiment was done in the lab to see the structure growth behavior.

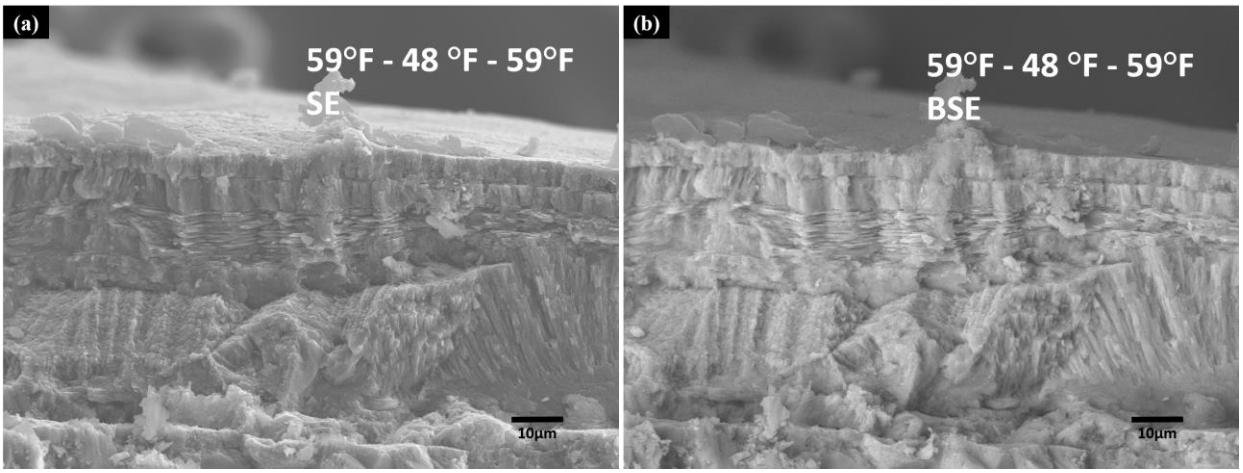

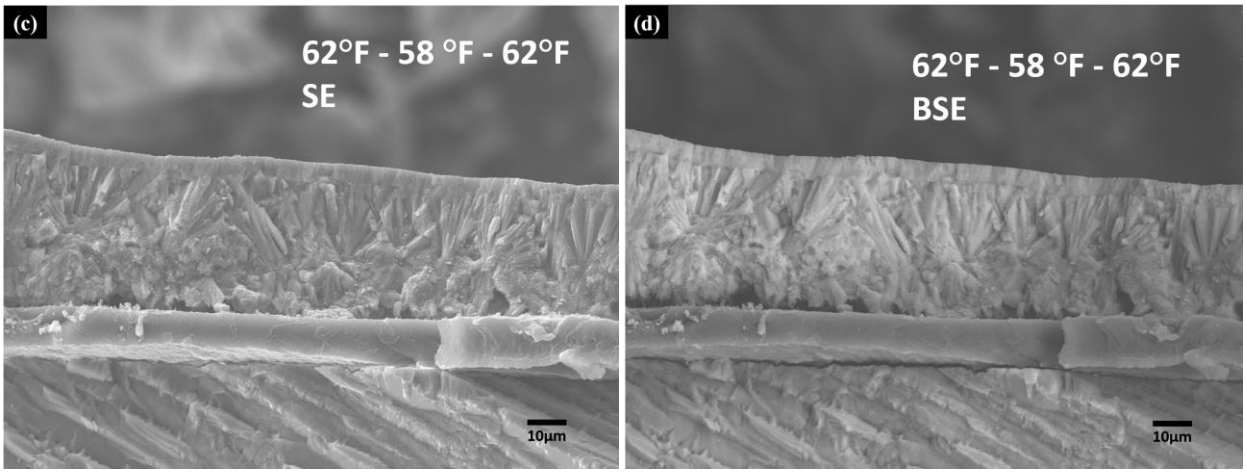

Figure 22. *Samples are collected obtained from Tank No.9 which the temperature is decreased from 15ºC to 9ºC and then back to the 15ºC. The SEM images of one of the collected sample are shown: (a) The SE SEM image; (b) the BSE SEM image. Samples are collected obtained from Tank No.3 which the temperature is decreased from 16.7ºC to 14.4ºC and then back to the 16.7º. The SEM images of one of the collected sample are shown: (c) The SE SEM image; (d) the BSE SEM image.*

Parameters related to the calcium carbonate formation, i.e. the temperature, pH, Ca^{2+} and Mg^{2+} concentration, of the artificial seawater in the lab were tested and recorded every day during experiments for analyzing their relation with the mesolayer formation.

After many experiments, with the improved Flat Pearl Method applied on the California red abalone in the lab, the collected data shows that this improved method is valid when applying to the investigation of the mesolayer growth in a specific period. Two experiments for growing the mesolayer are applied. One is increase the temperature from around 12ºC to around 16ºC and the other is increased from 12ºC to around 20 ºC. This serves to mimic the season change in nature. All the experiments are finished in 6-10 weeks. The temperature is controlled by the chiller and shows slight fluctuation at both low and high-temperature level based on its working mechanism.

The recorded artificial seawater parameters (temperature, pH, Ca^{2+} and Mg^{2+} concentration) of two of such experiments are plotted along the date and shown in **Figure 23** and **Figure 24** respectively. When the temperature is increased, the pH decreases gradually. During this period, the Ca^{2+} and Mg^{2+} concentration change with the opposite steps. After around one week, the pH of the seawater increased back to its original level, which might be caused by the strong self-adjustment ability. Then, the Ca^{2+} and Mg^{2+} concentration began to wave in the same steps.

When the experiments are completed, the calcite substrates inserted in that confined space between abalone shell and mantle are taken out. Backscattered electron SEM images were taken for them from the cleaved cross-section side (**Figure 25**). The mesolayer structure is observed in these samples. These images show the contrast between the thick organic layer and other parts. Particularly, in **Figure 25 (a)** and **(b)**, the prismatic layer, organic layer and column layer, which are typical structures of mesolayer, are clearly shown. **Figure 25 (c)** shows such a mesolayer structure with the tablet nacre structure above and below it. In the four samples, mesolayers all appear near the bottom part of the whole structure, which may be due to the insufficient normal nacre growth time before changing the temperature. When the mesolayer obtained in the lab is compared with the ones in wild abalone shell, a thickness difference of the organic layer should be observed. In the natural environment, the temperature changes gradually during the season transition. However, in the lab, the temperature was changed within 24 hrs. Besides, the periods for both the temperature transition and constant temperature are much longer in the natural environment than what was performed in the lab. The different temperature change rate and length of the time may lead to the difference in organic layer thickness between the wild abalone nacre and the farm-raised ones.

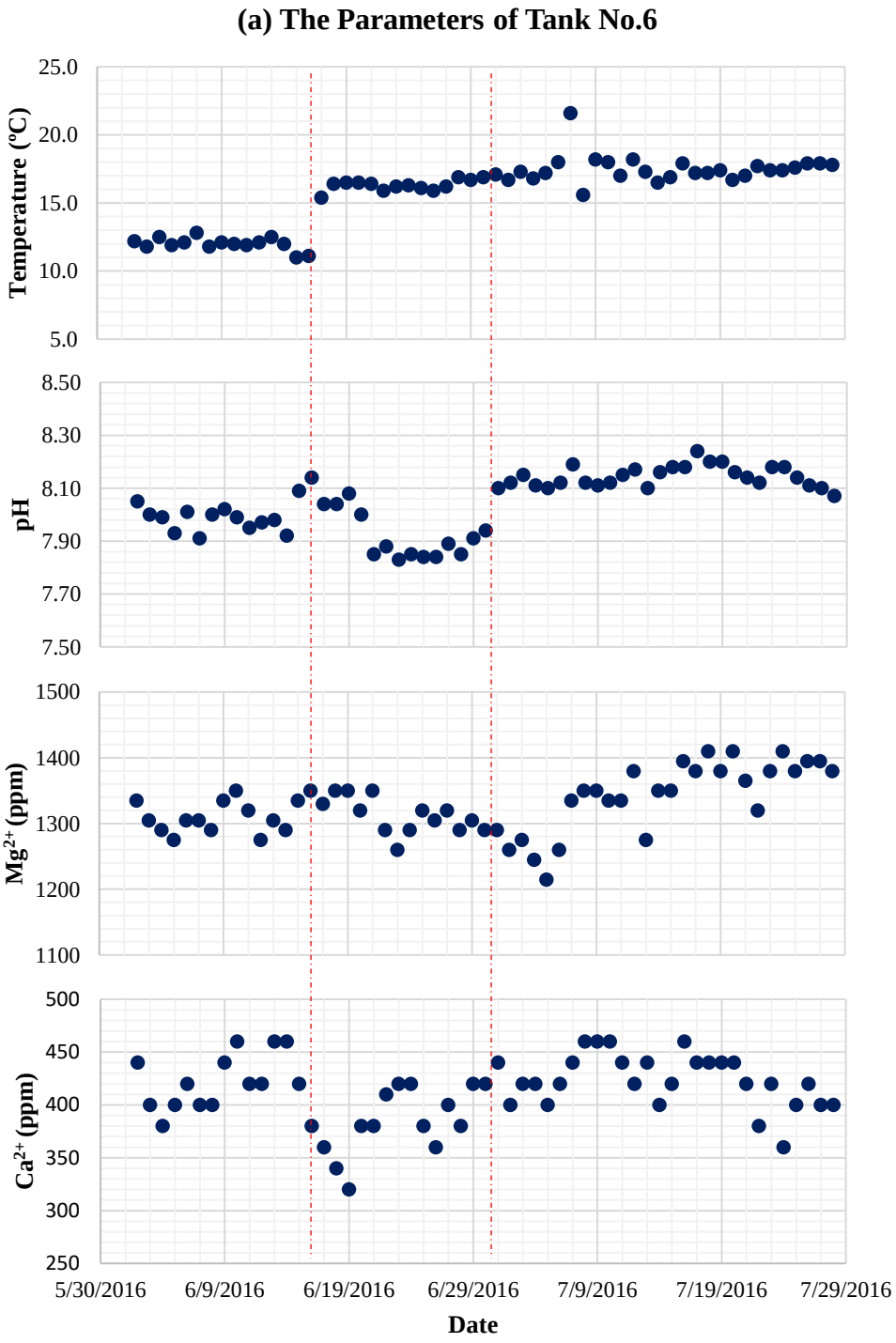

Figure 23. *The trend of temperature, pH, Mg2+ and Ca2+ concentration changing with dates during the "Increase temperature" experiments. (Tank No.6)*

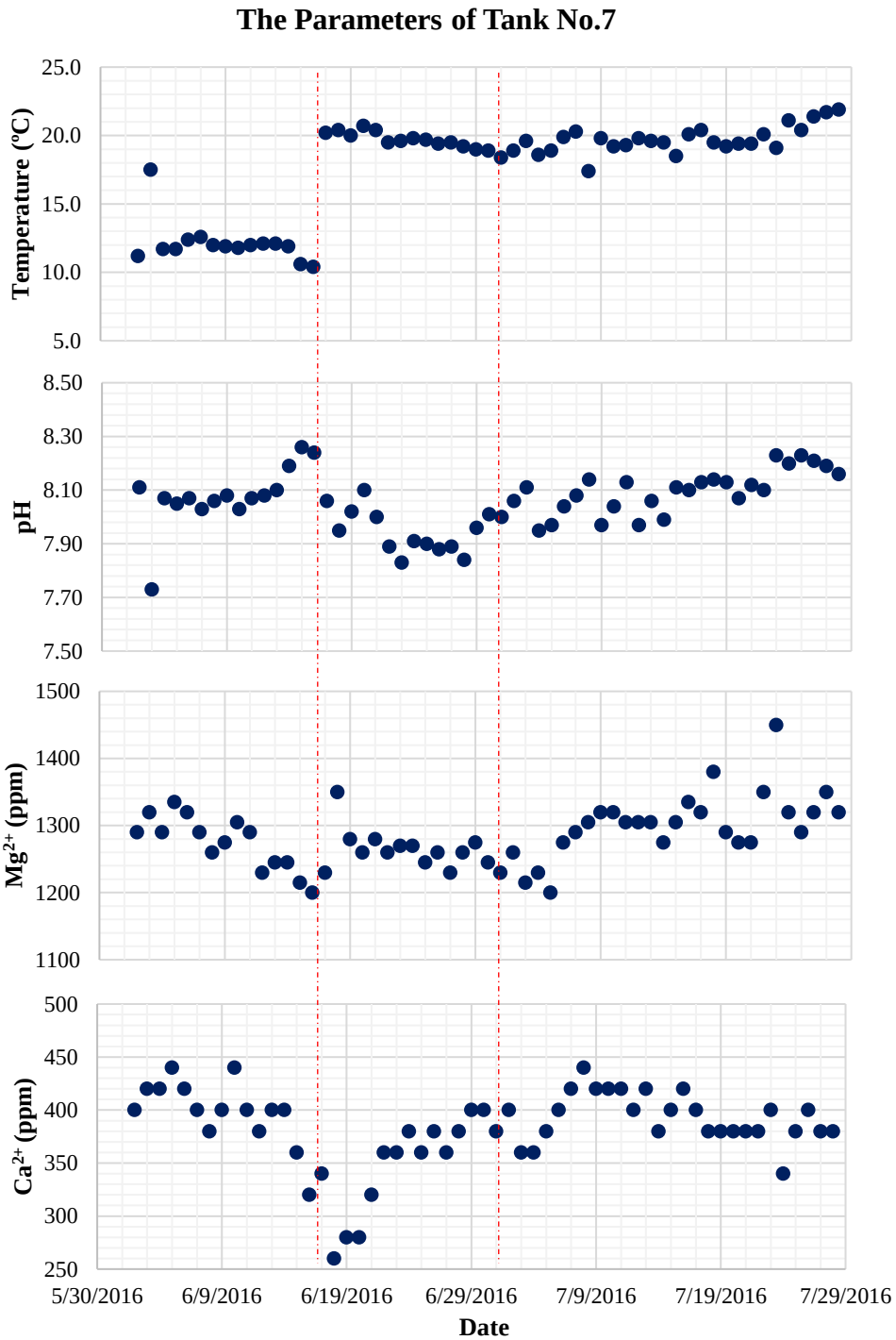

Figure 24. *The trend of temperature, pH, Mg2+ and Ca2+ concentration changing with dates during the "Increase temperature" experiments. (Tank No.7)*

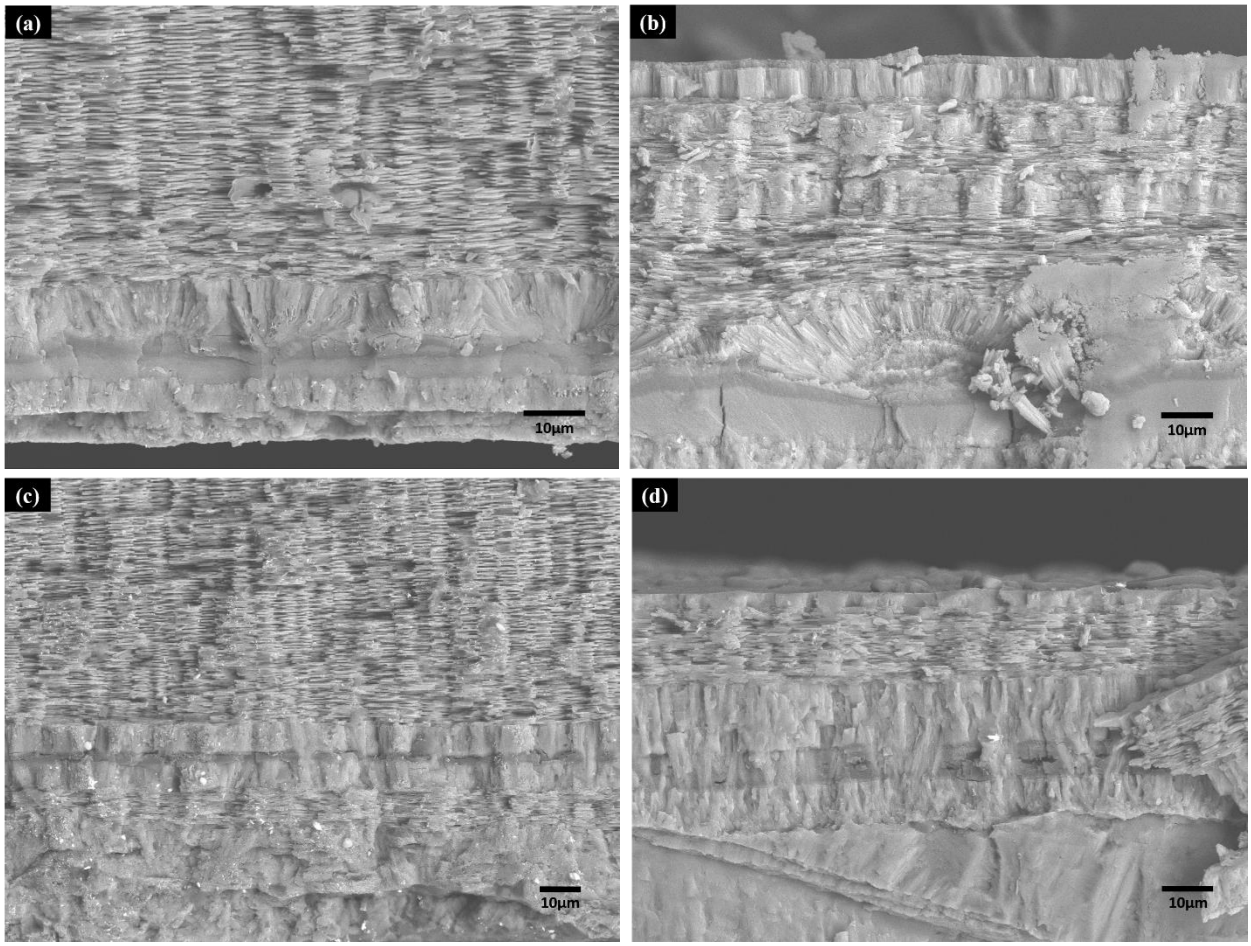

Figure 25*. Backscattered electron SEM images were taken for the samples obtained from the "increase temperature" experiments. Mesolayer could be seen through the typical contrast. (a)(b) two different samples obtained from Tank No.6; (c)(d) two different samples obtained from Tank No.7.All the four samples show the mesolayer structure.*

3.1.2.2 Influence brought by temperature and pH respectively

As the parameters influence each other, it is compelling to observe which factor plays the key role. Thus, another group of experiments are applied to figure it out. The temperature and the pH are the concerning factors since the Ca^{2+} and Mg^{2+} concerntation depends on them. There are two tanks involved in this experiment: one tank (Tank 8) has the temperature increased while the pH

is kept constant; the other tank (Tank 10) is controlled the opposite way. In Tank No.8, the temperature is increased from around 13ºC to 20ºC. When the temperature began to increase, the Na_2CO_3 powder was added into the tank to stop the pH dropping. And, when the temperature decreased back to around 13ºC, the Na_2CO_3 was no longer being added. The pH plot shows that during the high temperature period, the pH always shows a tendency to drop even if the Na_2CO_3 is added. An interesting phenomenon is that the pH began to increase once the temperature was back to the low level despite Na_2O_3 no longer being added. In Tank No.10, adding white vinegar regularly artificially decreased the pH. The pH decreased during the vinegar-adding period and began to increase after the vinegar was no longer being added. The temperature was kept at around 13ºC during the whole experiment, which is the same level as the one for Tank No.8 before the temperature was changed.

Similar to the previous experiments, the data for temperature, pH, Ca^{2+} concentration, and Mg^{2+} concentration was recorded daily. The data collected from Tank 8 and 10 was plotted along the date and shown as **Figure 26** and **Figure 27**. Based on the plot, the Ca^{2+} and Mg^{2+} concentration changed when the temperature and pH altered. For Tank No.8, the Ca^{2+} concentration is decreased when the temperature began to increase. After around one week, the Mg^{2+} concentration started to increase. For Tank No.10, there was no distinctive path of change for the Mg^{2+} except for the random fluctuation. In the meantime, the Ca^{2+} concentration showed a drop-down trend when the pH started to decrease. Under the conditions of Tank No.10, the Ca^{2+} concentration did not increase again when the pH started to increase. Instead, it stayed at a decreased level until the end of the experiment.

The SEM images of the samples collected from these two tanks are shown in **Figure 28**. Two samples are collected from Tank No.8 (**Figure 28 (a)** and **(b)**). The mesolayer structure was found

in one of the two samples (**Figure 28 (a)**). However, in the other sample (**Figure 28 (b)**), although the organic layer could be identified by the contrast in the backscattered electron image, the three sublayers structure were difficult to determine. Additionally, the structure, including the obvious organic layer, was almost at the bottom of the sample. It is hard to tell if this is caused by the changed conditions of the environment. For the samples collected from Tank No.10 (**Figure 28 (c)** and **(d)**), pure calcium carbonate interruption structure was found rather than the mesolayer.

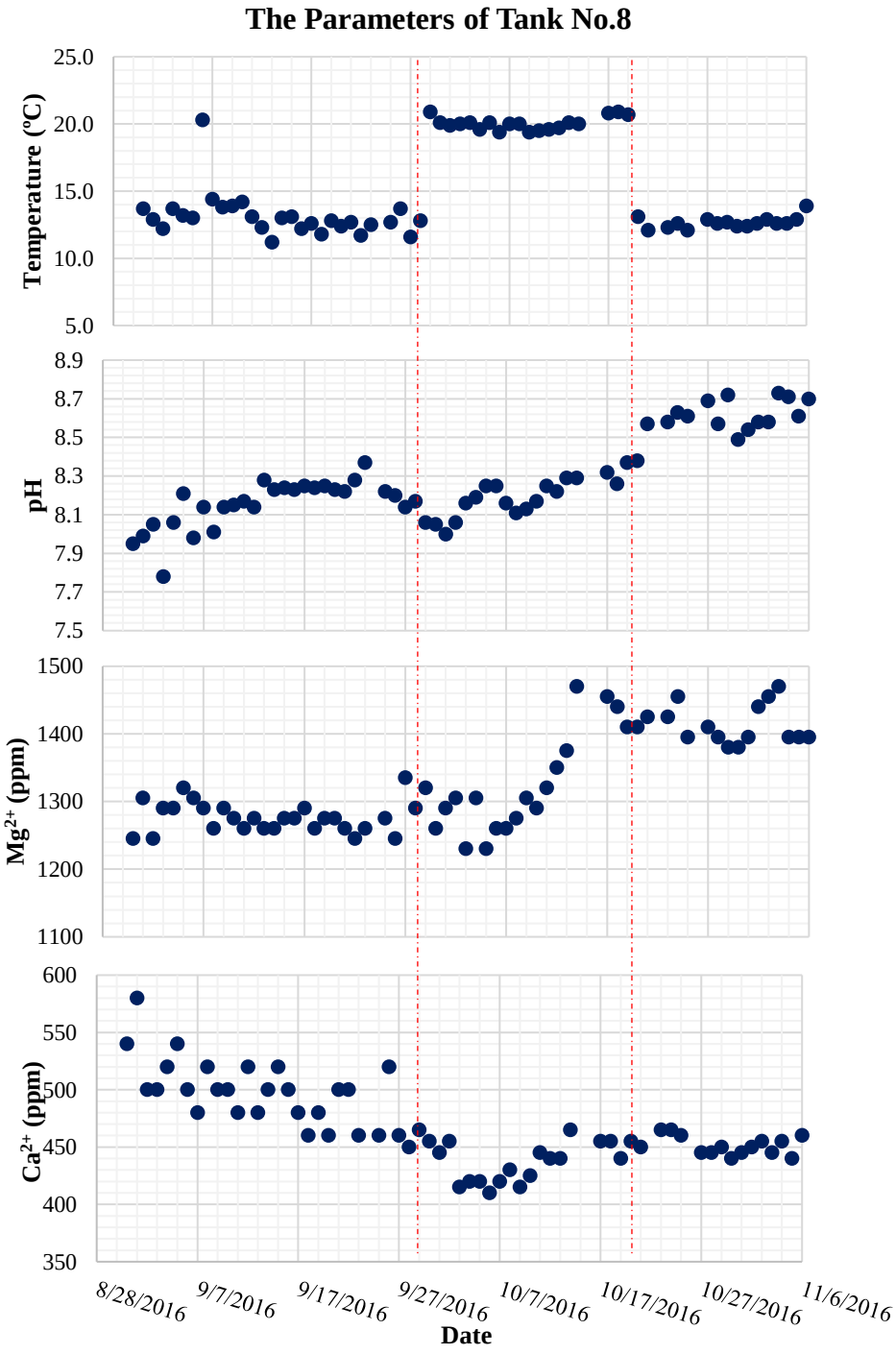

Figure 26*. The comparison experiment to investigate the influence brought by Temperature and pH respectively. In Tank No.8, temperature was increased and decreased back to the original level while the pH was kept above 8.*

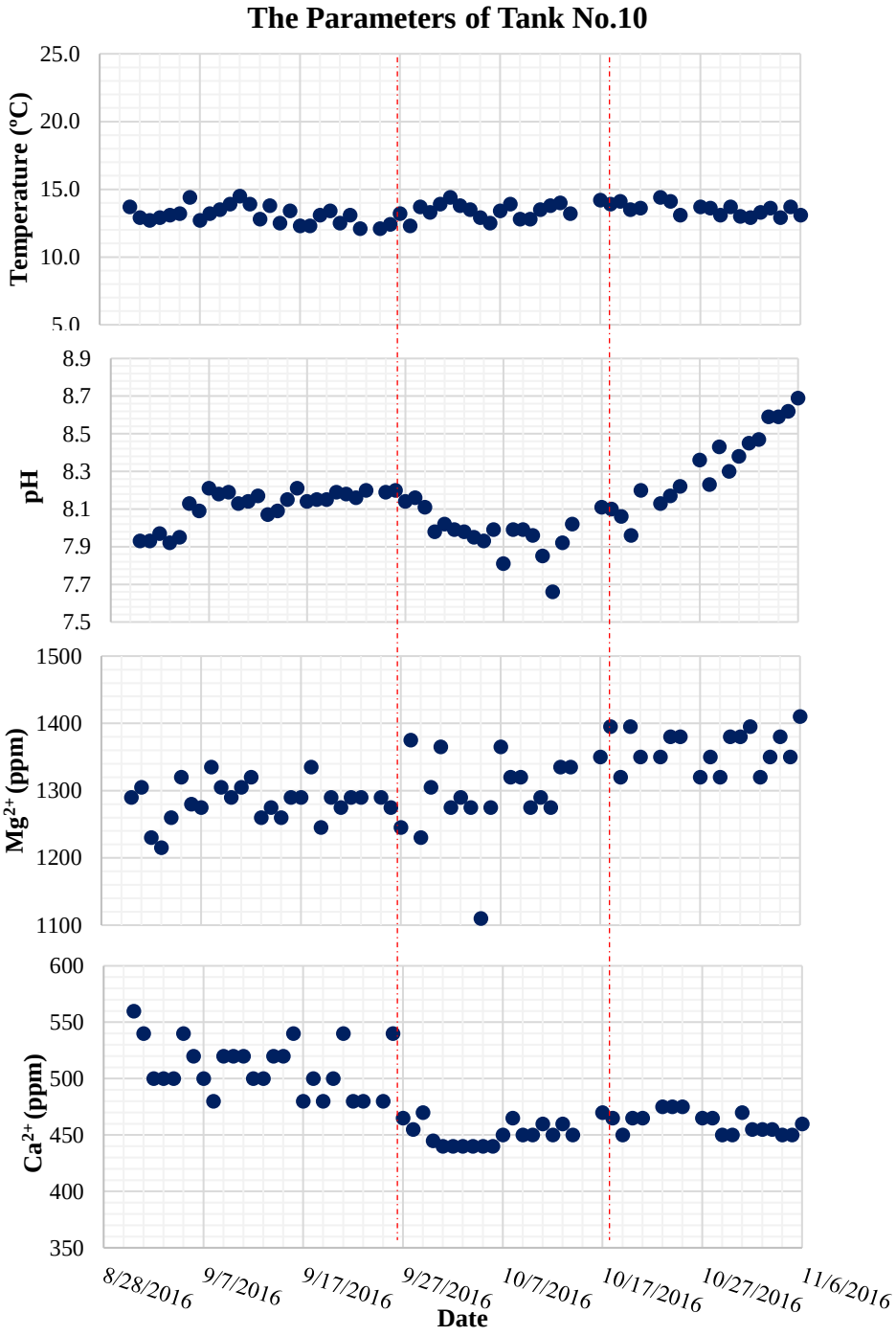

Figure 27*. The comparison experiment to investigate the influence brought by Temperature and pH respectively. In Tank no.10, pH was decreased l lower than 8 and then increased back to the original level while the temperature was kept around 14ºC.*

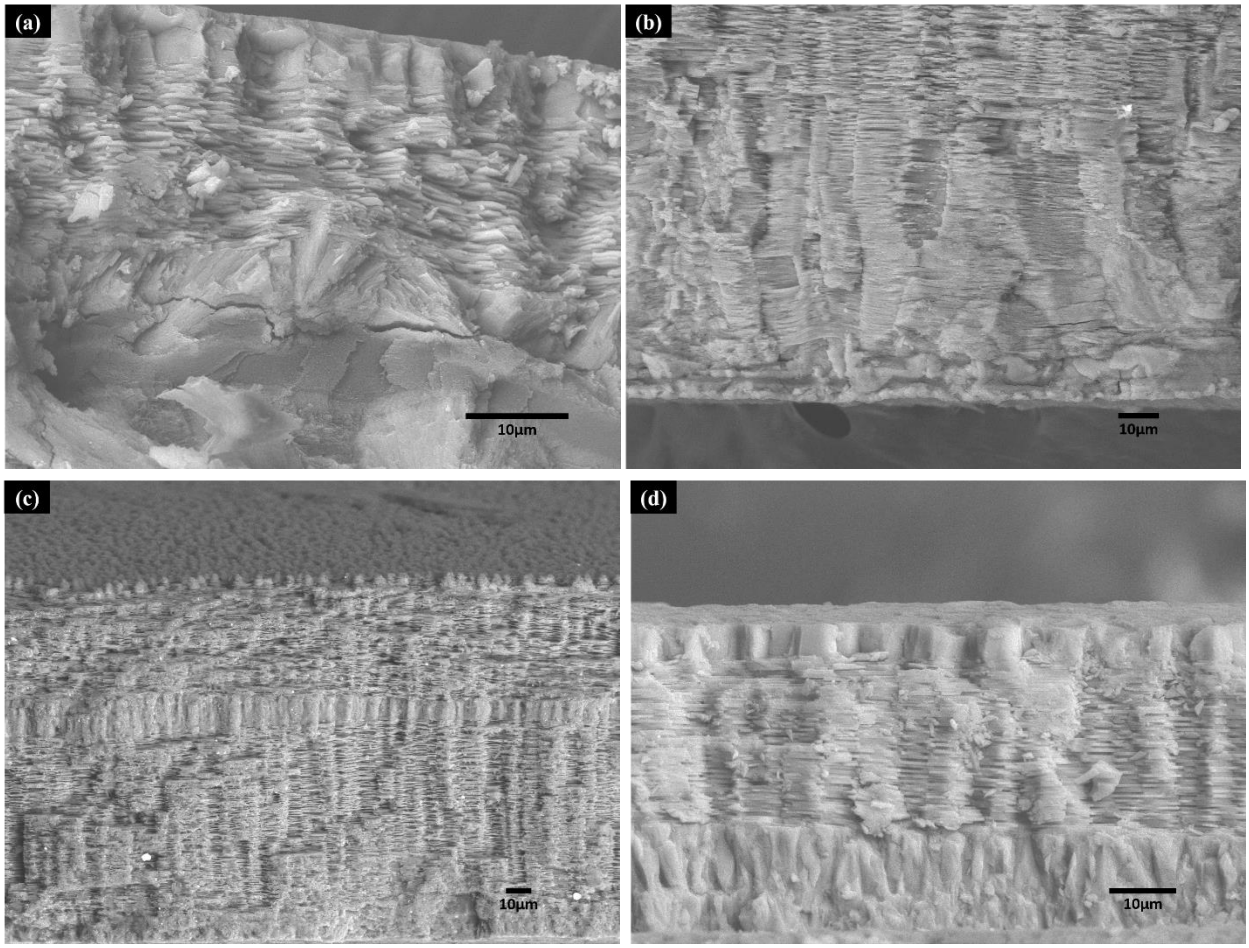

Figure 28. *Backscattered electron SEM images were taken for the samples obtained from the "increase temperature" experiments. Mesolayer could be seen through the typical contrast. (a)(b) two different samples obtained from Tank No.8; (c)(d) two different samples obtained from Tank No.10.*

3.1.3 An Extra Observation Related to The Nacre Growth

It was previously stated that the nacre grows in an isolated environment, which fills up with colloidal mucus. The organic composition in the mucus will eventually become the organic matrix in the mature nacre. In other words, the mucus in that confined space is the immediate environment for the nacre growth. Investigating the mucus could be helpful for understanding the in-depth

details about the nacre growth process. Even though the *in-situ* nacre growth process is hard to observe, a lot of arguments are still present to reveal the truth. The colloidal environment is believed to contribute to the self-assembly process [38][80-82]. Thus, besides the study focusing on the effects brought by the outside environment, some of the mucus is taken out from the nacre growth space in the abalone and dehydrated in a mimicked confined space between two glass slides for the investigation.

To avoid contaminating the sample, both the abalone shell and body were carefully cleaned and dried with a Kim Wipe outside of the water. The mantle attached on the inner side of the shell was slightlty lifted with special lamellar tools. Scratches might induce some tissue cells into the sample, so the 12mm Circle VWR micro cover glass was only placed on the side of the mantle, which is slightly facing the shell, to have some colloidal organic liquid stuck on it. Then the micro cover glass was carefully pulled back and some colloidal organic liquid could be seen on the glass surface, which was in contact with the mantle. The colloidal organic liquid was covered with another micro cover glass. Since only a very small amount of that colloid organic liquid could be obtained through this method, the space between the overlapped micro cover glass could be treated as confined. Waiting for more than 24 hours after placing the sample in the air, the colloidal organic liquid would dry gradually in that confined space. The colloidal organic liquid samples were prepared with liquid obtained from different samples.

After the sample dehydrated completely, SEM images were taken of the remaining solids. Dendrites with various morphologies were observed in these solids (**Figure 29**). Some of them have a continuous body while some others do not. By using the EDS, the composition of these dendrites was determined to be sodium chloride (NaCl). The similar NaCl dendrite phenomenon

was also observed in other studies related to NaCl nucleation in the colloidal environment research [83-85].

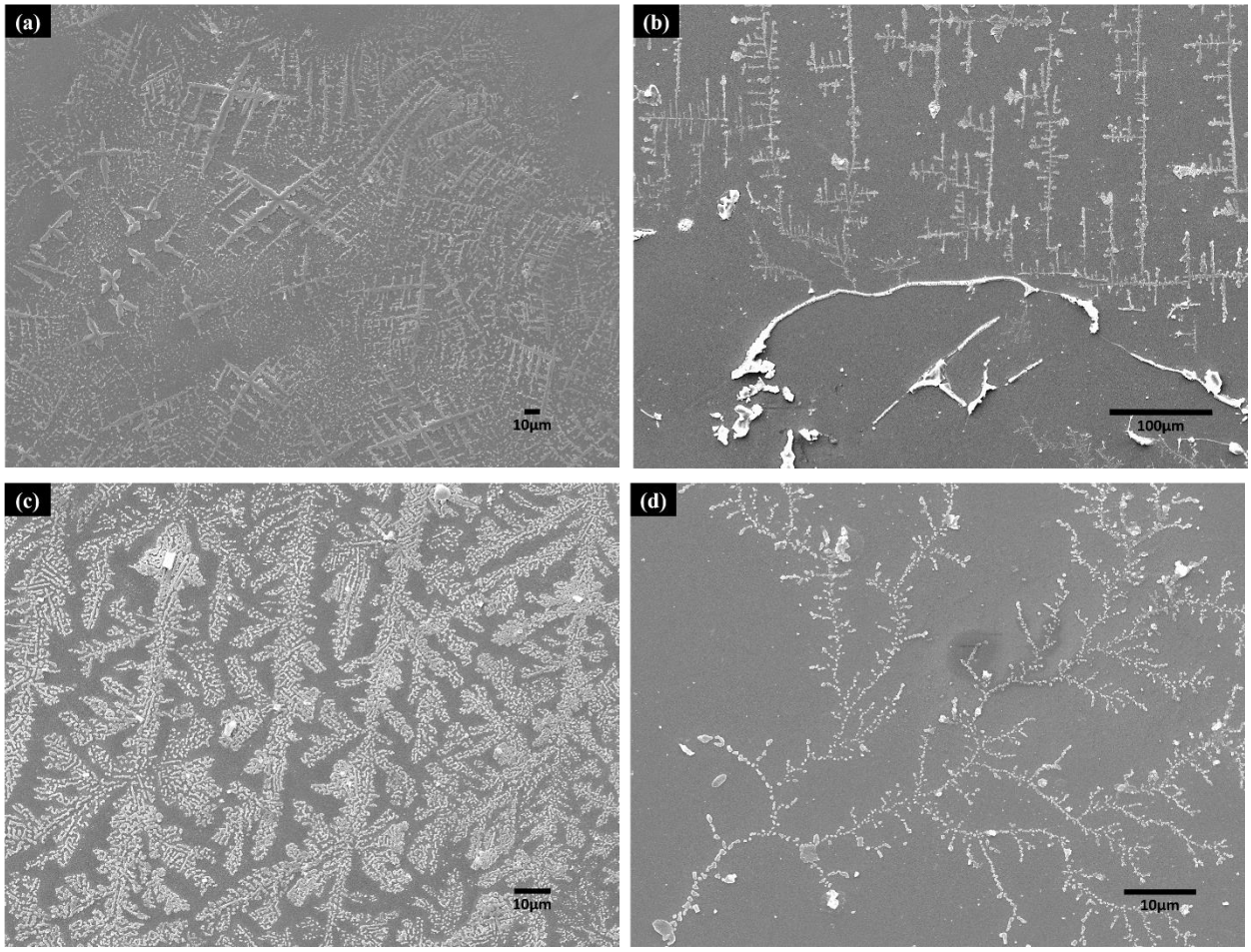

Figure 29*. Different patterns of dendrites nucleated from the mucus in a mimicked confined space where abalone nacre grows in. The composition of these dendrites is determined as NaCl by applying EDS.*

The NaCl crystallization in the mucus is quite different from the one in the normal seawater. An optical microscope image comparison between the NaCl nucleation in the mucus collected from abalone and in the seawater collected from the tank are shown in **Figure 30**. Both of them are dehydrated between two glass slides in the air. The NaCl crystallizes in the normal sea water into the regular shape sheet (**Figure 30 (a)**) while it forms dendrites (**Figure 30 (b)**) in the mucus

produced by the abalone. This comparison might support the idea that the organic colloidal mucus plays an important role in the crystallization with specific morphology.

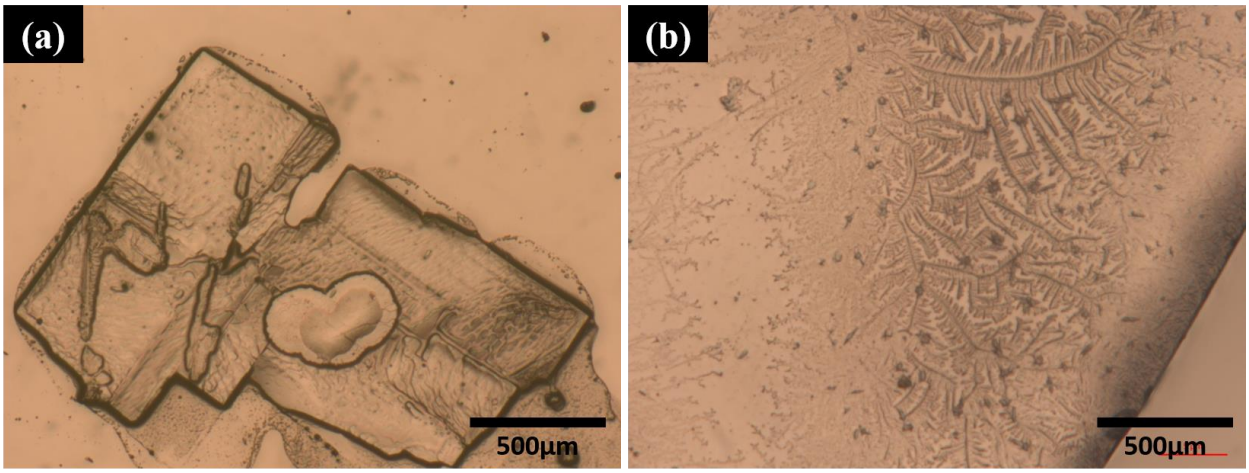

Figure 30. *The optical microscope image of the NaCl crystal formed in (a) normal seawater and (b) mucus of abalone.*

The elements of Mg and Ca, which are related to the calcium carbonate nucleation, were found in bulk with other morphologies. The element of Mg was found accumulated along the organic membrane (**Figure 31**). And, the element of Ca was found in some randomly shaped and distributed micro-scale bulk solid particles. The element of sulfur (S) and oxygen (O) are frequently found existing together with Ca (**Figure 32**). Some special micro-scale hexagonal particles were also observed (**Figure 33**). The existence of Ca, Mg, S, C, and O is determined by the EDS.

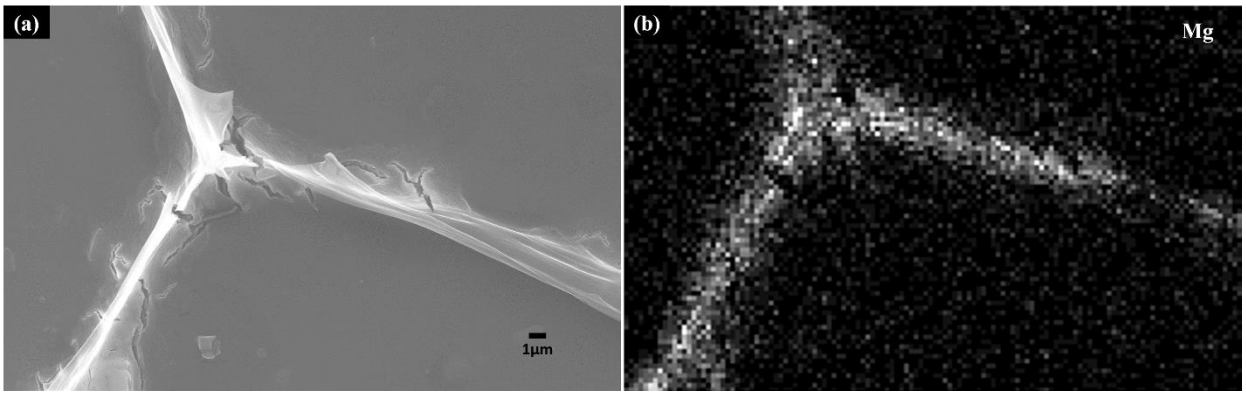

Figure 31. *Some solid accumulated along organic thin film and align in branch-like pattern. (a) The SE SEM image; (b) the EDS mapping shows that the solid includes the element of Mg.*

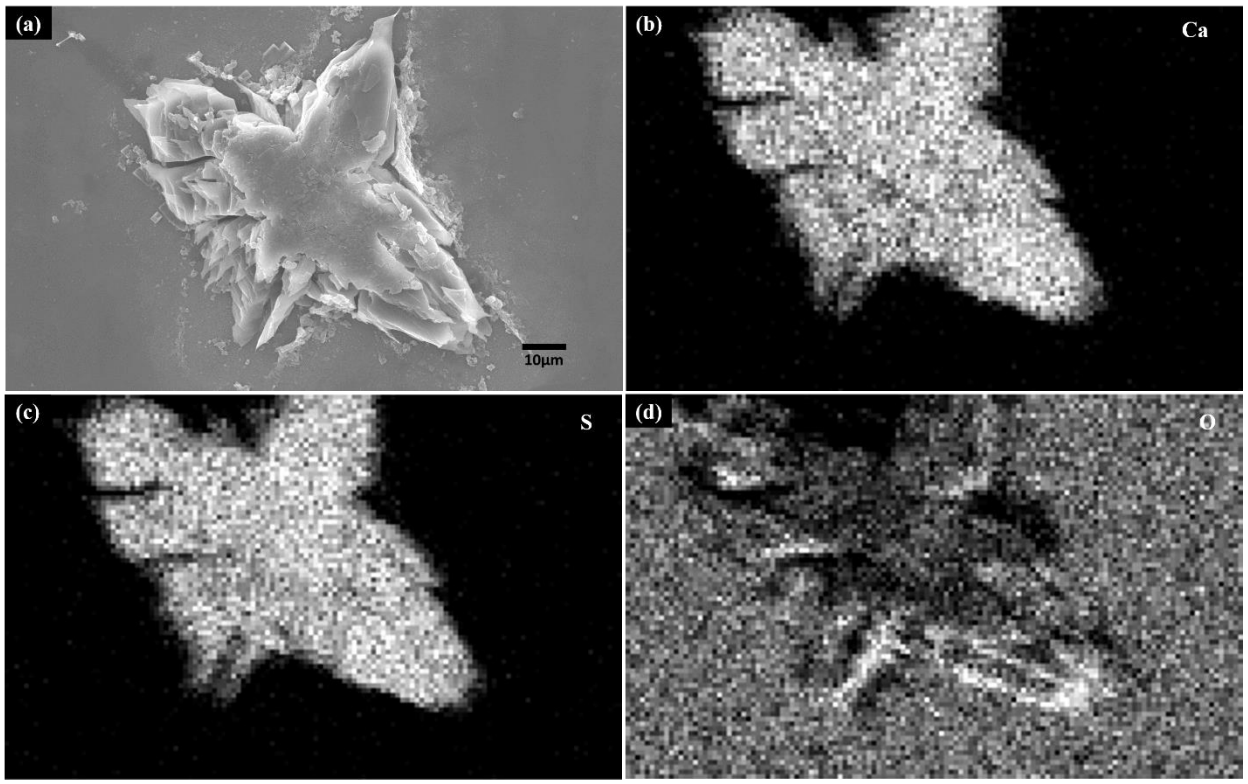

Figure 32. *Some solids accumulate to micro-scale bulk. They are random either in the shape or in the distribution. (a) The secondary electron SEM image of a bulk; the EDS mapping shows that the solid bulk includes the element of (b) Ca, (c) S, and (d) O.*

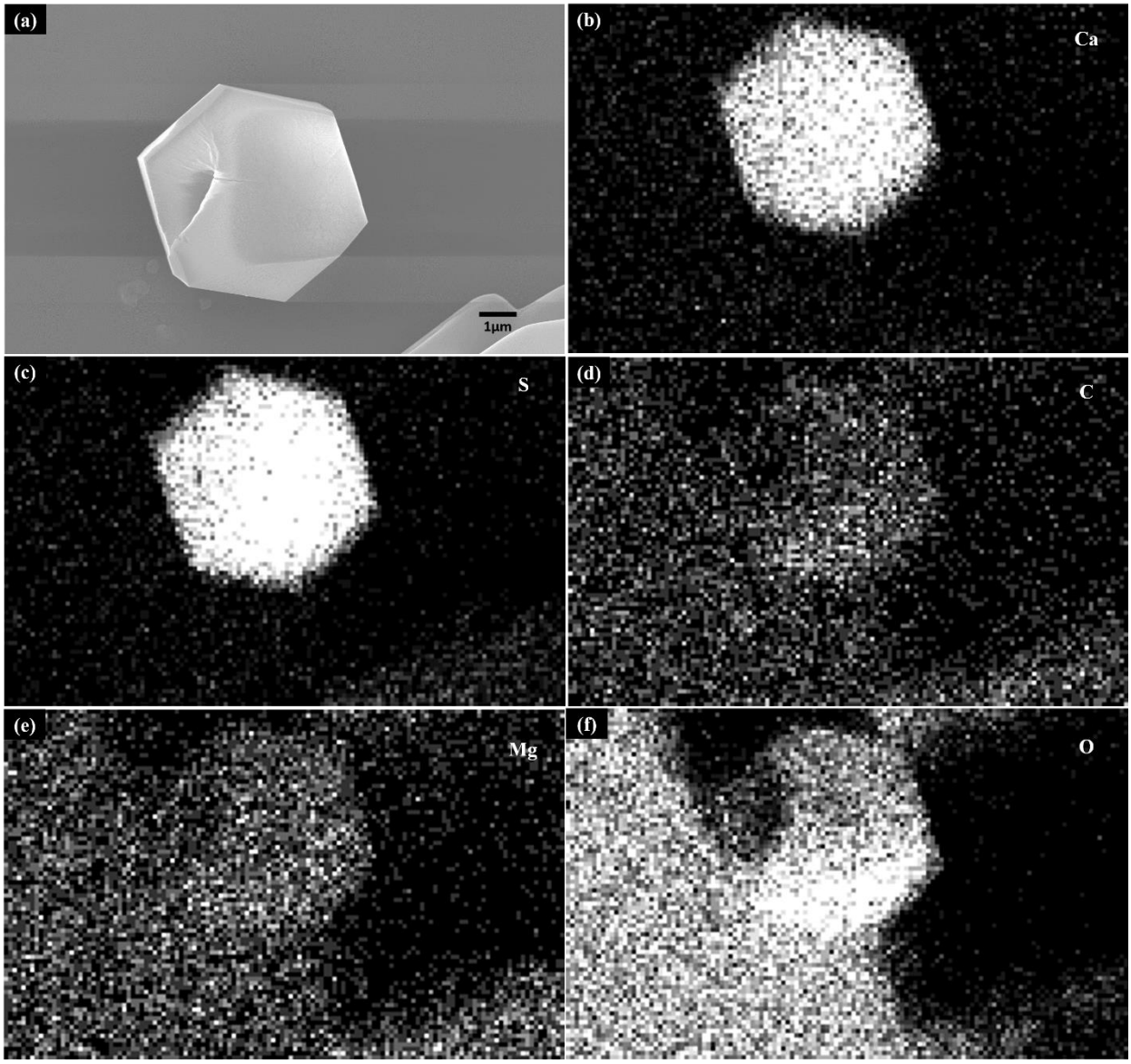

Figure 33*. Some hexagonal particles are found in the dehydrated mucus. (a) The secondary electron SEM image of a bulk; (b)(c)(d)(e) the EDS mapping shows that it includes the element of Ca, S, C, Mg, and O.*

3.1.4 Conclusions

The abalone nacre growth is a quite complicated process still described by many assumptions based on observations.

The experimental results obtained in this research show that the change in outside environment conditions could initiate the change in nacre growth, i.e. the mesolayer formation. When the temperature of the outside environment, i.e. the seawater temperature, is decreased, the mesolayer was not found in the collected samples. In contrast, when the temperature is increased, the samples collected through the Flat Pearl Method indicate that the abalone tend to have a growth transition from aragonite tablet growth to the mesolayer formation during the period of temperature change. The pH and the mineral ion concentration (Ca^{2+} and Mg^{2+}) are recorded daily throughout the entire "temperature-increase" experiment and plotted to observe details. Both the temperature and pH are controlled in a group of similar experiments. The result shows that the seawater temperature is more likely to influence the mesolayer formation.

Simultaneously, it should be addressed that the mucus in the confined space between abalone's shell and the tissue, called the mantle, is the immediate growth environment for the nacre. Thus, the relation between the outside environment and the inside isolated environment could contribute to revealing the growth mechanism of the nacre and mesolayer. When this mucus is taken out of the abalone and dehydrated in a mimicked confined space, NaCl dendrites are found in various patterns. The elements related to nacre growth, Ca and Mg, are found either in some randomly distributed bulk, displaying a random shape, or in some solid with a unique shape, such as the solid accumulated along some organic thin film and aligning in special angles with the hexagonal particles. A similar phenomenon was observed in the studies of the crystallization in the colloidal environment.

More studies focusing on the relationship between the outside and inside environment could be expected to be one possible way to describe the true nacre growth process and explain the mechanism behind this biomineralization process.

3.2 The Mechanical Properties Investigation

As mentioned in the Introduction section, the mechanical properties of nacre are investigated by using the nanoindentation test. The nanoindentation test is primarily used for studying the modulus and hardness of the material. In this research, the elastic property of nacre is important, and the elastic modulus will be discussed, here in.

3.2.1 The Nanoindentation Test Applied on The Mesolayer

The growth of the mesolayer, as well as its mechanical properties, are a main focus of this research. As mentioned before, the mesolayer can be divided into three sublayers: prismatic layer, organic layer, and columnar-like layer. The details about the mechanical properties of each of them are the fundmental for learning about the mechanical property of the whole mesolayer structure and the possible influence on the nacre including the mesolayer brought by the mesolayer. Due to the complex micro-structure, nanoindentation test is an ideal way for investigating the mechanical property for those thin layers.

3.2.1.1 Sample preparation

Wild abalone nacre, as shown in **Figure 2**, has many layers which make up the mesolayer and is ideal for this experiment. Wild abalone shells were cleaved into pieces, then grinded and finely polished into a “Top-side” sample. With its natural waviness, each of the three sublayers of the mesolayer were exposed on the surface through careful grinding and polishing. Although the individual sublayers of the mesolayer cannot be distinguished with the naked eyer from the sample surface due to its scale, the special morphology of the mesolayer can still be discerened when exposed on the surface and placed under light at certain angles.

The sample preparation steps are shown in **Figure 34**. The red, blue and yellow area represent the prismatic, organic and column-like layers respectively. The sample was grinded and polished until the mesolayer was exposed on the sample surface. The red square depicted in step 3 of **Figure 34**, is the same area as depicted in step 4. The difference is that step 3 is a draft of the cross-section side of the sample while step 4 is a secondary electron SEM image taken from the top side of the prepared sample.

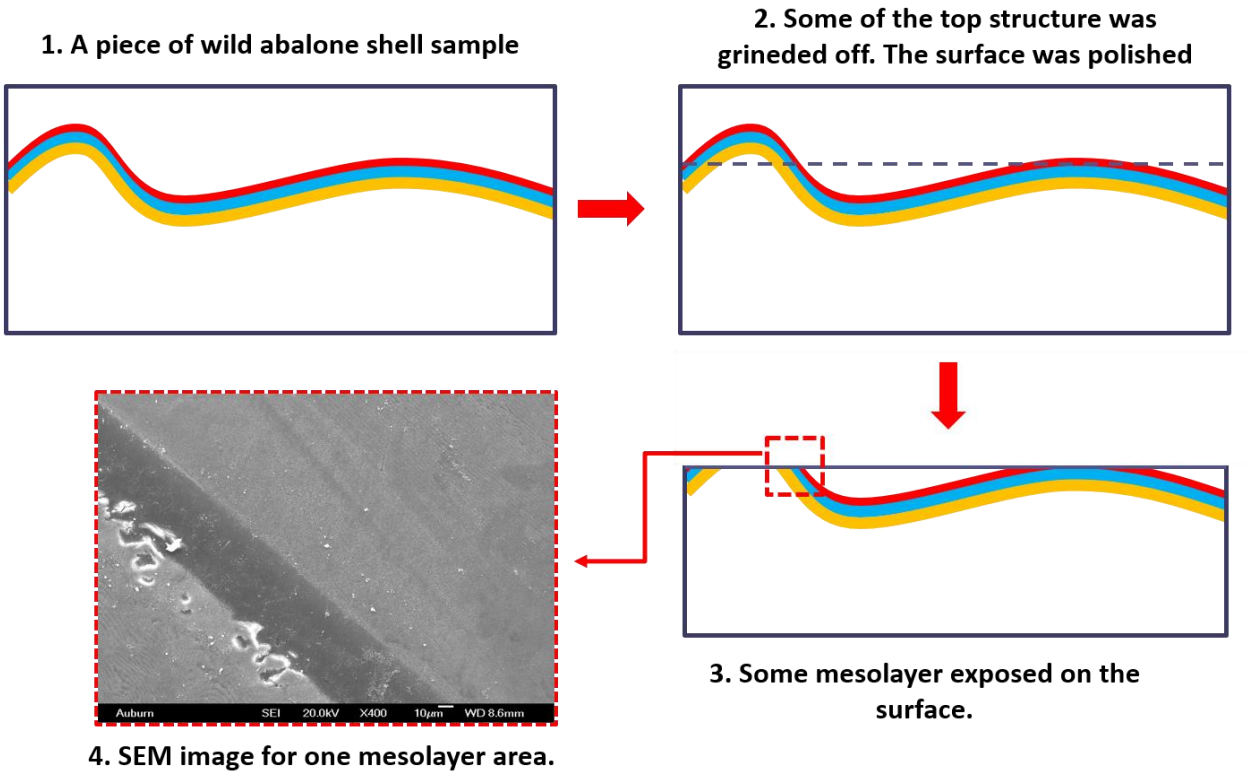

Figure 34. *Grinding and polishing of a piece of wild California red abalone nacre to let the mesolayer be exposed on the sample surface. (a) A mesolayer exists in a nacre sample. (b) The top layer of the material was grinded and polished. (c) Both the organic layer and column-like layer were exposed on the surface. (d) SEM image of the top-down view of the sample surface.*

The three sublayers of the mesolayer could be distinguished from the polished mesolayer surface by the boundry morphology of two separate layers. This could be shown by comparing the polished mesolayer surface and the mechanically cleaved mesolayer cross-section (**Figure 35**). The boundary between the prismatic layer and the organic layer (the green dash line in **Figure 35**) is zigzaged while there is a smooth boundary between the organic layer and the columnar-like layer.

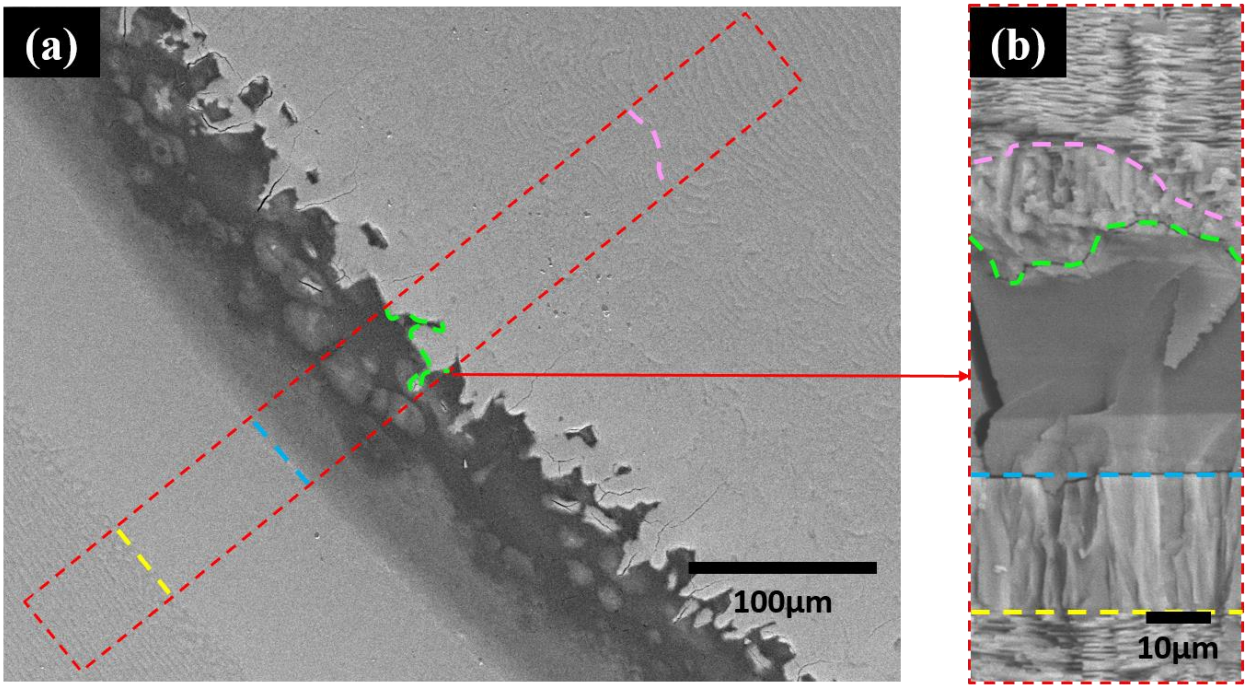

Figure 35*. The comparison between the top-side and cross-section-side SEM image for the mesolayer. (a) The polished mesolayer exposed on the top-side of the wild abalone nacre sample surface; (b) the cross-section of a mechanically cleaved wild abalone nacre sample with mesolayer visible. The pink dash line represents the boundary of the tablets and the prismatic layer. The green dash line represents the boundary of the prismatic layer and organic layer. The blue dash line represents the boundary between the organic layer and the columnar-like layer. And the yellow dash line represents the boundary between the columnar-like layer and tablets.*

When each sublayer of the mesolayer was tested, the optical microscope in the nanoindenter is used for determining the location to apply the test. Although the sublayer structures cannot be identified as clearly as under the SEM due to the low magnification and low resolustion, some boundaries between each sublayer are distinguishible (**Figure 36**). Thus, the nanoindentation tests could be applied on the specfic sublayer area. After the nanoindentation test, SEM images were taken for those nanoindentations to confirm that the tests were applied in the correct area. An existed possibility is that the nanoindentation test is determined by the SEM image that it was not applied within the expected area.

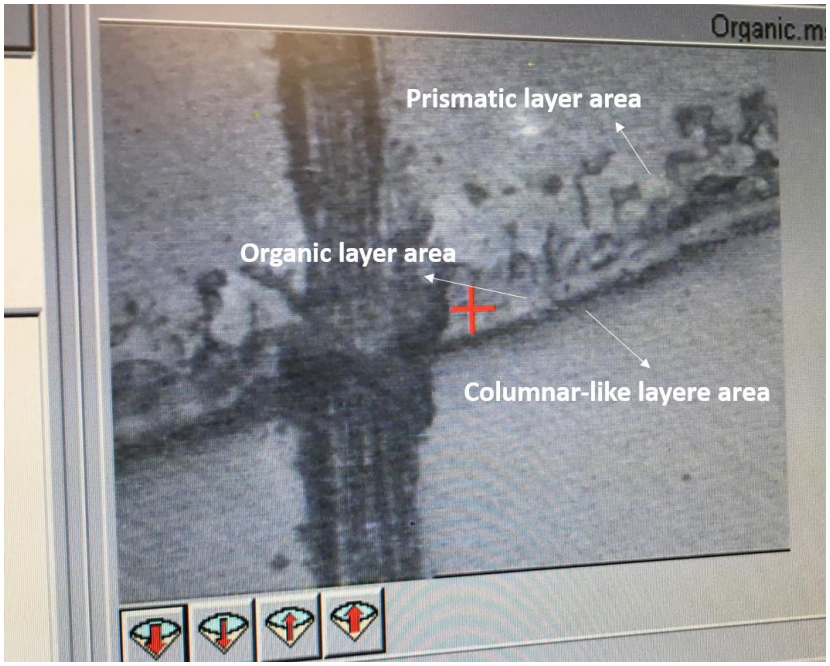

Figure 36. *The mesolayer observed under the optical microscope of the nanoindenter, which is used for determining the location to apply the nanoindentation test.*

3.2.1.2 Testing and Results

Fifteen nanoindentations were applied to each area and the final result for each area was calculated based on all the vaild nanoindentation data in said areas. The calculated final modulus of each

sublayer of the polished mesolayer were then plotted (**Figure 37**). In the tests shown by **Figure 37**, the nanoindentation depth is 1000nm. It can be seen that the modulus of the organic layer continues decreasing while the nanoindentation depth increases. Conversely, the modulus of the columnar-like layer and the prismatic layer increase with increasing nanoindentation depth. It should be noticed that the modulus plots in **Figure 37** are not necesarily stable values. The dynamic stiffness during the loading process for the three structures were ploted (**Figure 38 (a)**). It can be seen that the dynamic stiffness has a polynormial-like relationship with the nanoindentation displacement, rather than a linear one, which is caused by the substrate effect. This indicates that the tested area has an inhomogeneous structure, which is reasonable due to the fact that the mesolayer is built by sublayers being stacked one by one. Also, the three sublayer stuctures are different from each other and are expected to show different mechanical properties. The entire mesolayer structure could be treated as an inhomogeneous material. By comparing the tested loading dynamic stiffness (**Figure 38 (a)**) with **Figure 38 (b)**, the result of the columnar-like layer and the prismatic layer agree with the center case in **Figure 38 (b)**, and the organic layer test agrees with the bottom case in **Figure 38 (b)**.

Figure 34 can be used as a reference for explaining the dynamic stiffness plot. The tested prismatic layer area has the organic layer, which is soft and supposed to show a lower modulus than the calcium carbonate, under it. This is similare to the case shown in the center of **Figure 38 (b)**. The organic layer has the columnar-like layer under it and is similar to the case shown at the bottom of **Figure 38 (b)**. The dynamic stiffness plot for the columnar-like layer shows the similar curve to that of the prismatic layer. Since the nacre tablet structure exists underneath, this columnar-like layer is expected to show a higher modulus than that of just the tablets. Images of the nanoindentations on the three sublayers corresponding to the modulus shown by **Figure 37** were

taken (**Figure 39**). It should be mentioned here that, even if it is carefully polished, the tested area is not perfectly flat and smooth due to its natural features. Thus, some of the individual nanoindentations did not produce vaild data and the nanoindentation might not show the perfect equilateral triangle shape, such as the one shown in **Figure 39 (a)**. However, **Figure 39 (a)** cannot represents the shape of all the nanoindentations in that area. The final result was calculated based on these vaild nanoindentations.

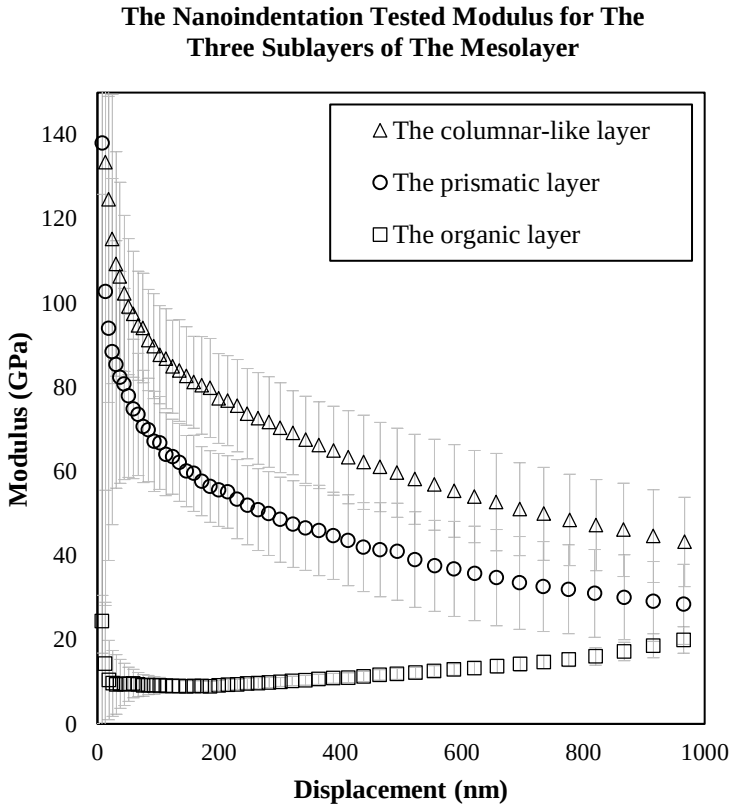

Figure 37*. The tested modulus from use of the nanoindenter of the columnar-like layer, the organic layer, and the prismatic layer of the mesolayer.*

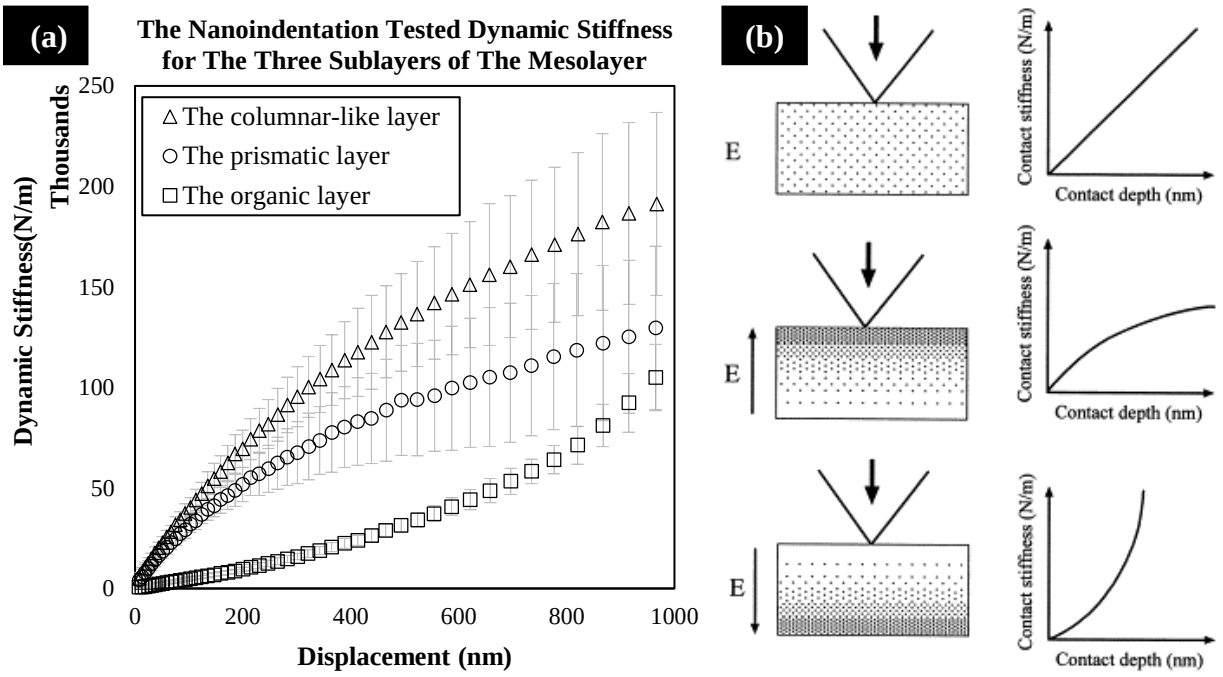

Figure 38*. The comparison between the (a) tested dynamic stiffness of the prismatic layer, organic layer, and the columnar-like layer and (b) the schematic of the relationship between the loading dynamic stiffness and nanoindentation displacement for the homo- and inhomogeneous material. [86]*

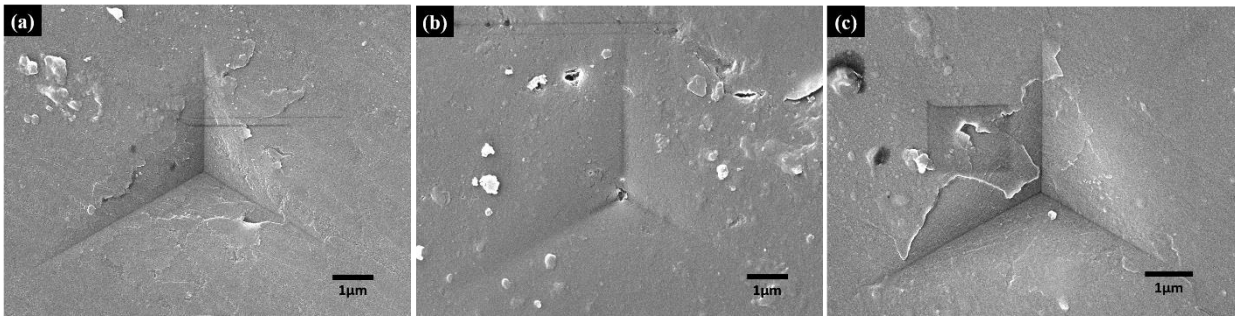

Figure 39*. The secondary electron SEM image of the nanoindentation on the (a) prismatic layer, (b) organic layer, and (c) columnar-like layer.*

3.2.1.3 The Curve-fitting and Discussion

The dynamic stiffness data was curve-fitted through the least square method by using Python. The curve-fitting plot is shown in **Figure 40**. During the curve-fitting, the stiffness is forced to zero at the displacement of zero, due to no stiffness being expected when the displacement is zero. Based on the Taylor's expansion, those data could be fitted into a curve represented by a polynomial function, and the polynomial functions for the three sublayers in one of the experiments are listed in **Table 4**.

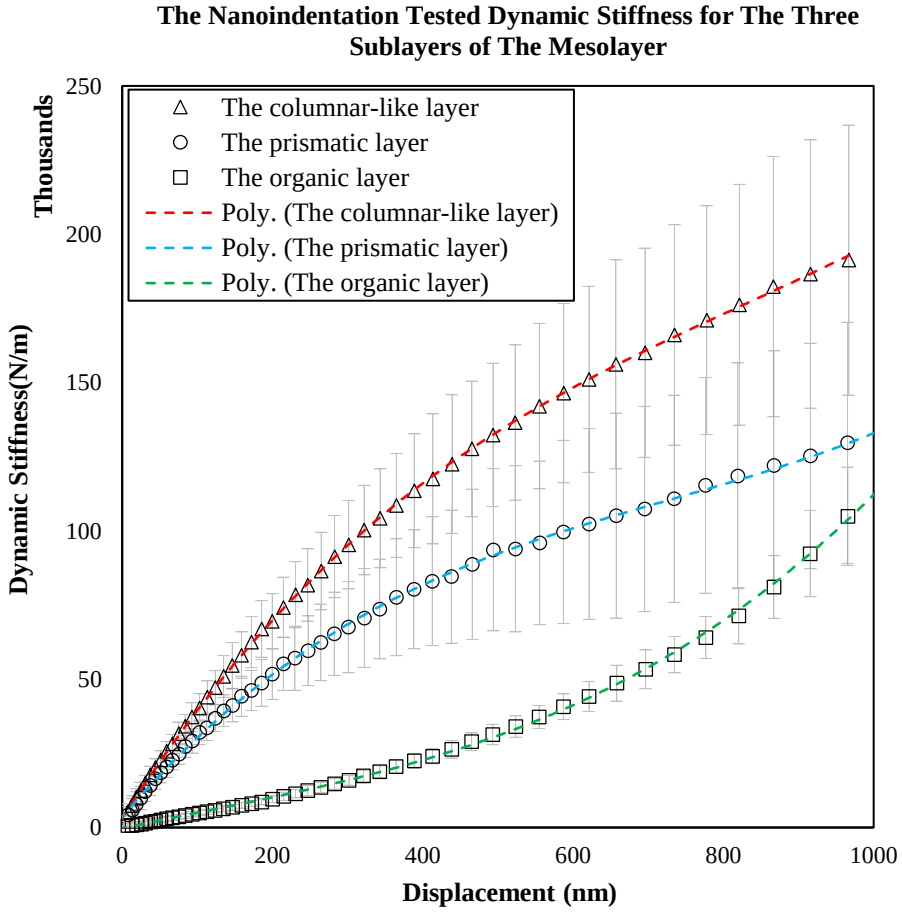

Figure 40*. The curve-fitting for the dynamic stiffness data of the prismatic layer, organic layer, and the columnar-like layer of the mesolayer. The curve-fitting is based on the least square method.*

Layer Name	Polynomial Function
Prismatic Layer	$s = 321.2x - 0.3552x^2 + 0.0001672x^3$
Organic Layer	$s = 68.93x - 0.06900x^2 + 0.0001131x^3$
Columnar-like Layer	$s = 415.4x - 0.3740x^2 + 0.0001560x^3$

Table 4*. The polynomial function of the dynamic stiffness vs. displacement plot for the prismatic layer, the organic layer, and the columnar-like layer of the mesolayer.*

As the nanoindenter tip used in this research was a Berkovich tip, the contact between the tip and the sample should be the Sneddon's contact, as introduced previously. However, in reality, the end of the Berkovich tip cannot be perfectly sharp. The end of the tip can be treated simply as a spherical end, and the contact during the first few nanometers should be the Hertz contact, which describes the contact between a sphere and a half free surface [87]. Based on the parameters such as the radius of the tip end (< 50nm) given by the company sharpening the nanoindenter tip, the displacement, that should be treated as Hertz contact, can be determined geometrically. Based on the geometry calculation (**Figure 41**), the relation between the tip end radius and the nanoindentation depth can be described by (**Equation 5**):

$$d = R - R * sin77.05°$$

Equation 5*.* d *= The nanoindentation depth,* R *= The radius of the Berkovich tip end.*

As the radius of the tip end is less than 50nm, the calculation based on **Equation 5** shows that the Hertz contact nanoindentation depth is less than 1.27nm, which is quite a small distance. The Hertz contact can be described by (**Equation 6**) [88]:

$$F = \frac{4}{3} * E_r * \sqrt{R} * d^{\frac{3}{2}}$$

Equation 6. *F = The load during the nanoindentation process, E_r = The reduced modulus of the tested sample, R = The radius of the Berkovich tip end, d = The nanoindentation depth.*

The reference sample for the nanoindenter included in this research is a single crystal SiO_2 which shows a reduced modulus of 69GPa. The test data of the reference sample is plotted together with the Hertz contact curve based on **Equation 6** and various radius values to determine the radius of the tip end (**Figure 42**). The test data of the reference sample below the displacement of 25nm is used here. In **Figure 42**, the colorful solid line is the Hertz contact equation curve based on various sphere radii. It should be noticed that none of the solid lines match the test data in the range of 10nm~25nm displacement. Below 10nm, limited amounts of data were collected, and it is difficult to compare the Hertz contact equation curve and the test data.

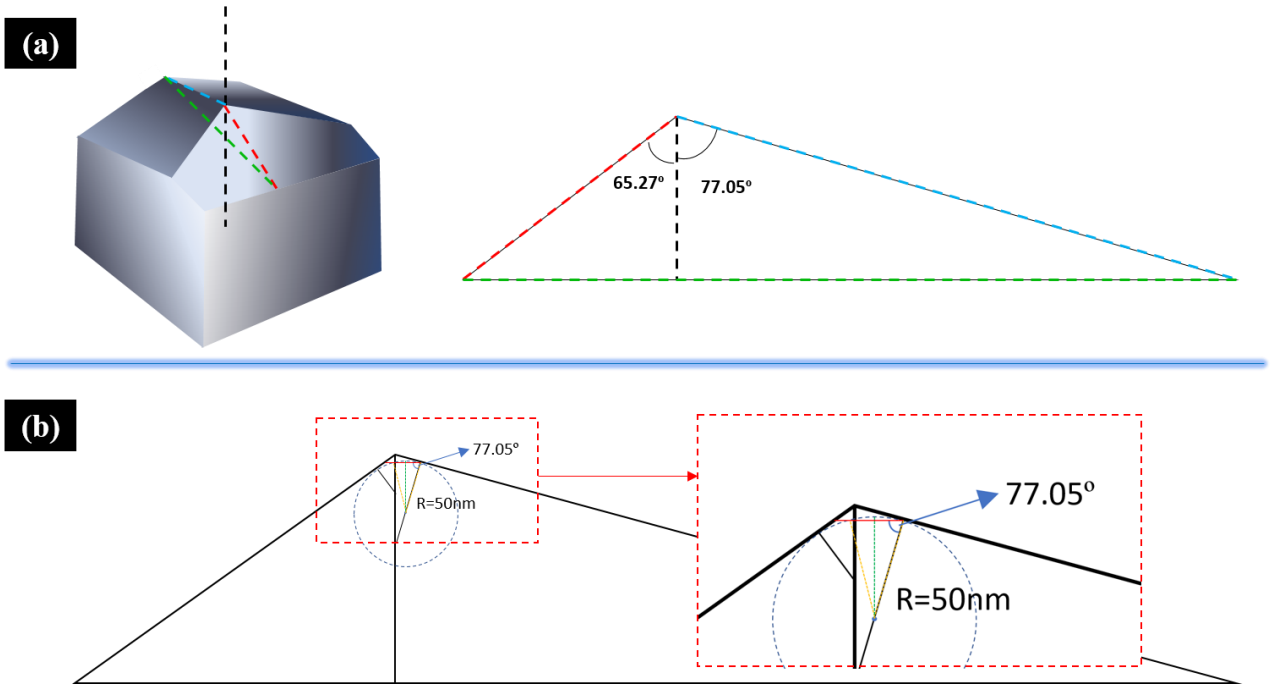

Figure 41. *The (a) geometry and (b) geometry parameters of the Berkovich tip used in this research. The Hertz contact range were calculated based on this geometry analysis.*

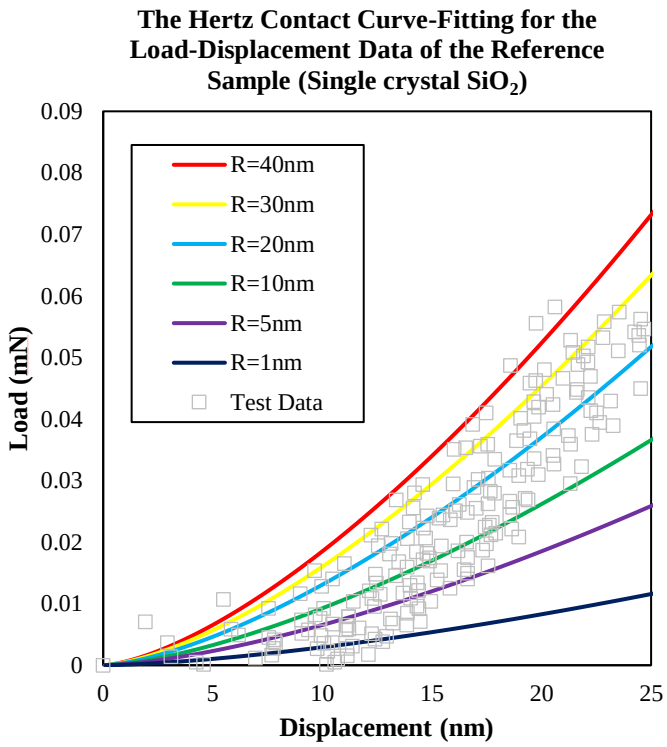

***Figure 42**. The plot showing the test data of the reference sample (single crystal SiO_2) and the Hertz contact equation curve based on various sphere radii.*

Based on geometrically calculated data and the comparison between the reference data and the Hertz contact equation curve, it could be concluded that the role played by Hertz contact is quite limited. Thus, the curve-fitting shown in **Figure 42** could be treated as a perfect Berkovich contact.

The truth, in fact, is the tip end has complex geometry and the contact is much more complicated [89-90]. But, to simplify the problem, this complex tip end will not be a concern in this work.

The calculation for the modulus of each sublayer in the mesolayer could then be determined by combining the curve-fitted polynomial function, the Sneddon contact equation (**Equation 1**), and the area function of Berkovich tip (**Equation 2**). The calculation for the prismatic layer is shown here as an example to demonstrate the process:

$$s = 321.2x - 0.3552x^2 + 0.0001672x^3 = \frac{2}{\sqrt{\pi}} E_r \sqrt{A} = \frac{2}{\sqrt{\pi}} E_r \sqrt{24.5x^2}$$

Using Taylor expansion to simplify:

$$321.2x = \frac{2}{\sqrt{\pi}} E_r x \sqrt{24.5}$$

Then, the value of the reduced modulus E_r was determined to be 57.51GPa.

By applying this calculation, only the very beginning of the nanoindentation process is considered, and the assumption applied here is that the substrate effect is ignored at the very beginning part of the nanoindentation test. Thus, the modulus of prismatic layer could be calculated by applying Equation 3 which describes the relation between the reduced modulus and the elastic modulus. The Poisson's ratio of the prismatic layer is assumed as 0.3 here. Then, the modulus of this structure is calculated as 52.33GPa.

Besides the calculation stated above, the Zhou-Prorok model [69] is also used for fitting the modulus of the prismatic layer based on the tested modulus (**Figure 43**). This fitting, based on the Zhou-Prorok model results, shows the modulus of the prismatic layer as 54GPa. The Poisson's ratio of the prismatic layer is 0.3 in the Zhou-Prorok model fitting.

The elastic modulus value of the prismatic layer resulting from the two different methods are comparable.

(a) **The Comparison of The Zhou-Prorok Model Fitted Curve and The Tested Modulus of The Prismatic Layer**

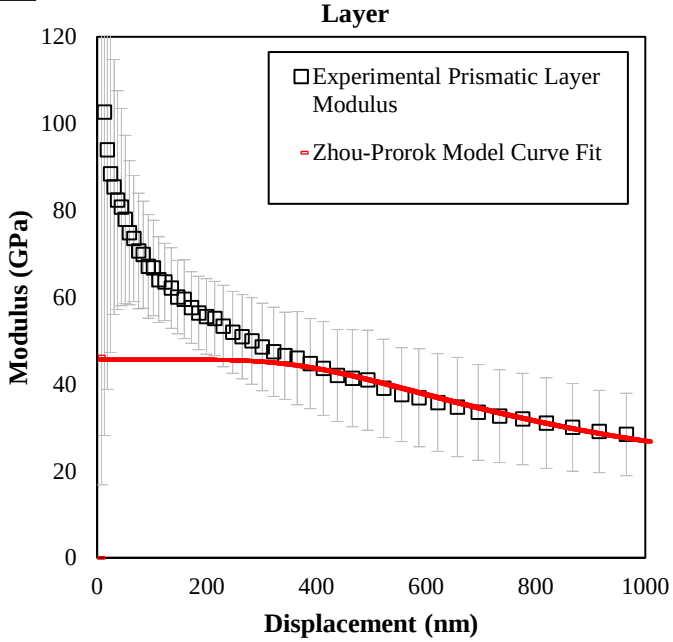

(b) **The Comparison of The Zhou-Prorok Model Fitted Curve and The Tested Modulus of The Organic Layer**

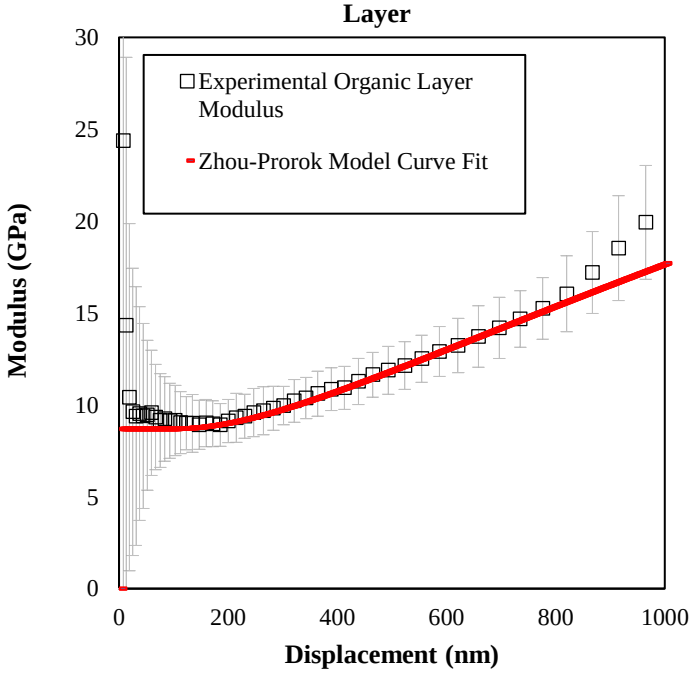

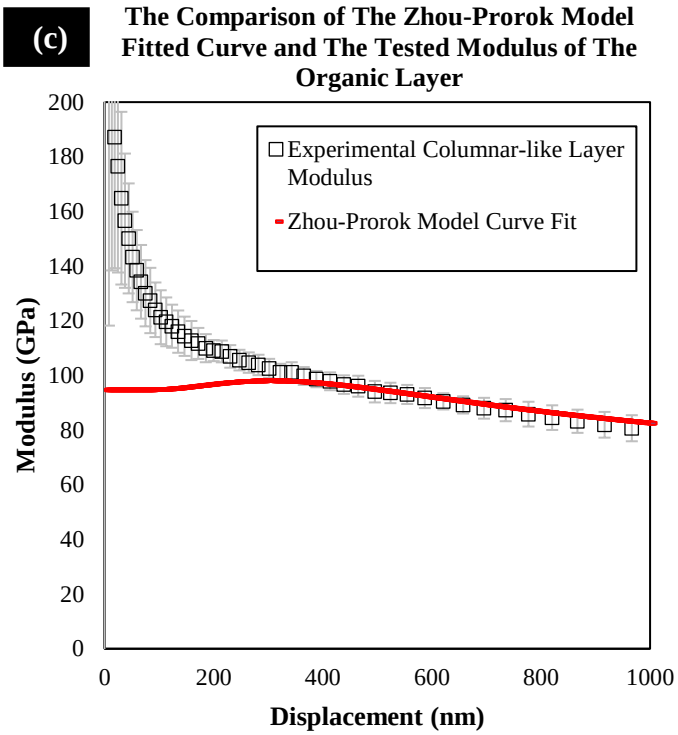

Figure 43*. The Zhou-Prorok model based curve-fitting of the tested modulus of the (a)prismatic, (b)the organic, and (c)the columnar-like layer.*

3.2.1.4 Conclusions

By applying the same calculation stated above and the Zhou-Prorok model on all those three sublayers of the mesolayer, the modulus of the them were determined. The values of the sample being used as the example of the curve-fitting and calculation shown above are listed below in **Table 5**.

The same test, calculation, and curve-fitting were applied on 4 different samples. And, the results are listed in the **Table 6**. Some of the test data are unavailable because the SEM images taken after the nanoindentation test indicates the tested area is not the expected area. Besides, caused by the microstructure, the surface of those sublayer area sometimes cannot be perfectly flat which fails the test.

Layer Name	Calculated Modulus (GPa)	Zhou-Prorok Model Fitted Modulus (GPa)
Prismatic Layer	57.51	54.0
Organic Layer	12.34 (Lowest E)	7.0
Columnar-like Layer	78.88 (Highest E)	85.0

Table 5*. The comparison between the calculated modulus and the Zhou-Prorok model fitted modulus of the prismatic layer, the organic layer, and the columnar-like layer.*

	Calculation by Curve Fitting			**Zhou-Prorok Model Fitting**		
	Organic	Prismatic	Columnar	Organic	Prismatic	Columnar
Sample 1	8.12	-	75.58	7.8	-	74.0
Sample 2	9.58	-	-	8.0	-	
Sample 3	12.34	57.51	78.88	7.0	54.0	85.0
Sample 4	-	52.89	93.86	-	55.0	100.0

Table 6. *The elastic modulus of the three sublayers of the mesolayer collected from different samples.*

It should be noticed in the Zhou-Prorok model fitting (**Figure 43**) that the test results begin to overlap with the calculation curve after surpassing 400nm depth. In the beginning range of 0nm-400nm, the test results and the calculation curve are separated. The Zhou-Prorok model was developed based on the metal thin-film sputtered on the industrially processed ceramic samples, while the mesolayer is a natural multilayer sample. The connection between the thin film and the substrate is even and tidy, while it is random in the mesolayer. Thus, it is reasonable to say that the Zhou-Prorok model fitted values cannot be perfectly matched with the experimental modulus.

In any case, the calcium carbonate is an anisotropic material, and the mesolayer is a natural material. It is hard to obtain two exactly same samples. The mesolayer has a high possibility of exposure on the sample surface, having different orientations in different samples. Thus, the moduli may vary from sample to sample. Even for the organic layer, the modulus is different from sample to sample. The reason for the various moduli of the organic composition might be different from the reason for the calcium carbonate part of the mesolayer. Besides, if the tested layer is too thin, it has the possibility that the test is influenced by more than one substrate which can cause a more complicate problem. Under that situation, the analysis of the stiffness of the tested area might need a more complex calculation. Although the modulus tested from different samples may various among each other and this difference sometimes is quite distinctive, the columnar-like layer always shows the highest modulus among the three sublayers while the organic layer always show the lowest modulus.

What makes the investigation of mesolayer more complicated is the fact that there is an area which shows the contrast of both the very dark organic area and bright calcium carbonate area, which is distinguishable in the backscatter electron SEM image of the mesolayer (**Figure 11**). Currently, no information about this area could be found. But it is possible that the mechanical effect brought on by this area cannot be ignored in the test.

More research could be performed to learn the details of this complex structure. The studies of the mechanical properties of the mesolayer itself are the foundation used in investing the role that the mesolayer plays in the whole nacre structure.

3.2.2 The Nanoindentation Test Applied on The Nacre

Although the mechanical properties of nacre have been studied extensively, more secrets of this complicated structure are still waiting to be explored. In this research, nanoindentation tests were applied on various nacre samples which are collected from different individudals. The nacre samples were obtained from the previously mentioned California red abalone, purchased from the abalone farm.

3.2.2.1 Sample Preparation

Abalone shells were cleaved into approximately $2cm^2$ rectangular pieces with the use of a dermel tool (**Figure 44 (a)**). The top and bottom surfaces were both grinded to have the faces parallel to each other, and both the top and bottom surfaces were also parallel to the boundary of calcite and nacre portions, as much as possible (**Figure 44 (c)**). The top surface, i.e. nacre surface, was finely polished before the test. Then, the samples were mounted on an Aluminum puck and were ready for nanoindentation tests (**Figure 44 (b)**).

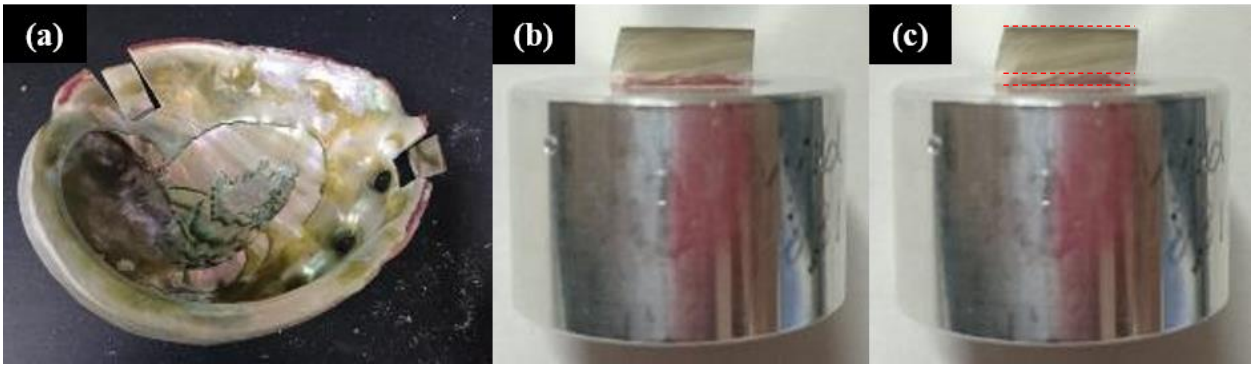

Figure 44*. Sample preparation for nanoindentation tests. (a) Abalone shells were cleaved into small pieces. (b) These small pieces were grinded, polished and fixed on Aluminum pucks and used for nanoindentation tests. The photo was taken from cross-section side of the sample. (c) The top and bottom surface are parallel to the boundary lines as much as possible.*

Nanoindentation tests were applied on the finely polished top surface of these prepared samples. Different types of nacre samples were included in this research and they are listed in **Table 7**.

Samples Used for Nanoindentation Tests			
Farm-raised California red abalone shell		**Wild** California red abalone shell	
Hydrated sample	Dehydrated sample	Hydrated sample	Dehydrated sample

Table 7*. Nacre sample types used in the nanoindentation tests included in this section.*

3.2.2.2 Testing and Results

At the beginning of the mechanical properties study of nacre, nanoindentation tests were applied on the hydrated farm-raised and hydrated wild California red abalone shell samples. Samples were obtained from different individuals and different areas of the abalone shell. The samples included in this experiment are the ones without mesolayer, i.e. no black lines could be observed from the cross-section side of the samples.

In these tests, the test depth was set as 2000nm. 25 test points (5×5 pattern, the distance between every two adjacent points is 100μm) were applied to each sample. The average elastic modulus of these 25 tests points was treated as the final elastic modulus for each sample. The elastic modulus vs. displacement data for both the farm-raised and wild abalone nacre were plotted (**Figure 45**).

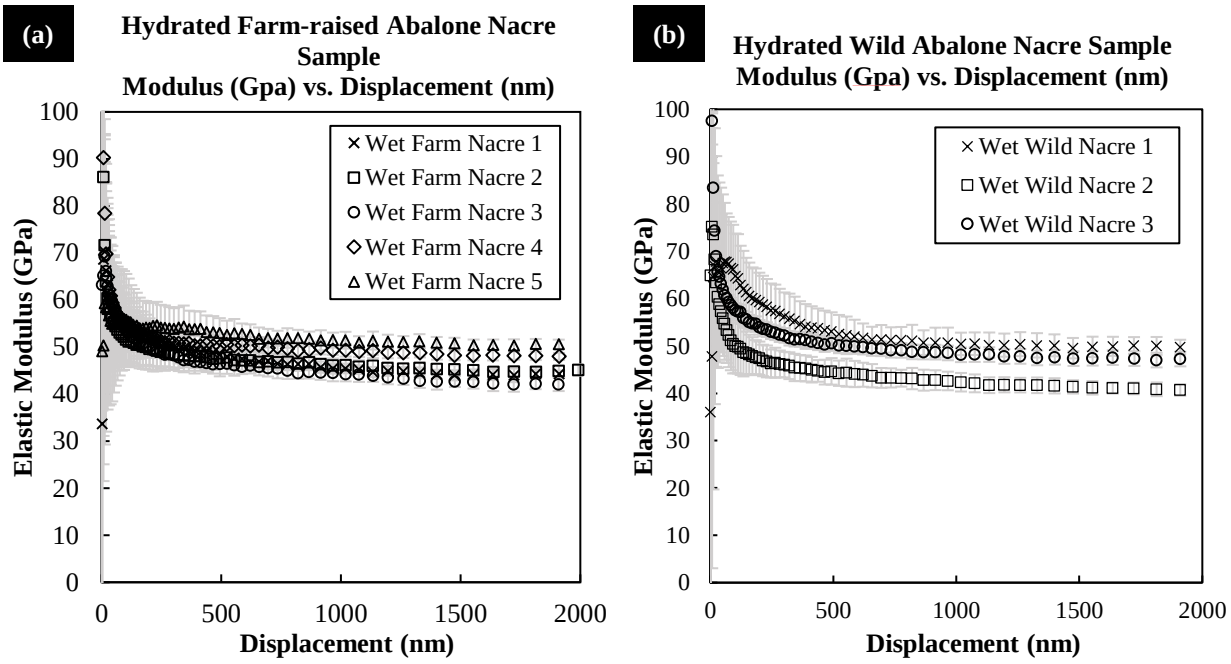

Figure 45*. Elastic modulus of (a) hydrated farm-raised abalone nacre samples and (b) wild abalone nacre samples. Samples were obtained from different individuals. Nanoindentation tests were applied on the top surface of these samples. Some of the values are close to each other while others are not.*

When the tests were applied on the top-side surface, the plots show that the elastic modulus values stayed in the range of 40GPa-55GPa for both the farm-raised abalone and the wild abalone. However, these values fluctuate in this range. As for some samples, the difference is more than 10GPa, which cannot be ignored. This fluctuation also appears among the dehydrated nacre samples. SEM images were taken for the polished nacre surface, in order to find the reason source of this difference. In the SEM images (**Figure 46**), orderly aligned lines are shown. Under further investigation, these lines were determined to be the stacked tablet layers. It can be seen clearly in **Figure 46 (b)**. The reason why the tablet layers can be seen on the polished surface is that the tablets are not perfectly parallel to the polished surface. In fact, the boundary lines of the two shell

parts often appear as waviness rather than perfect straight lines. During the grinding and polishing, the front surface of tablets may not be completely exposed on the top surface. They are more likely to have an inclination angel to the sample surface. Two sketches of the cross-section side of nacre shown in **Figure 47** could assist with showing the reason of the stacked layers lines which are shown on the polished nacre surface.

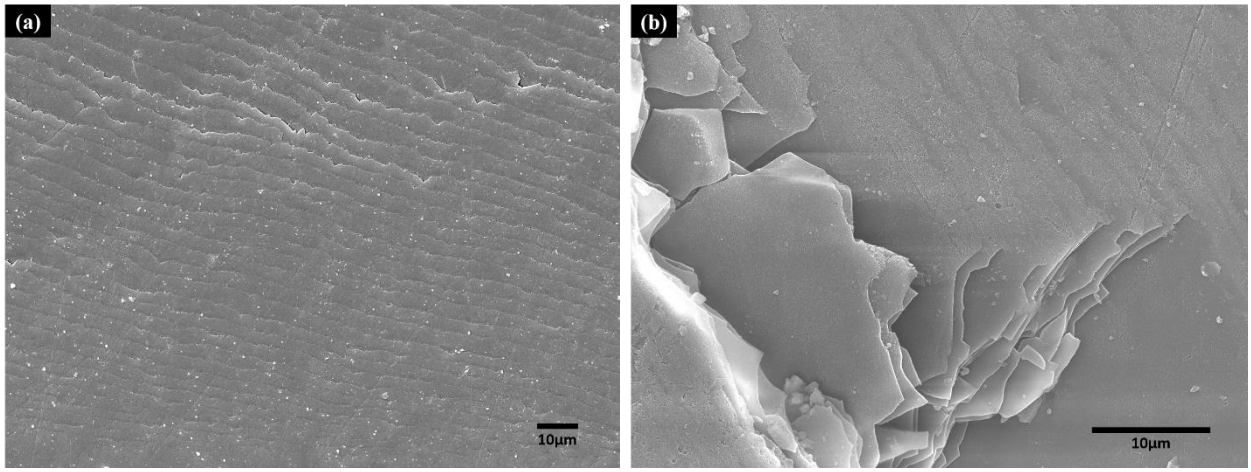

Figure 46*. SEM images were taken for these polished nacre sample surface. Tablets are stacked layer by layer in order. (a) The polished sample surface showing the lines caused by the layer by layer tablets; (b) The lines observed on the sample surface was determined to be caused by the tablets stacking from the mechanically broken nacre sample.*

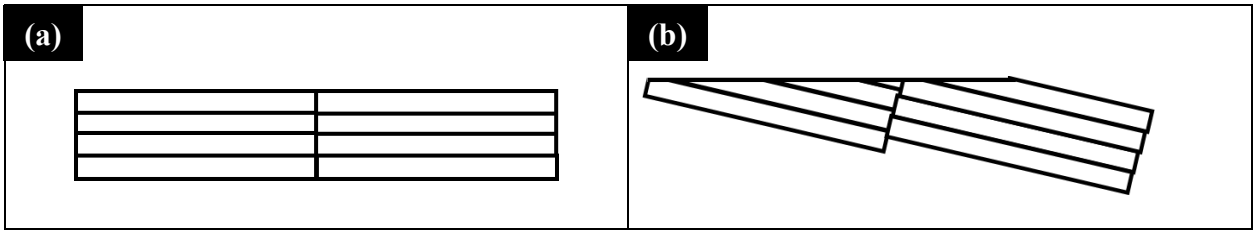

Figure 47*. Two drafts from cross-section side of the polished nacre sample. (a) The expected polished nacre with the tablets front surface perfectly and completely exposed on the top surface*

of the nacre sample. (b) The tablets front surface is not parallel to the polished top surface in practice and causes the stacked layer lines shown on the sample surface.

Different crystal orientations, various tablet inclination angles, different hydrated level, etc all have the ability and possibility to influence the nanoindentation tested modulus. Thus, the differences among these test results are reasonable.

Figure 48 shows the secondary electron SEM image of a 1000nm depth nanoindentation on nacre sample and a 2000nm depth nanoindentation on the (001) plane of an aragonite single crystal. Serious cracks are shown around the nanoindentation on nacre (**Figure 48 (a)**) which indicates that the nacre tablet is still a brittle material. Cracks also appear in the center of the nanoindentation on the nacre. **Figure 48 (b)** is a 2000nm depth nanoindentation on an aragonite single crystal. Even though the nanoindentation depth on aragonite is higher than the one on the nacre sample, there are no serious cracks forming around the nanoindentation like what is shown on the nacre sample surface. The different behaviors observed on the sample surface between the nacre and the aragonite single crystal also supports the idea that the nano-structure of nacre effects the mechanical property of the aragonite. Thus, it is necessary to investigate the behavior beneath the surface. The Focused Ion Beam (FIB) was applied on the indentations on the nacre. Part of the material was milled and the structure under the surface was exposed.

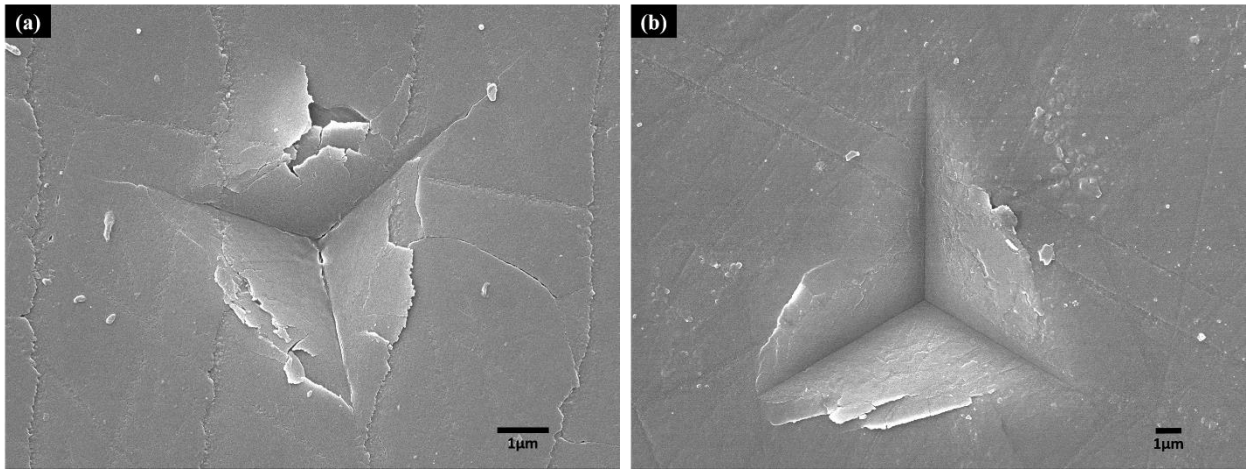

Figure 48*. The nanoindentation on (a) California red abalone nacre (1000nm depth) and (b) a mineral aragonite single crystal (2000nm depth).*

By milling a gap with FIB, the sub-surface tablets could be seen clearly (**Figure 49**). In one of the nanoindentations, the gap was milled perpendicular to the tablets layer lines (**Figure 49 (a)** and **(b)**). The tablets cracks were observed under the surface. These cracks concentrate around the boundary between two tablet layers which can be shown by combining the layer lines on the sample surface. For another nanoindentation, when the FIB was applied in a different direction of the indentation and within the area of one tablet layer, just as shown in **Figure 49 (c)** and **(d)**, cracks were also observed but not as serious as these ones around the boundary of the two tablet layers.

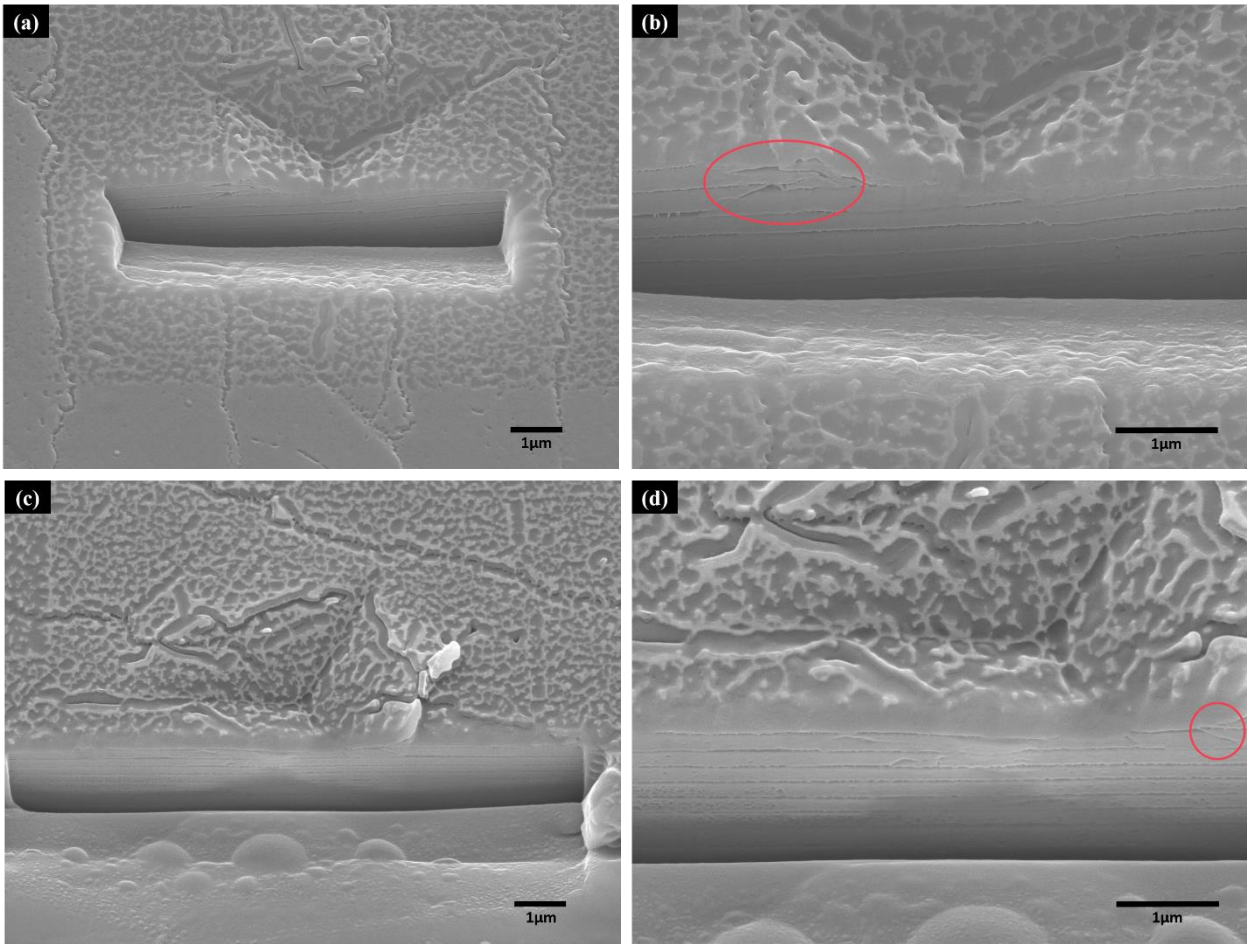

Figure 49*. FIB was applied on nanoindentations on a farm-raised dehydrated nacre sample surface. (a) Full view of one indentation and the gap obtained by FIB is perpendicular to the tablet layer lines; (b) The same indentation as the one shown in figure (a) with some serious cracks being shown; (c) Full view of another nanoindentation. The gap is within the area of one tablet area; (d) The same indentation as the one shown in figure (c) and cracks are seen but not as serious as the one shown in figure (b).*

There were numerical reports on the ability of nacre tablets, which isolates cracking and deformation from each other. Our experiments showed this ability can still hold true even under extreme strain. In **Figure 49**, the cross section from FIB shows the deformed nacre under strain concentration from nanoindentation. This high strain is enough to completely pulverize a few

tablets near the surface where the strain is concentrated. However, the rest of the tablets are free of the deformation. Even under this extreme strain, the strain field is highly isolated from adjacent tablets.

3.2.2.3 Conclusions

The nanoindentation tested moduli varies among different samples. Even on the same sample, the tested modulus is different from area to area and test to test. Before starting the test, the samples were placed in water for the same amount of time. Thus, it is assumed that these samples are equally hydrated.

Based on the observations, even if the samples are collected from the same species of abalone and prepared in the same way, the tablet inclination angle to the sample surface is still varies among samples as the shell is in a dome shape. As the nacre sample is a natural material, it is hard to prepare exactly identical samples. This could be one of the reasons for the variations in the tested moduli. Cracks were observed around the nanoindentations. The formation of these cracks might influence the tested elastic modulus. As it is impossible to have identical cracks for each nanoindentation, these cracks also could be responsible for introducing the differences among the tested moduli.

3.2.3 The Nanoindentation Test Applied on The Nacre with Sputtered Chromium (Cr) Film – The Chen-Prorok Method

As there are cracks which occurred under the surface when nanoindentation tests were applied, these irreversible damages might influence the test results. A special method which could help in avoiding crack formation during the test became necessary. The Chen-Prorok method [70] was implemented in this research to solve the sample damaging problem. In this method, when the

metal thin film is sputtered on to the ceramic material surface and nanoindentation test was implemented, the elastic modulus of the substrate could be calculated with the developed equation (**Equation 7**).

$$\frac{1}{E_t}\frac{1}{(1\ -\ e^{-\nu_s/h'})} \approx \frac{1}{E_f'} + \frac{1}{E_s}(0.5\ -\ \frac{\nu_f}{\nu_s} + \frac{h'}{\nu_s})$$

Equation 7. *E_t – The tested elastic modulus from nano-indenter, E_f' – Metal thin film's elastic modulus, E_s – Substrate's elastic modulus, ν_s – Substrate's Poisson's ratio, ν_f – Metal thin film's Poisson's ratio, h' – The nanoindentation displacement over thin film thickness ratio.*

3.2.3.1 Sample Preparation

Nacre samples were cleaved, grinded, and polished in the same way as in the previous experiments.

Based on the Chen-Prorok method, chromium (Cr) film was sputtered on to the polished nacre surface. Direct current sputtering was used, and the sputtering parameters are listed in **Table 8**. The thickness of Cr film was controlled through manipulating sputtering time. As the height of the sample is different among groups, the film thickness could be different even if the sputter parameters are exactly same. Thus, the film thickness needed to be measured after each sputtering. A piece of silicon wafer was sent into the sputter chamber together with other samples as a reference sample. The silicon wafer was placed at a similar height with the samples. The thickness of the Cr film on the silicon wafer could be treated as equal to the film thickness on the nacre samples. Finally, the silicon wafer could be broken into smaller pieces, and the final thickness of the Cr film is measured from the cross-section side of the silicon wafer piece by using SEM. Thickness is measured at different locations and the final thin-film thickness was determined by

the average value of these measurements. The SEM images were taken to show morphology of the Cr film from both top side and cross-section side (**Figure 50**).

Target Material	Cr
Pre-sputtering Power (W)	200
Pre-sputtering Time (s)	120
Sputtering Power (W)	200
Sputtering Time (s)	1000
Gas flow rate (sccm)	25
Deposition Temperature (ºC)	RT
Ignition Pressure (mTorr)	80
SEM Determined Average Film Thickness (nm)	459.5

Table 8*. The parameters used for sputtering the Cr film on the top of nacre sample. The sputter time may change due to different film thickness being required.*

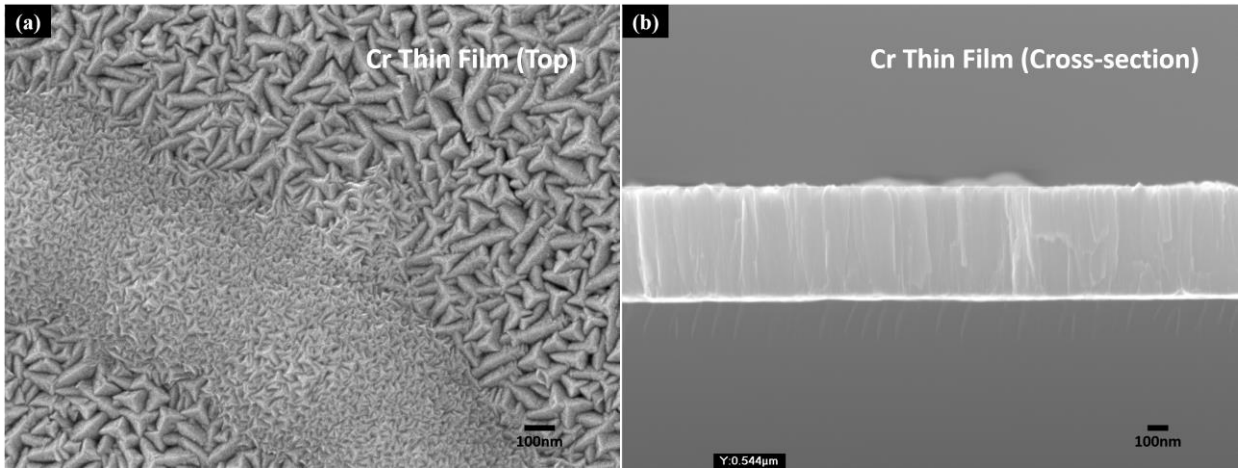

Figure 50. *Cr thin film was sputtered on the nacre samples and a reference Si slice. SEM images were taken from both the top side and cross-section side. (a) The SEM image taken from the top*

side of the Cr film on the nacre; (b)The SEM image taken from the cross-section side of the Cr film on the Si slice.

Samples used for these experiments so far were dehydrated farm-raised abalone nacre as they have almost pure nacre structure without too many interruptions in the structure that might act as an obstacle in experiments. Also, due to the high vacuum environment during the sputtering, the final obtained samples are assumed as completely dehydrated samples. Nanoindentation tests were applied on the Cr film on both the top and cross-section side surfaces of the sample (**Figure 51**), and they were named as "Cross-section side" sample and "Top side" sample respectively. These samples were finally mounted on to the aluminum pucks and were ready for nanoindentation test.

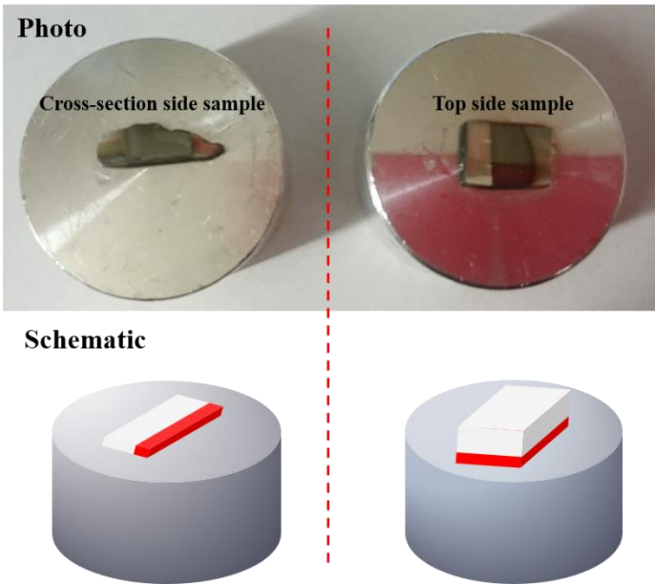

Figure 51*. Two types of dehydrated farm-raised abalone nacre samples have Cr sputtered on and used for nanoindentation tests. The left sample has Cr film on nacre cross-section surface and is called "Cross-section side" sample. The right sample has Cr film on nacre top surface and is called "Top side" sample.*

Nanoindentations in a 5 × 5 pattern were applied to the sample for one test and the result was calculated by the test software based on the valid data in these 25 nanoindentations. The nanoindentation depth depends on the thickness of the Cr film.

3.2.3.2 Nanoindentation with The Same Indentation Depth Applied on Nacre Samples with Various Cr Film Thickness on The Top

831nm depth indentations were applied on "Top-side" sample with 831nm Cr film on top firstly to see how the Cr film and nacre behave and to determine if this method was valid for nacre. SEM images were then taken from the top side (**Figure 52**). The images show that cracks form along the indentation edges and around indentations. In fact, Cr film is a relatively ductile material and rarely shows cracking during the nanoindentation tests.

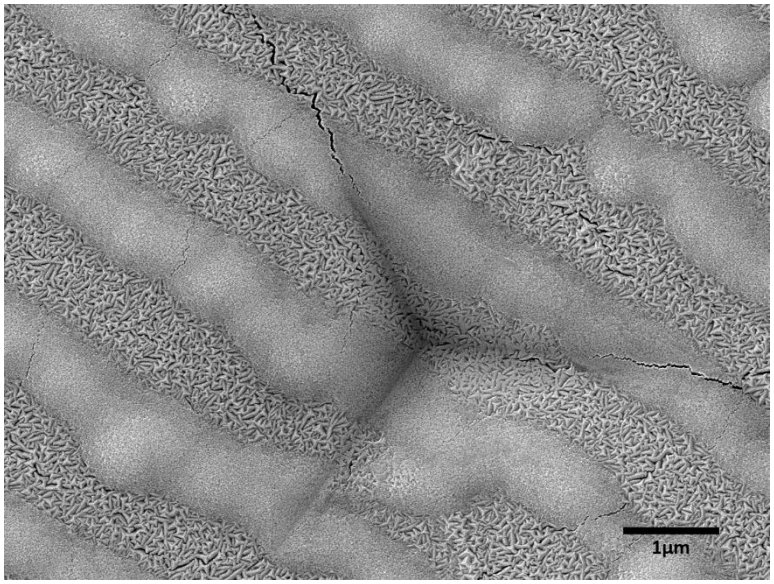

Figure 52*. SEM images are taken for the 831nm nanoindentations applied on 831nm Cr film on a "Top-side" nacre sample. Cracks are shown forming along the edges and around these nanoindentations. The nanoindentations were checked one by one, and all of them show the similar morphology and cracks.*

Then, FIB was applied on some of these indentations and the SEM images were taken of the structure underneath (**Figure 53**) to show the behavior of the material. There were no cracks found in these aragonite tablets. Even when a gap was milled perpendicular to the tablets' line (**Figure 53 (b)**), no cracks could be observed around the boundary between two layers of tablets. However, the SEM images indicate that the bottom of the Cr film is torn.

The sample shown in **Figure 53** was applied 831nm depth nanoindentation test while the one shown in **Figure 49** is 1000nm. The difference between these two depth values is not too much, thus the tablets behavior should be comparable. Chen-Prorok method was valid in testing abalone nacre as it was helpful in eliminating cracks on the tablets during the nanoindentation test.

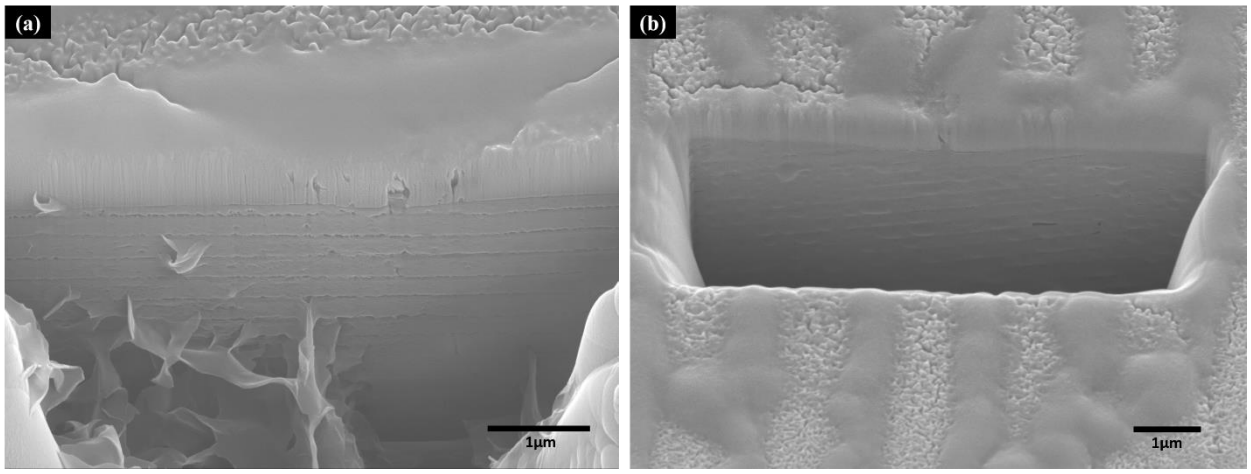

Figure 53*. FIB was applied on two randomly selected nanoindentations shown in (a) and (b) respectively. The indentation depth is the same as the film thickness 831nm. No cracking of tablets could be observed.*

Besides the 831nm Cr film sample, these "indentation depth equivalent to Cr film thickness" experiments were then applied to another two samples. One with an 870nm Cr film and the other a 459nm Cr film. Based on the Chen-Prorok method, data obtained from Nano-indenter does not

represent the elastic modulus of the substrate, i.e. in this experiment, the nacre. The data was calculated using **Equation 7**. After the calculation, the elastic modulus of nacre was plotted against ratio between displacement and metal film thickness to show the elastic modulus of the nacre samples. The results for the 831nm, 870nm, and 459nm Cr film samples were placed in one plot for comparison (**Figure 54**). In **Figure 54**, the three curves all trend in a similar fashion, as to be expected. They also show reasonable elastic moduli values between 40GPa to 60GPa, which is similar with the results when nanoindentation tests were applied on nacre from the top side without Cr film.

With the metal film, the serious cracks were eliminated and the number of valid test points out of the set 25 tested points increases. The results can be considered more reliable. It should be noted that the results plotted in **Figure 54** are for three different samples, and the Cr film thickness for them are also different. Thus, it is difficult to determine the reason causing the different moduli shown in **Figure 54**. Either the film thickness or the sample itself could be the one leading to the differences. In later experiments, the Cr film thickness of all the samples are kept at a relatively constant value to eliminate any variations caused by the thin film thickness.

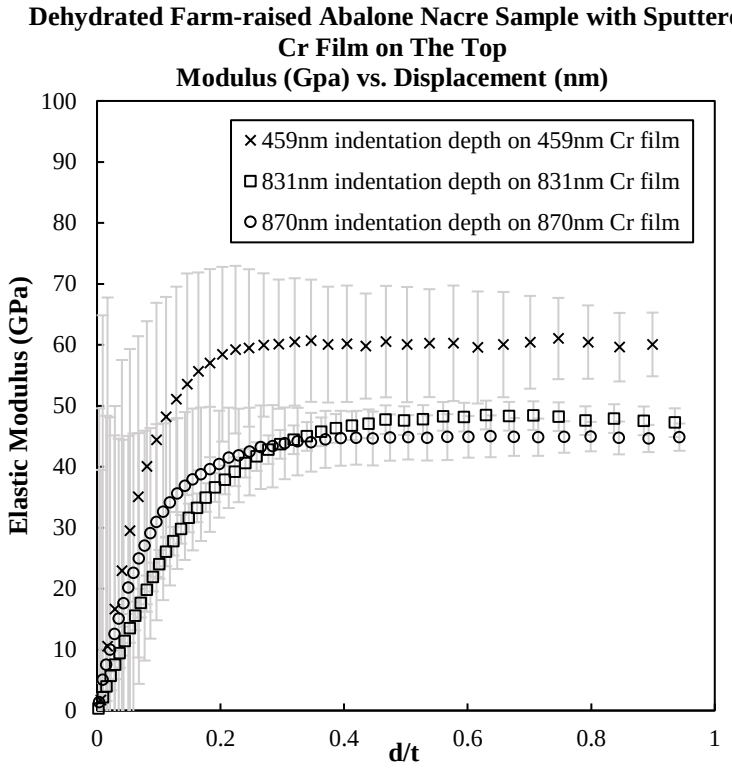

Figure 54*. The Chen-Prorok method based calculated elastic moduli of abalone nacre is plotted against the displacement/film thickness ratio. Three different samples are compared. The Cr film thickness on the top of the three samples is different from each other.*

3.2.3.3 Different Nanoindentation Depth on The Same Sample with 831nm Cr Film

Since the cracks along the edges and around the center of nanoindentations were observed when the indentation depth was equivalent to the Cr film thickness, different nanoindentation depths were then applied on samples to see how the Cr film will behave. “Top-side” sample, which was sputtered with 831nm Cr film, had a nanoindentation depth of 300nm, 500nm and 750nm applied to it. SEM images were taken for these different depths and are depicted in **Figure 55**.

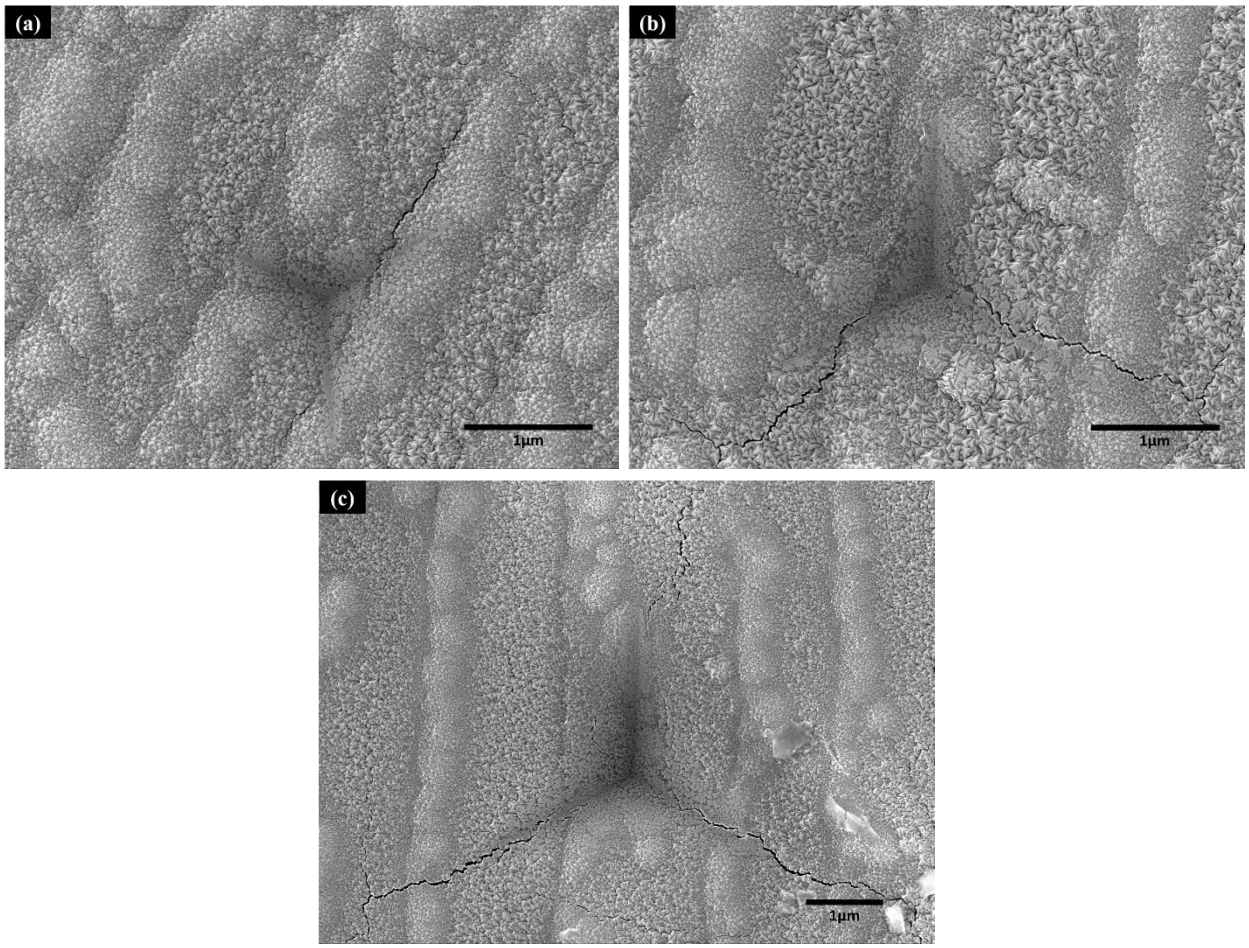

Figure 55*. Nanoindentations with the depth of (a) 300nm (b) 500nm (c) 750nm were applied on a "top side" nacre sample sputtered with 831nm Cr film. These nanoindentations were made in a small area, so the tablets could be treated as showing the same inclination angle*

It can be seen that the amount of crack formation varies with each indentation depth. In the 300nm nanoindentation test, almost no cracks appear around the indentation. In the 500nm test, cracks started to occur along the edges of the indentation. In the 750nm test, the cracks became more serious. The data obtained from the nanoindenter for these three tests was plotted together in **Figure 56**. These three curves are relatively well matched with each other. This is reasonable because these three tests were applied on the same sample within a very small area which could

be assumed to have tablets in the same orientation. For the same reason, the cracks which formed around these three nanoindentation tests are assumed to be comparable.

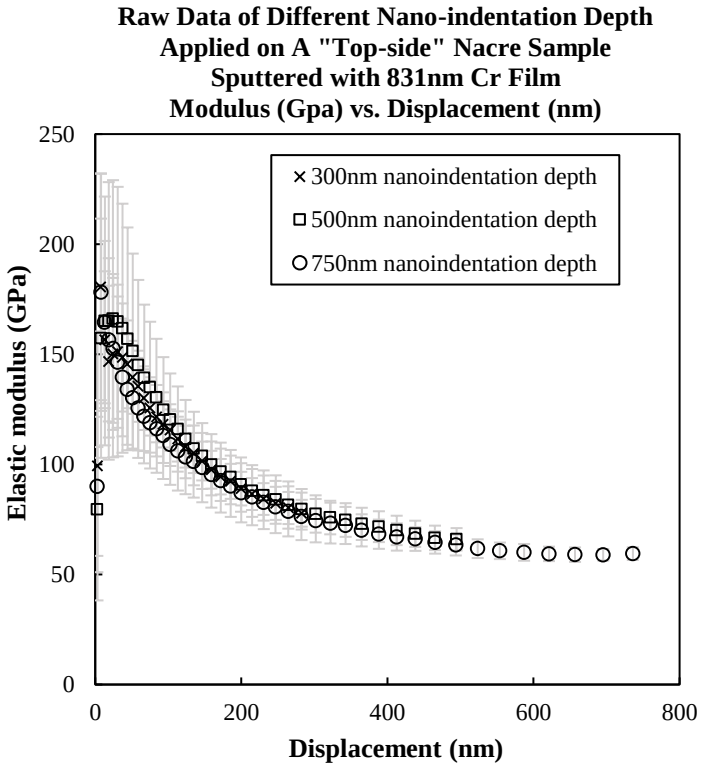

Figure 56*. The plots of the data obtained from the nanoindenter without Chen-Prorok method calculation for different nanoindentation depth (300nm, 500nm, 750nm) trend very similarly.*

In the Chen-Prorok method, to calculate the data presented by the nanoindenter, the nanoindentation depth must be over half that of the thin film thickness. Thus, the 300nm nanoindentation test data could not be calculated. The 500nm and 700nm depth test results were calculated using **Equation 7** and plotted in **Figure 57**. After the calculation, the curves were again well matched throughout. The calculated results for the 500nm and 750nm depth nanoindentation tests were 48.805GPa and 47.606GPa, respectively. These results represent the elastic modulus of the nacre sample.

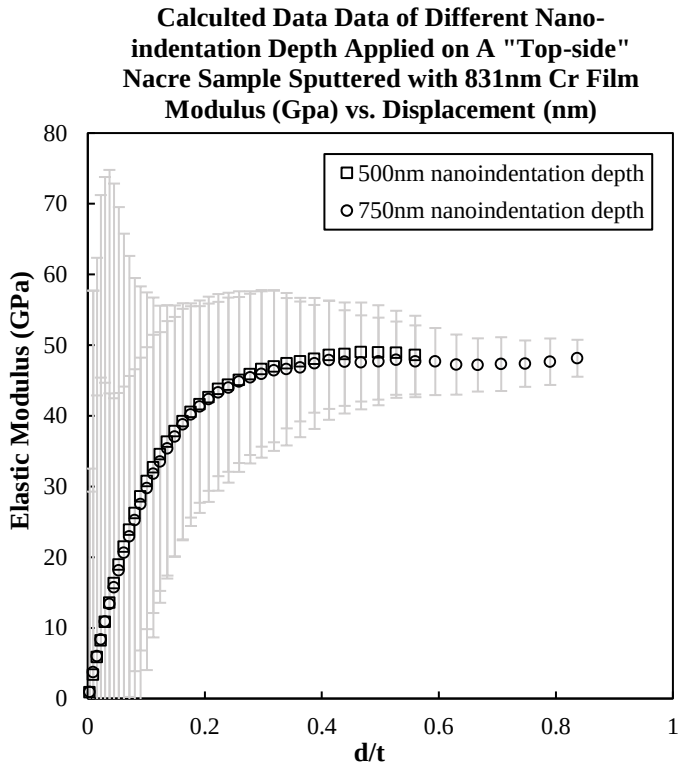

Figure 57*. 500nm and 750nm nanoindentation test results were calculated and plotted. The two curves match with each other all the way.*

3.2.3.4 Conclusions

By comparing the nanoindentation tested modulus data and the SEM images taken for these samples, it was determined that the Chen-Prorok method is a valid method for investigating the elastic property of the abalone nacre.

The nacre is a natural material and it is difficult to obtain two identical samples. Thus, there are always several variables which effects the moduli, and it can't be fully determined the effect that the Cr film thickness has. As the influence brought by Cr film thickness is still uncertain, only the results collected from the samples with similar Cr film thickness could be used for comparison. At the same time, the results for the tests with different nanoindentation depth within the same small

area match with each other very well. Thus, the influence brought by other factors will need to be investigated, and the experiments could be done within a small area on the same sample.

3.2.4 The Nanoindentation Tested Anisotropic Modulus of Nacre

Another unique property of nacre is the high anisotropy of its mechanical properties. This is believed to be caused by the special architecture. Based on the results concluded from the previous experiments stated above, the Chen-Prorok method was used for studying the anisotropic elastic property of nacre. The investigation of the anisotropic mechanical property, and its relationship to the architecture could contribute to the development and designation of composition materials.

It has been introduced that through the sample preparation methods, the nacre tablets normally show an inclination angle to the surface. This could be determined by the counting the lines which are approximately parallel to each other on the sample surface. These lines are called the "tablet lines" here. Although the thicknesses of these tablets were not constant, the values produced were still within a reasonable range. Based on several randomly selected samples from different individual abalone being measured a hundred times, an average tablet thickness for the nacre included in this research was determined to be 368nm. As the tablet line distance d could be measured, the tablet inclination angle could be calculated by a trigonometric function based on the geometry (**Figure 58**). This is expressed as such using **Equation 8**.

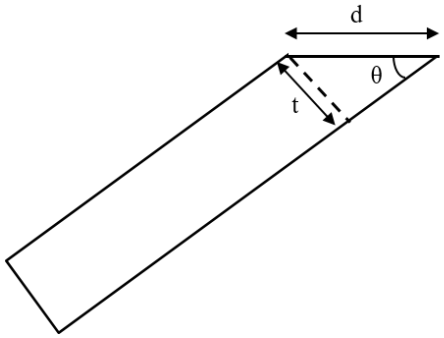

Figure 58*. The schematic of an aragonite tablet. The relation among tablets thickness (t), the distance between two tablets layer lines (d), and the inclination angle in one tablet could be described based on the trigonometric function.*

$$\theta = arcsin\frac{t}{d}$$

Equation 8*.* θ *= The tablet inclination angle,* t *= The average tablet thickness,* d *= The adjacent tablet line distance.*

3.2.4.1 Sample Preparation

Nacre samples included in this part were prepared in the similar way as before: they were carefully grinded, polished, and finally sputtered with Cr film. The sputtering parameters were set as te same as these shown in **Table 6**. Again, during the sputtering, the sample surface and the silicon wafer surface, which acts as a reference sample, were kept at the same height to make sure all these samples were sputtered with Cr film of the same thickness. The tablet lines of the nacre surface could still be distinguished easily from the surface even if the sample was sputtered with the metal film (**Figure 59**).

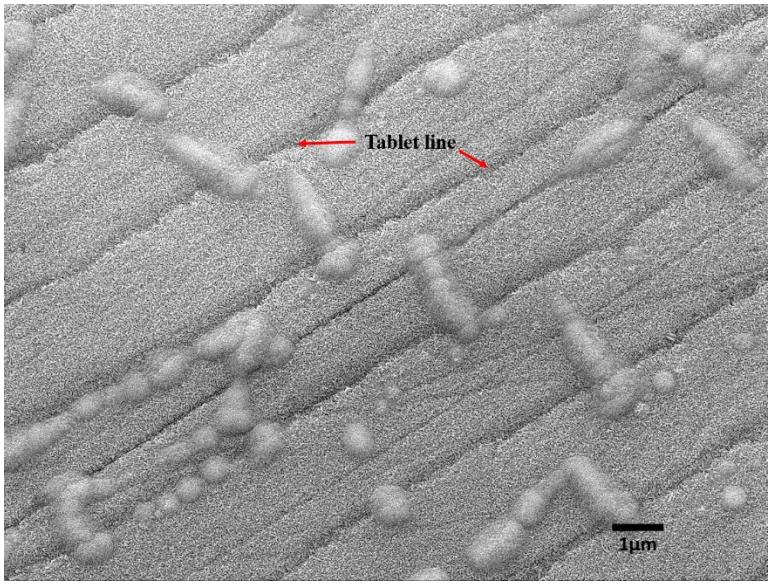

Figure 59*. The polished nacre surface was sputtered with Cr film. The tablet lines could be distinguished from the surface.*

3.2.4.2 Comparison of The Same Nanoindentation Depth on Different Side of Nacre

Compared to the single crystal aragonite, the nacre has a significant change in the anisotropy of the mechanical properties due to its special architecture. It was concluded above that the nanoindentation depth does not affect the test results. Thus, on the same sample and within a quite limited area, applying a series of nanoindentations with gradually varying depth can be helpful in showing the nacre's behavior during the nanoindentation up to the highest depths in this series. This can be treated as equivalent to the *in-situ* observation of a nanoindentation process. To avoid the potential for thickness of the Cr film causing cracks, samples included in the experiments of this part were sputtered with thinner films than before at 459nm. Both the top side and cross-section samples were tested with a series on nanoindentation depths: 300nm, 459nm, and 800nm. SEM images were taken for these nanoindentations with different depth after the tests and they are shown in **Figure 60**.

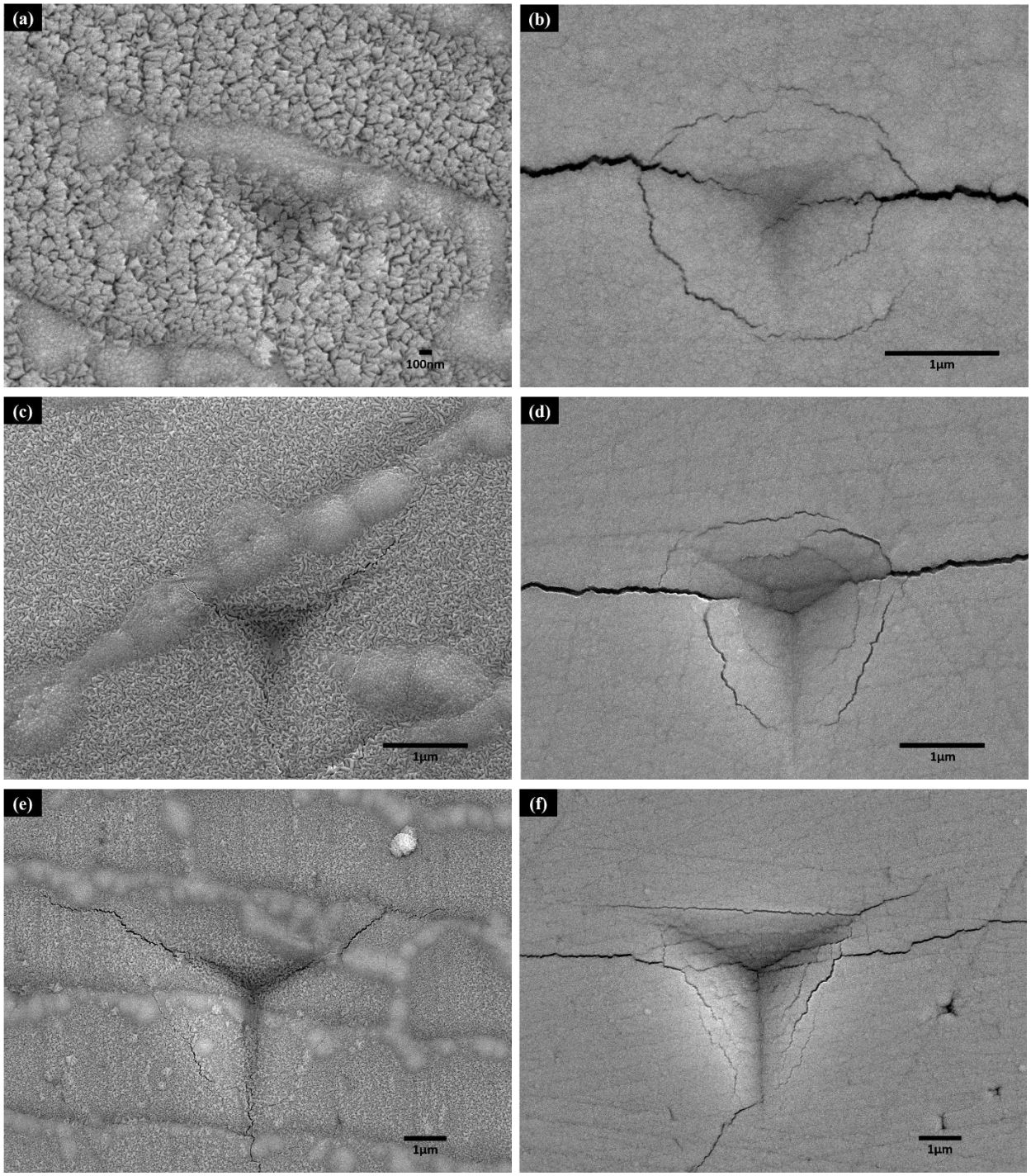

Figure 60*. Same nanoindentation depth tests applied on two types of samples with 459nm Cr film. (a)(c)(e) "Top-side" sample, (b)(d)(f) "Cross-section-side" sample. (a)(b) 300nm depth; (c)(d)459nm depth; (e)(f) 800nm depth.*

On the Cross-section samples, the cracks become more and more prominent as the indention depth increases. At 300nm nanoindentation depth, there appear to be no cracks around the nanoindentation (**Figure 60 (a)**) while some significant cracks begin to appear around every nanoindentation on the sross-section samples (**Figure 60 (b), (d),** and **(f)**). Such distinctive differences in the behavior of the Cr film around the nanoindentation on the top side and cross-section side of nacre sample are a clear indication of the anisotropic mechanical property. Differenet deformation mechanisms can be expected when the force is applied on the nacre top side and cross-section side. The uncalculated raw data of these tests were plotted and shown in **Figure 61**.

Again, the plots show that the tests with different nanoindentation depth on the same sample match well with each other. The tests applied on the top side sample show a better match than the ones applied to the cross-section sample.

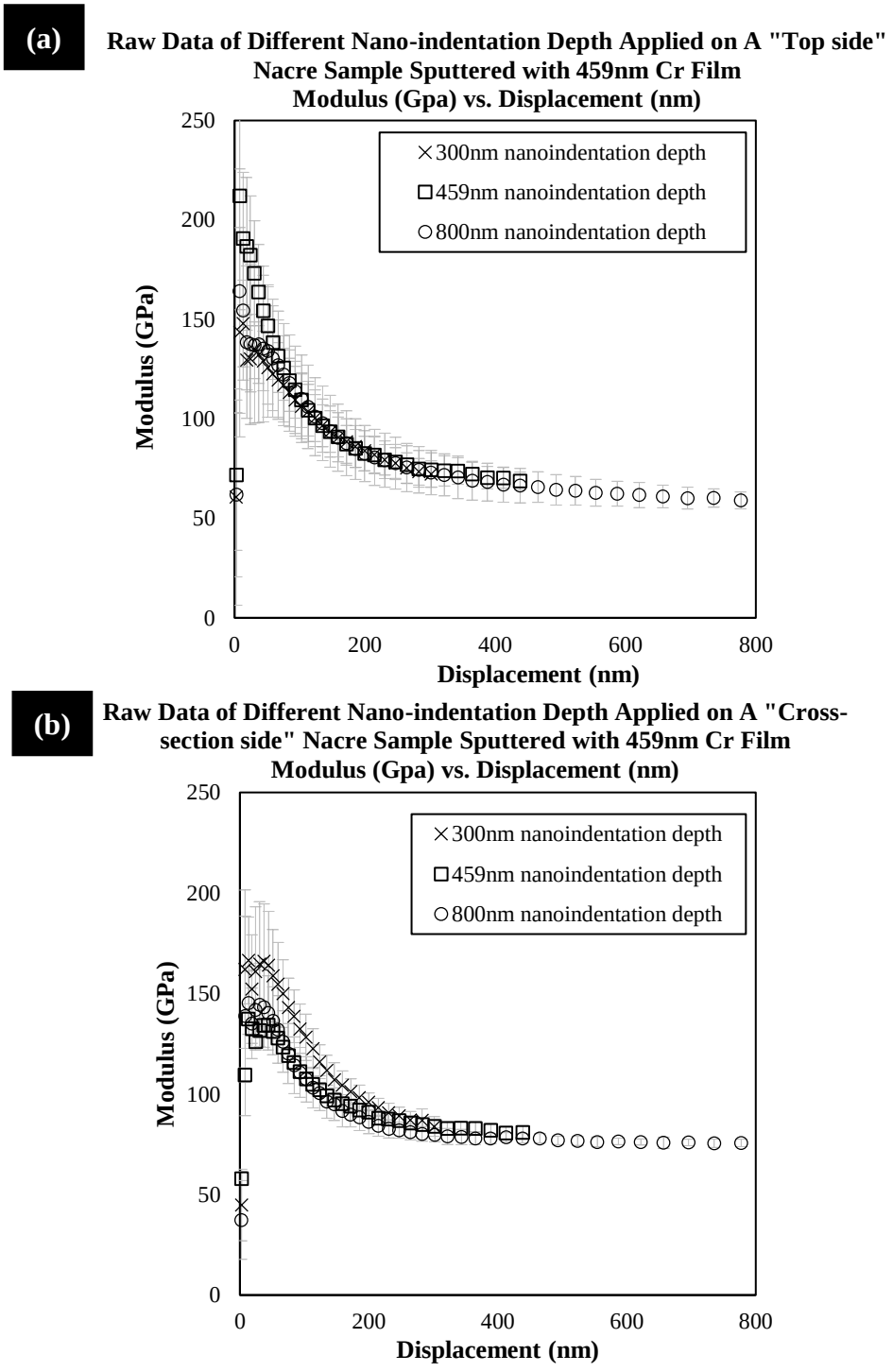

Figure 61*. The nanoindentation tests with 300nm, 459nm, and 800nm depths applied on a (a) top side sample, and (b) cross-section side sample. Both these samples are sputtered with 459nm Cr film.*

These test results were calculated through the Chen-Prorok method, and the calculated moduli of the tests on the top side and cross-section side samples with 300nm, 459nm, and 800nm nanoindentation depth are listed in **Table 9**. The calculated modulus data were plotted together for comparison (**Figure 62**). In the Chen-Prorok method, the collected data of the "nanoindentation depth/film thickness" (d/t) ratio over 0.5 is vaild for determining the modulus of the sample. Thus, it could be concluded from the plot shown in **Figure 62** that, for the nacre, the nanoindentation tested moduli on the cross-section side was always higher than these of the top side sample. This result agrees with the general test results during the whole research that the modulus tested by nanoindentation test from the transverse direction, i.e. on "Cross-section-side" sample, is always higher than that from the lateral direction, i.e. on the "Top-side" sample (**Figure 63**). The elastic modulus tested from the cross-section side is always around 15GPa higher than the top side.

Nanoindentation Depth on The Sample with 459nm Cr Film	Top Side Sample Modulus (GPa)	Cross-section Side Sample (GPa)
300nm Nanoindentation Depth	54.64 ± 9.9945	67.43 ± 5.9572
459nm Nanoindentation Depth	60.17 ± 8.5084	73.17 ± 4.9095
800nm Nanoindentation Depth	53.39 ± 9.3507	72.14 ± 2.9477

Table 9*. The calculated modulus based on the Chen-Prorok method of the top side and cross-section side sample with 459nm Cr film on the sample surface. 300nm, 459nm, and 800nm nanoindentation depth were applied on these two types of samples.*

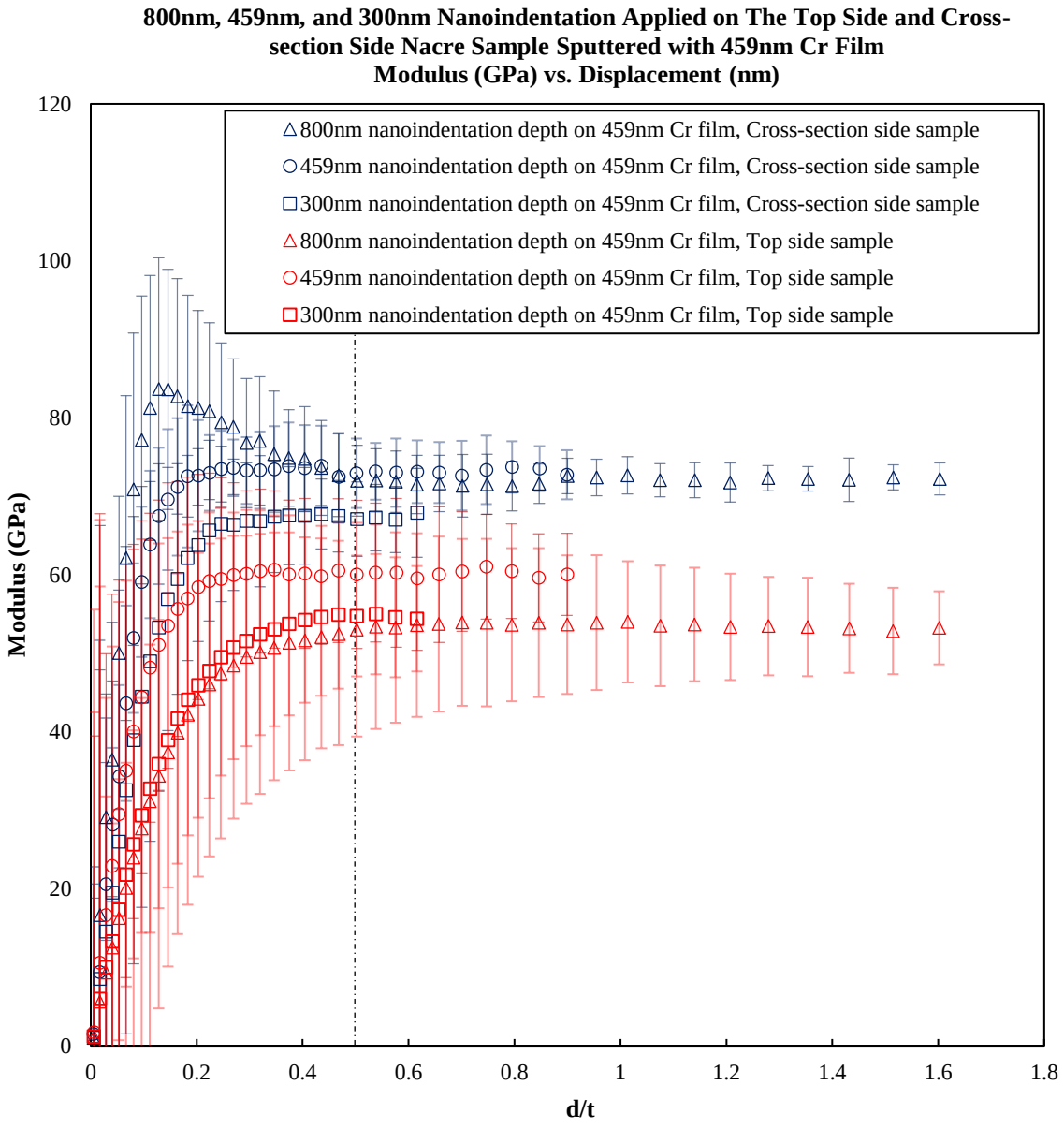

Figure 62. *800nm, 459nm, and 300nm nanoindentation test results on both the top side nacre sample and the cross-section side nacre sample which was sputtered with 459nm Cr film.*

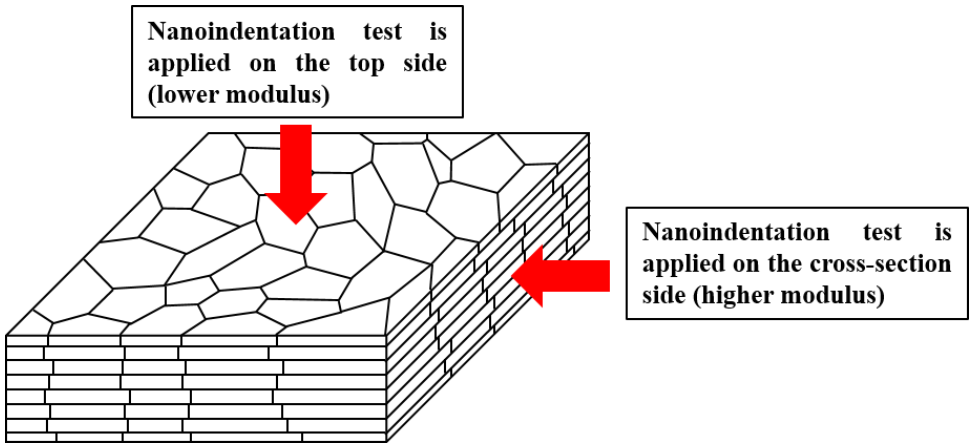

Figure 63*. Schematic of the nanoindentation test applied on the top side and cross-section side of nacre sample.*

FIB was also applied to the Cross-section sample and the SEM images are shown in **Figure 64**. The crack-like behavior was observed on one of the substrate's sub-surface structure (**Figure 64 (b)**, red circled area) which is possibly caused by the compression of the material during the nanoindentation test. More detailes will be discussed in the later part of this dissertation.

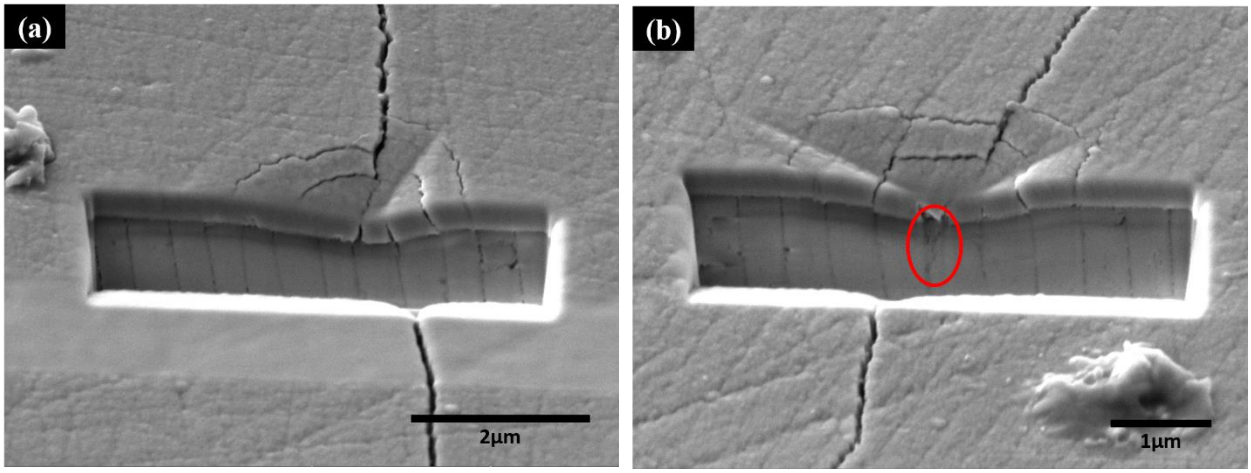

Figure 64*. FIB was applied on the 459nm nanoindentation on the Cross-section-side sample with 459nm thickness Cr film. The two randomly selected nanoindentations are shown in (a) and (b).*

During the process of milling part material of the nacre sample by using FIB, different structure behavior could be observed as different amount material is milled. An example could be helpful to explain this further. **Figure 65 (a)** and **(b)** show the same nanoindentation which was milled off different amount of material. The sample was milled off for some the material and the SEM image is shown in **Figure 65 (a)**. Then, more material was milled off and SEM images were taken again (**Figure 65 (b)**). It should be noticed that what is shown in the red circled area is different. To obtain more information for this completely natural material, it had better to increase the steps of milling and decrease the amount of milled off material in each step. SEM images should be taken after each step. However, as we do not have an easy access to the FIB and the material is an insulator, some more ideas are still needed to make this come true.

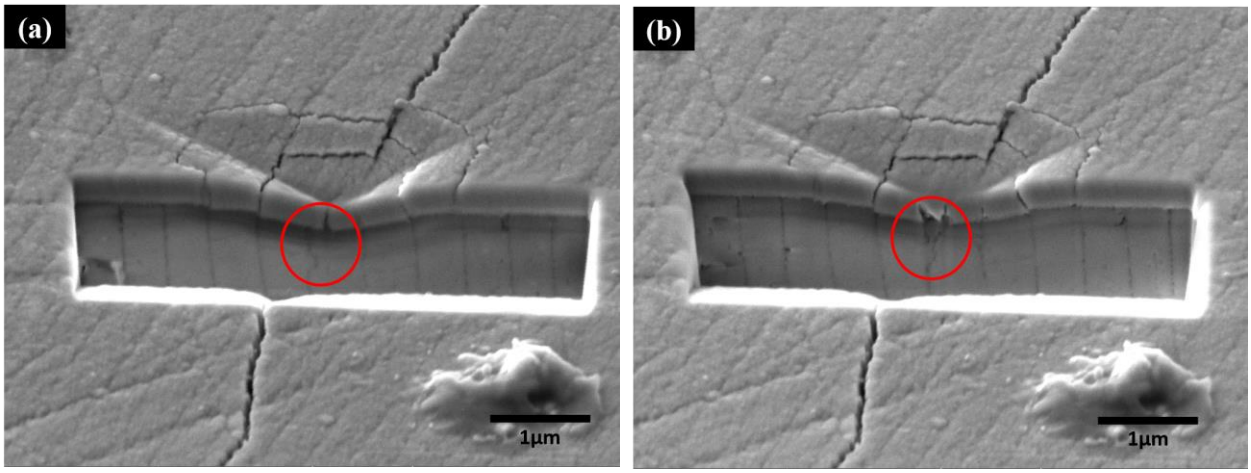

Figure 65. *Different steps during the process of milling part of the material of the same nanoindentation. The sample shown in (b) was milled more material than what is shown in (a).*

3.2.4.3 Various Orientation Nacre Samples Sputtered Cr Film Are Tested

Since the nacre has shown such a high anisotropic modulus, the transition of the modulus between these two directions was investigated to determine the behavior of this material when force is applied to it from various directions and how the modulus is affected.

Randomly shaped pieces of nacre samples were mounted in a resin through a cold mounting process. The nacre samples were placed in the resin randomly to collect various tablet inclination angle data. The height of the resin was controlled and kept to less than 1cm to make sure the samples fit the sputter chamber. When the resin was completely solidified, samples were approriately grinded and polished to insure the nacre was exposed on the surface (**Figure 66**). These samples mounted in the resin were grinded into approximately the same height to guarentee they were sputtered with almost the same thickness Cr film. The sputter process and parameters were the same as before. As it was concluded that the influence brought by the Cr film thickness is still uncertain, the data included in this part is based on the samples sputtered with exactly same parameters and the Cr film thickness on these samples were similar to each other. The film thickness was around 500nm. With the similar Cr film thickness, the tested modulus could be assumed to not be affected by the film thickness.

Figure 66*. Nacre samples were mounted in a resin. They were grinded into the approximately same height and polished to have a flat and smooth surface.*

The nanoindentation tests were then applied to these samples. After that, SEM images were taken for these nanoindentations to show the Cr film behavior and measure the tablets' line distance. With the tablets' line distance, the tablet inclination angle was determined by the calculation. A series of SEM images for samples with different inclination angles, which is shown by different tablet line distance, can be seen in **Figure 67**, showing how the inclination angle changes with the tablets' line distance. The corresponding moduli are shown alongside the SEM images. From **Figure 67 (a-f)**, the tablets' line distance can be seen decreasing, which means the tablet inclination angle continues increasing. The inclination angle change can be seen as a factor for the increase in crack formation around the nanoindentation sites, seen in **Figure 67 (a-f)**.

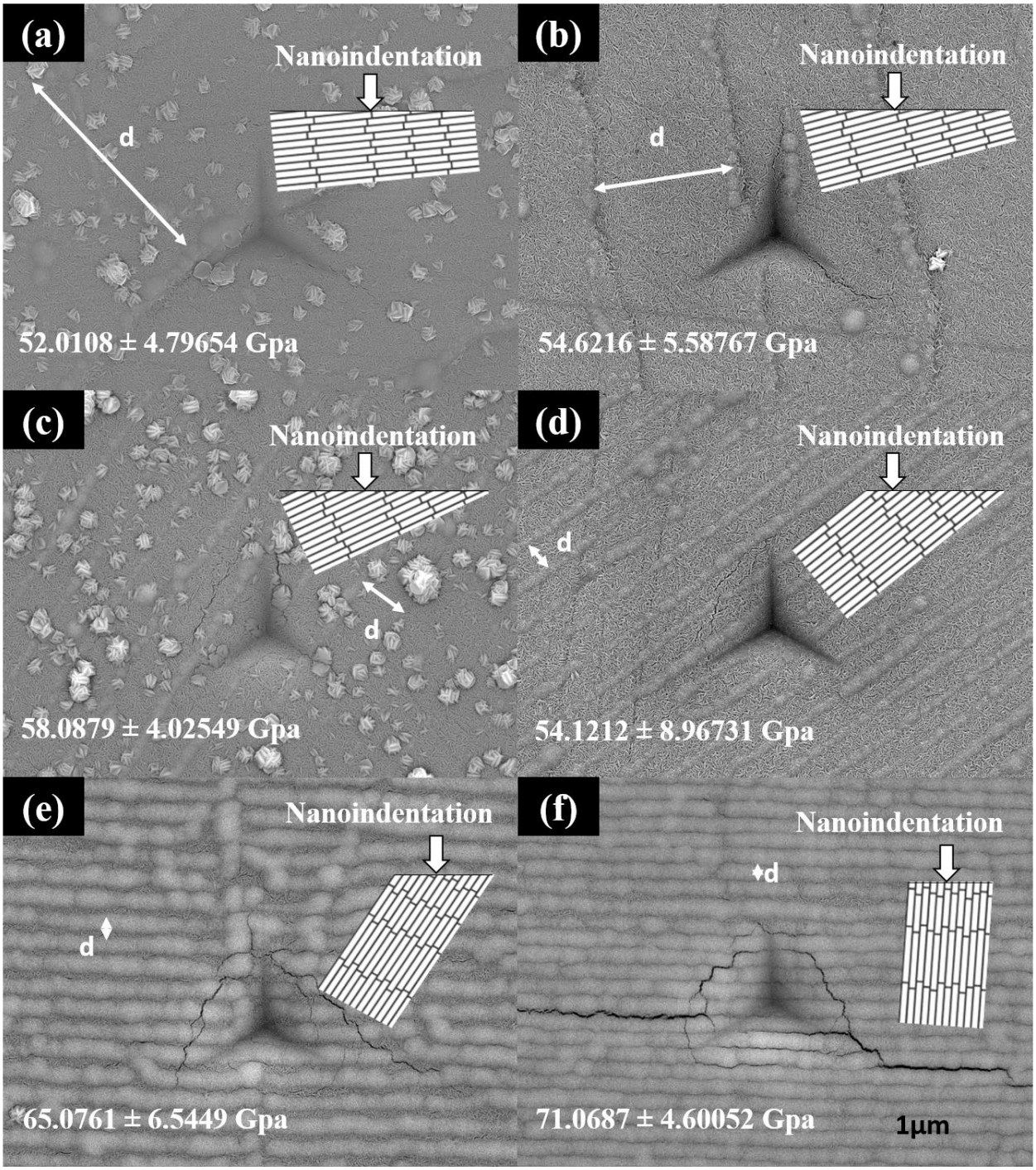

Figure 67*. SEM images of the nacre samples with different inclination angle which is shown by the different tablets' line distance. The corresponding elastic moduli are shown along with the SEM images.*

The test results were collected from various samples and calculated based on the Chen-Prorok method. The calculated results of all the samples were plotted together in a Modulus vs Inclination Angle plot to show the anisotropic modulus of nacre (**Figure 68**). Based on the plot, a distinct and sudden modulus increase occurs around the 45º inclination angle. It is possible that the dominating deformation mechanism has a sudden transition when the inclination angle reaches a specific value. The elastic modulus data was also plotted in a polar coordinate system to show the symetrical architecture of nacre (**Figure 69**). This data was curve-fitted using the least square method and the fitted curve was plotted together with the data points in the polar coordinate to show the symetrical architecture more clearly.

Besides the tablet inclination angle, the rotation angle between the tablet line and the nanoindenter tip is also a concern. Some of these samples were tested within the same area for several iterations with various rotation, which are represented by the multiple color points in the plot (**Figure 68**). The various rotation angles represent the different alignments between the tablets' line and the edge of the Berkovich tip. When the sample was rotated under the tip, the alignment repeats every 60º. And, in the 60º range, if it is considered from 0º to 60º, the alignment has a mirror plane symmetry at 30º. It has been concluded in the previous section that the tests applied in the same small area are expected to have similar results. Thus, the various modulus values tested within a small area on the same sample may possibly be caused by the different alignment between the tablets' line and the nanoindenter tip edge.

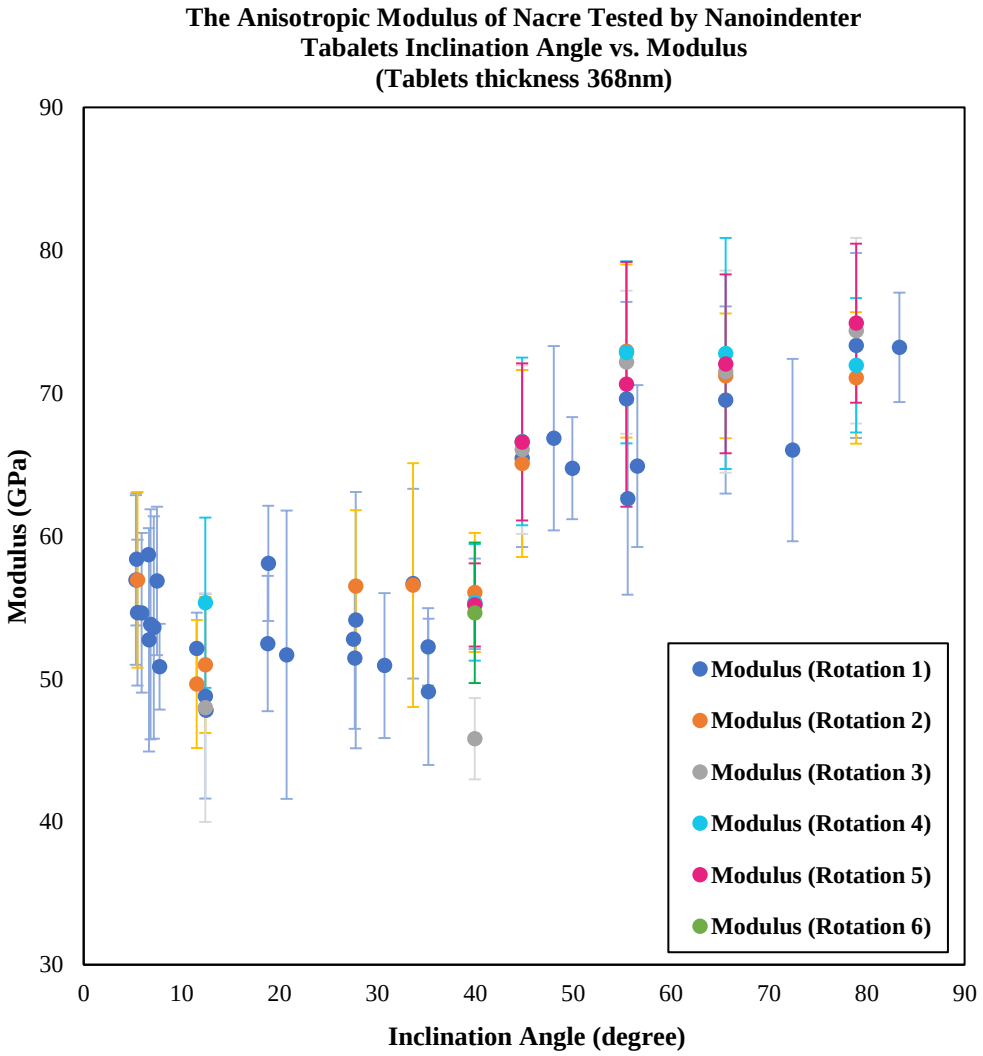

Figure 68*. The collected modulus of various nacre samples was plotted against the aragonite tablet inclination angle from 0º to 90º. The multiple color points represent the several iterations of the nanoindentation tests applied on the same sample within the same area with a different rotation angle.*

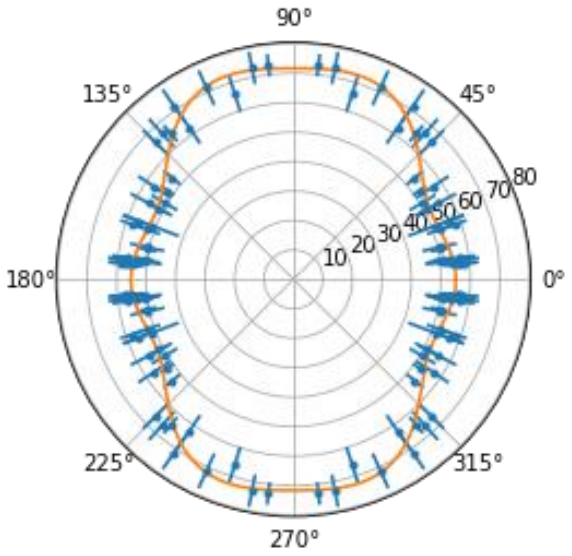

Figure 69. *Plot of the calculated data in a polar coordinate system, showing the symmetry of elastic modulus of nacre. The blue points are the moduli of each sample, the blue line is the corresponding error bar, and the orange curve is the least square method based curve-fitting.*

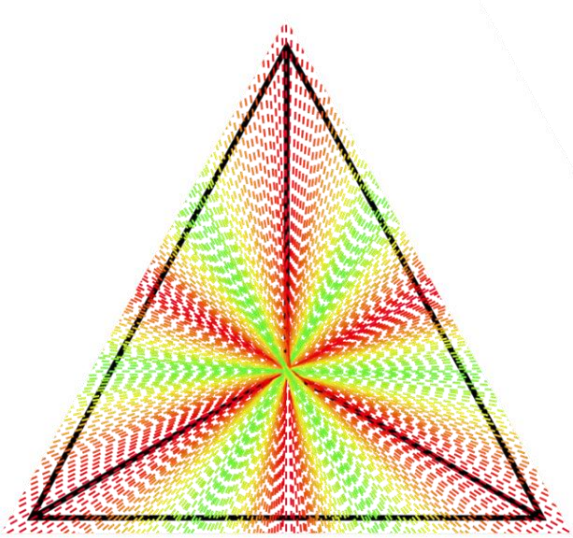

Figure 70. *The symmetry of the alignment between the tablet line and the Berkovich nanoindenter tip. The black in the schematic represents the nanoindentation impression. The multi-color dash lines show the symmetry of the Berkovich tip when it is aligned with the fixed line, i.e. the tablets' line.*

A point need to be paid attention from the **Figure 68** is the modulus of the sample tested with various orientation. As what was mentioned above, some of those samples were tested in the same small area for several times as they were rotated. And, each of the three edges of the indenter tip forms an angel with the tablets line on the sample surface. Based on the symmetry of the Berkvoich tip, there should be a mirror plane symmetry at 30º and a repeat symmetry every 60º for the alignment between the tip and the tablets line. This symmetry is represented by **Figure 70**. In this , the smallest angle among the ones formed by the tip edges and tablets line is named as the "Rotation Angle" in this dissertation. **Figure 71** shows the SEM images of the 4 times tests with different rotation angle applied on one sample within the same area which has the tablets inclination angle of 12.42º. The rotation angle of each time test and the corresponding elastic modulus are marked on the SEM image (**Figure 71**).

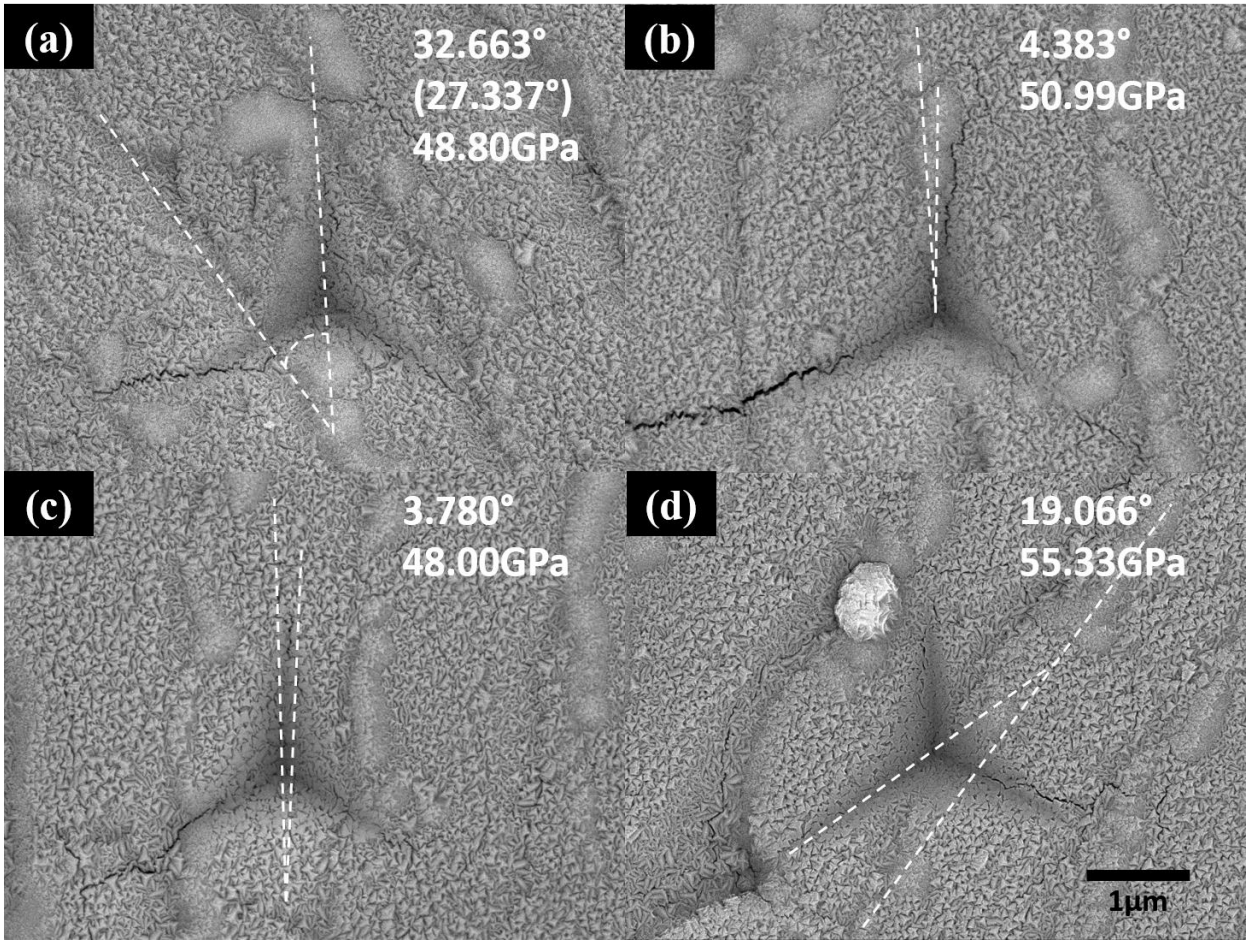

Figure 71. *The sample which shows a tablet inclination angle of 12.42º was tested for different rotation. The rotation angle is the one formed by the tablets line and one of the three edges of the triangle.*

The nanoindentation results indicate that there is a direct modulus value transition when the tablet inclination angle gradually changes from 0º to 90º, and the modulus is mainly distributed in two distinct levels. To analyze this behavior, the tested modulus values need to be combined with the SEM images to show the behavior of the structure under the nanoindentations. Thus, FIB is applied on more samples to show the underneath structure behavior.

For the sample with a low tablet inclination angle, some wide and distinguishable gaps between adjacent tablets in the same layer could be observed remaining in the stressed area (**Figure 72 (b)**, red circled area). These are similar gaps to the ones that were shown by the nacre samples under tensile testing [25][91]. The gap indicates a possible deformation mechanism for the nacre that occurs when the force is applied on the top side known as tablet sliding. In fact, this is believed to be the main stress behavior of nacre when a load is applied. Many published researches have talked about the relation between the tablets sliding and the asperities on the surface of tablets and how this relation enhances the toughness of nacre [46][92-93]. During the loading process, some of the tablets in the stressed area are separated from each other through tablet sliding. During the unloading, some of these separations are reversible and the tablets slide back to the original position or partially slide back while, some of them become permanent separation, which might be caused by the organic matrix fracture which would prevent the tablets from sliding back anymore. Thus, the tested modulus in this direction might be more dependent on the amount of irreversible tablet sliding.

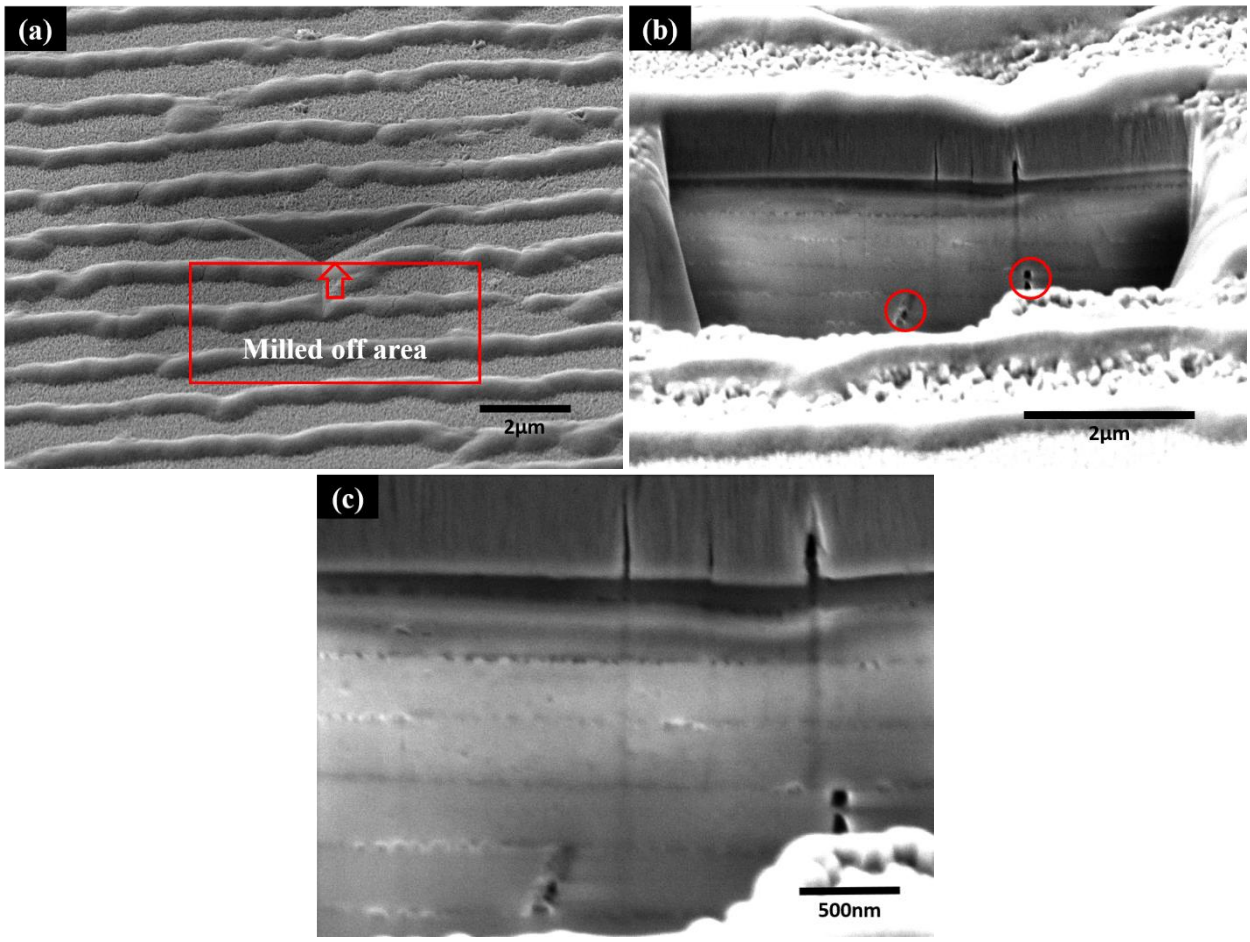

Figure 72*. FIB was applied on a nanoindentation on a top side nacre sample which was sputtered with 831nm Cr film. (a) Part of the material of the nanoindentation was milled, and SEM images were taken along the direction shown by the red arrow. (b) The SEM image of the structure under the nanoindentation and the inner layer tablets gap is shown. (c) The same location with (b) while the image was taken at a higher magnification.*

For the samples with a high inclination angle, i.e. the cross-section samples, some different phenomena begin to appear (**Figure 73**). In one milled sample, a crack was observed which may have been caused by the compresion (**Figure 73 (a)**, red circle). In another sample, a wider and deeper gap was milled to collect more information about how the tablets behave when the force is applied along the interface between tablets layers (**Figure 73 (b)**). In **Figure 73 (b)**, the red circled

area is the stress location caused by the nanoindentation test, and the blue circled areas are sights away from the nanoindentation zone. It should be noticed that in the blue circled areas, the small spaces between each tablet layers is distinguishable as the polymer matrix might have shrunk due to dehydratation. However, in the red circled area, that space is distinctively not as clear as these shown in the blue circled areas and the area below the red circled area. This may indicate that the space is filled with the tablet material. The possibility exists that the tablets extend when a compressive force is applied in the perpendicular direction. At the same time, since there are multiple tablets stacked near one another in a test area, the expansion of one tablet will be resisted by an adjacent expanding tablet. The expansion becomes the permnant deformation and the visible gap is partly eliminated. A schematic could help with describing this deformation in a more clear way (**Figure 74**). As this deformation process depends more on the property of aragonite tablets than the orientation direction, i.e. when the test was applied on the top side sample, it is reasonable to say that the modulus tested on the cross-section side of the nacre sample is closer to the single crystal aragonite than the modulus tested on the top side.

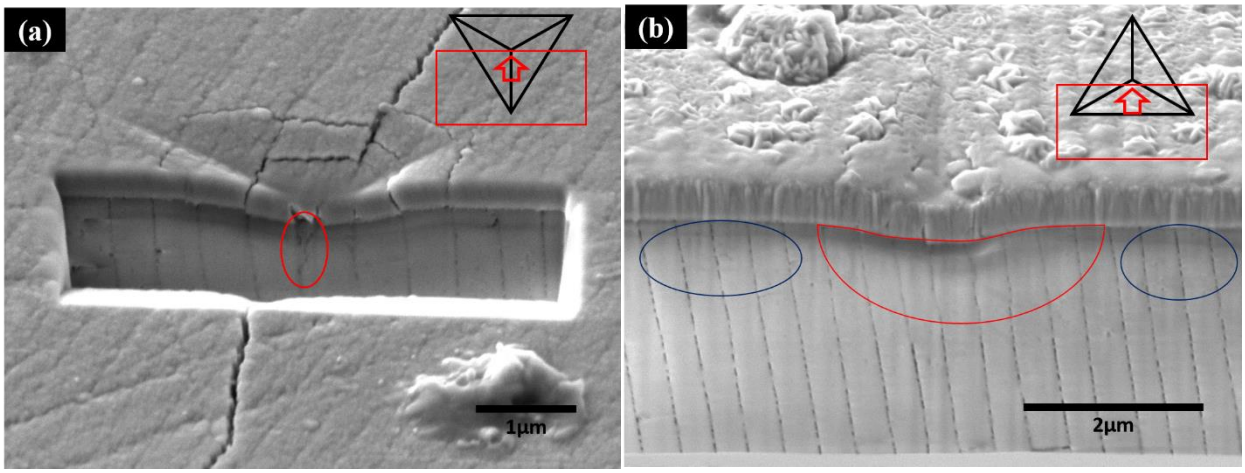

Figure 73*. SEM images of two nanoindentations. These two are on two different cross-section side samples which were milled by FIB. Some distinctive deformations can be seen.*

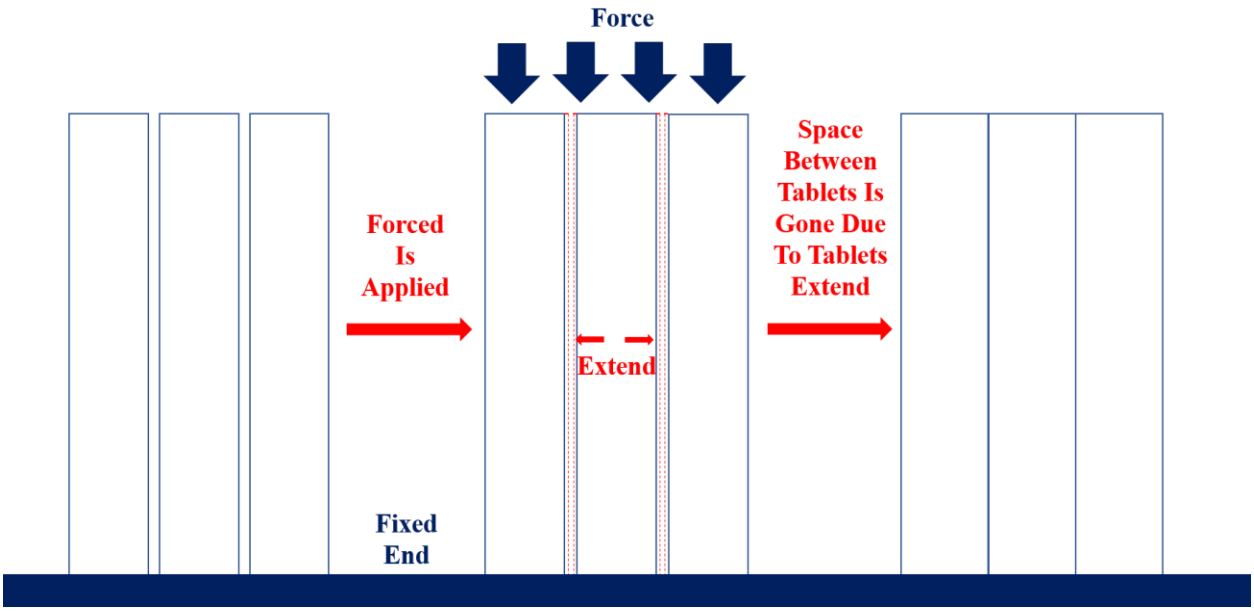

Figure 74*. A simplified schematic describing the possible deformations caused by tablet expansion under a compressive force along the interface between different tablet layers.*

In addition, the loading-unloading curve of the tests applied on the top side and cross-section side sample were compared with each other. One example of the comparison is shown in **Figure 75**. Both the top side and cross-section side sample included here were sputtered with 459nm Cr film and the nanoindentation depth is 800nm. There were 25 nanoindentations on each sample, and, the result shows that the amount of the vaild nanoindentation for the top side sample is 13 and for the cross-section sample is 12. The loading-unloading curves in **Figure 75 (a)** show the much more distictive dispersity than the ones in the **Figure 75 (b)**. This phenonmon was repeated for all the comparison experiments. And, this comparison matches with the assumptions stated above:

- When the force is applied on the top side nacre sample, it is possible that the modulus tends to depend on the amount of the reversible tablets sliding, which is more dispersitive in a wider range among each individual nanoindentation test than a homogenous material.

- When the force is applied on the cross-section side nacre sample, the possibility is that the tested modulus tends to be determined by the material of the aragonite tablet itself, which is expected to be uniform among those tests of each nanoindentations.

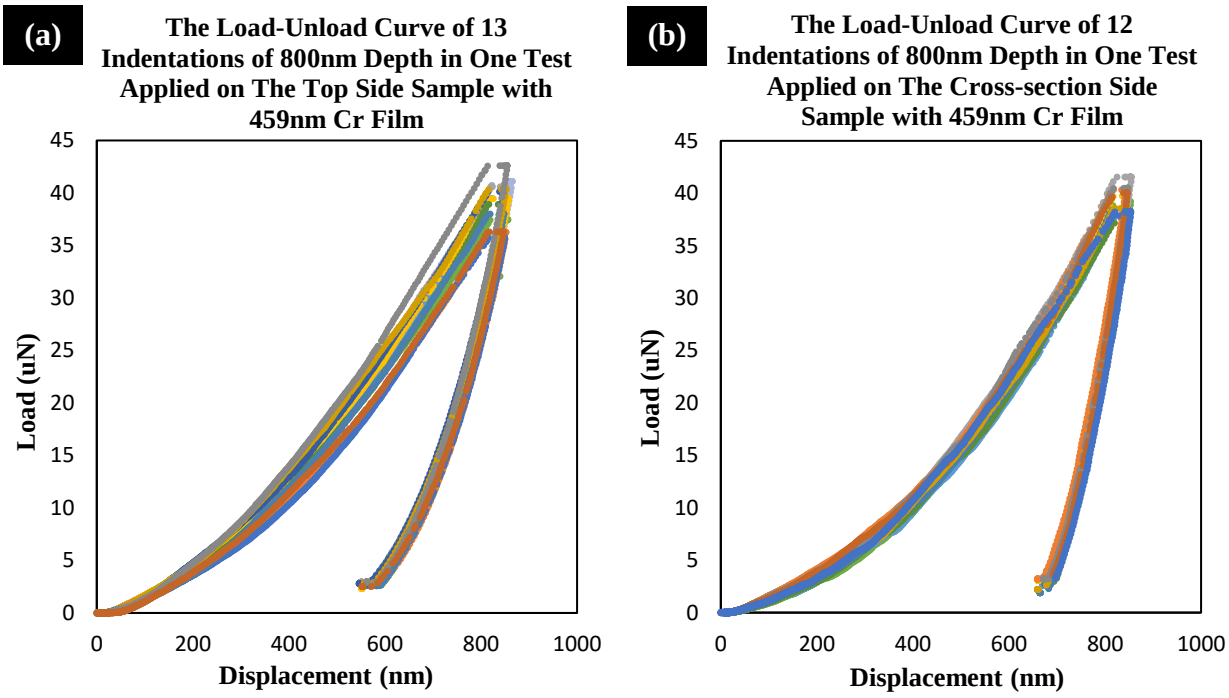

Figure 75. *The loading-unloading curve of the 800nm nanoindentation tests applied on the top side and cross-section side nacre samples which were sputtered with 459nm Cr film.*

As a conclusion, based on all the observations, a posibile explination for the anisotropic modulus of nacre may be due to different mechanism dominating the deformation when a force is applied in different directions.

3.2.4.4 Phenomenon Observed During Nacre Bending

More evidence is needed to support the assumptions developed above. A 3-point bending experiment was applied to a nacre beam sample, in order to identify if the tablet sliding is reversible. As it is difficult to have the nacre to be prepared into a beam with the size capable to

the normal 3-point bending test, a simple size-fitting 3-point bending device was manufactured (**Figure 76**). It should be mentioned that this device was only used for qualitative experiments.

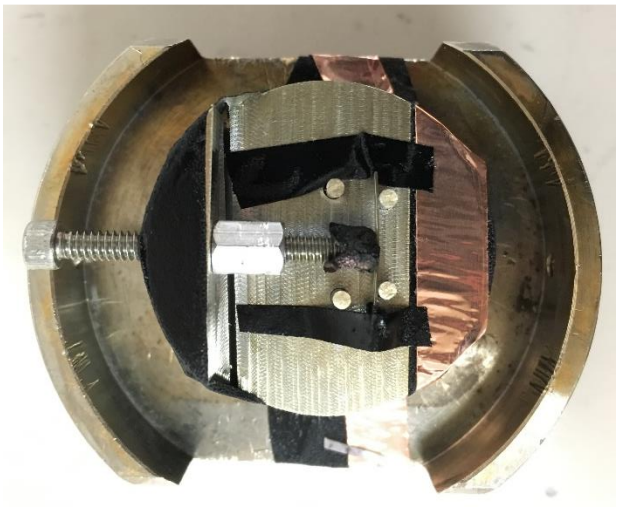

Figure 76*. The device used for the 3-point bending test for the nacre beam.*

The sample preparation can be described by the schematic (**Figure 77**). The nacre was grinded into very thin slices (thickness is 300-600μm), and the cross-section of these slides was polished thoroughly. Next, the slides were separated with a utility knife into a strip. The width of this strip was in the range of 300-500μm and the polished surface is the one that would be observed by using SEM. These strips were then used as the nacre beam for the beam bending experiment.

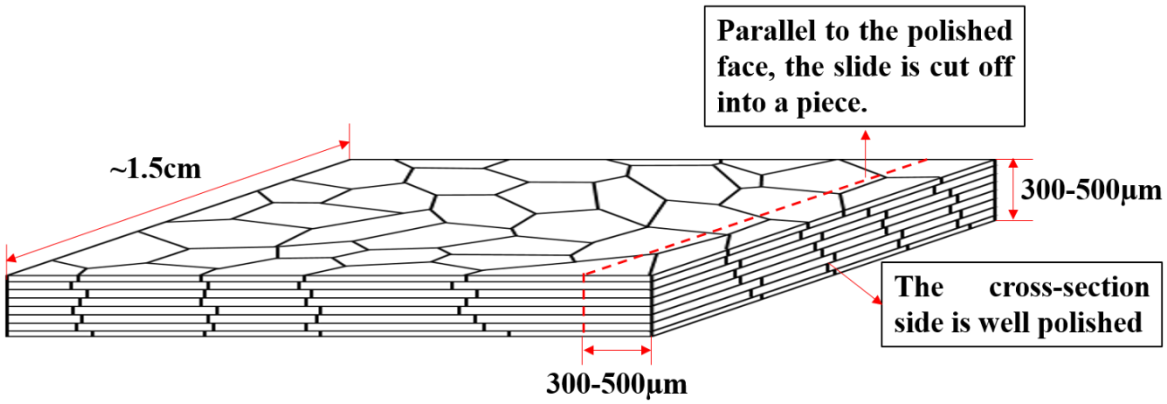

Figure 77*. A schematic describing the nacre beam preparation and sample dimension.*

The nacre beam was loaded into the device and the polished face was kept facing upwards. Then, the screw was turned clock-wise to apply a load on the nacre beam, causing it to bend. This loading process needed to be performed very carefully, as it was quite easy to cause the beam to reach failure. When the nacre beam was under a bent condition, the device was placed into the SEM for characterization.

The nacre beam was first bent slightly. By measuring with the SEM, the distance between the highest point and lowest point of the bent beam was 506.25μm (**Figure 78 (a)**). After taking some SEM images, the sample was taken out and bent to a higher degree. The distance between the highest point and lowest point of the bent beam approached 703.13μm (**Figure 78 (b)**). After taking SEM images under this bending condition, the nacre beam was released and SEM images were also taken for the microstructure of the released beam.

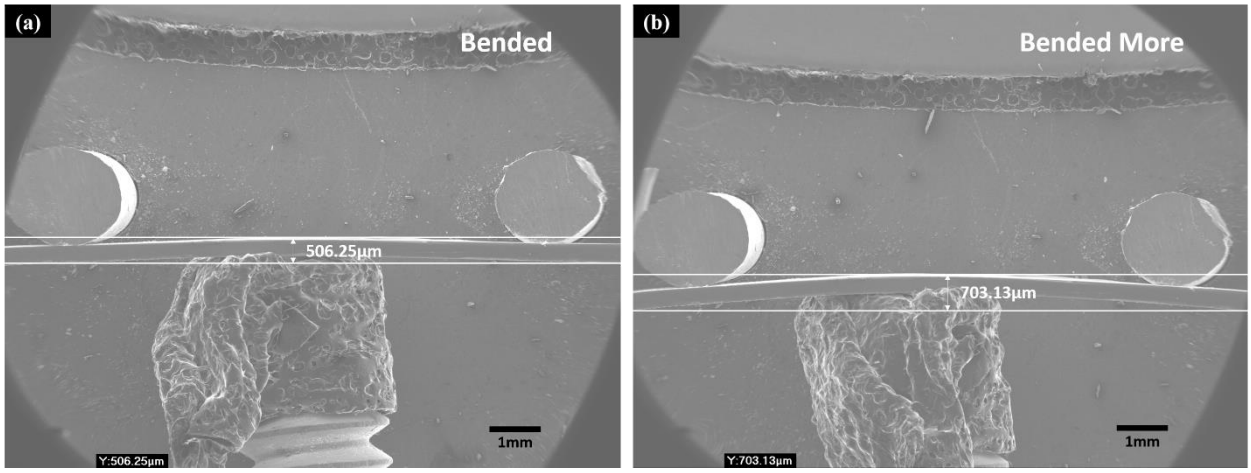

Figure 78*. The nacre beam was bent by the device to different degrees. The maximum bending displacement of (a) the 1st bending was 506.25μm and (b) the 2nd bending was 703.13μm.*

When the nacre beam was bend into the condition shown by **Figure 78 (b)**, the separation among the inner layer tablets could be observed widely distributed around the top part of the beam (**Figure**

79). Those separations are distinguishable by the bright contrast. Then, SEM images taken at the same location under the different bending conditions and the released condition are depicted in **Figure 80** alongside one another for comparison. Some local dirt spots are circled with multiple colors in these images. These dirt spots were helpful in confirming that the images were taken at the exactly the same location. As there are still some slight imperfections to this 3-points bending device, the beam sample was tilted a little when the load is released. Thus, although the SEM image taken for the released beam (**Figure 80 (c)**) were taken under the same magnification as these in **Figure 80 (a)** and **(b)**, the area shown in the image is slightly different. The white squared area in **Figure 80 (c)** is the same location that is shown in **Figure 80 (a)** and **(b)**.

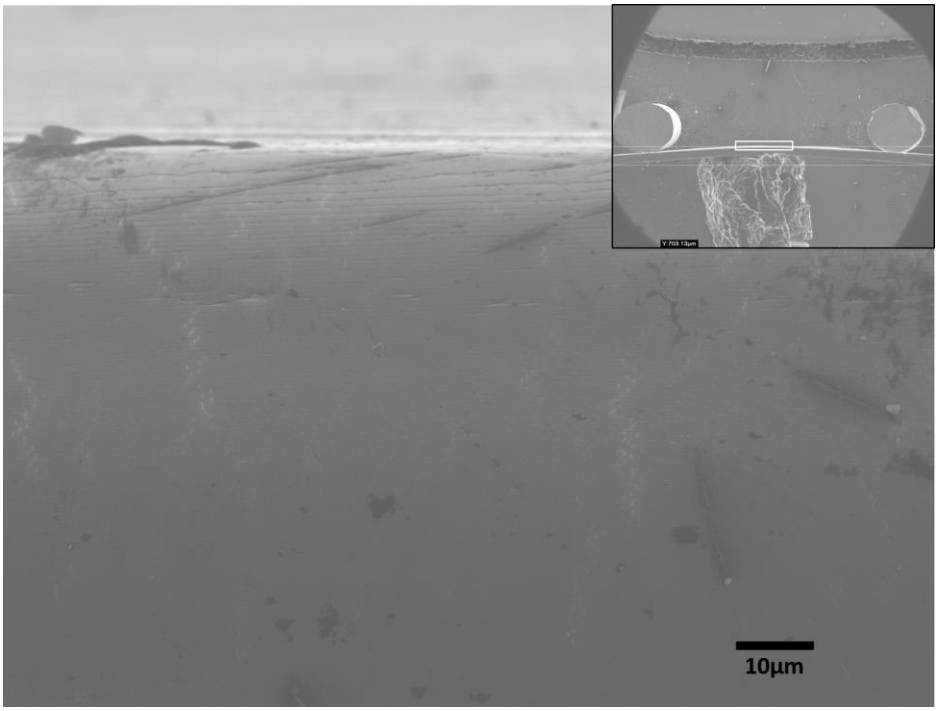

Figure 79. *The tablets sliding distributed widely around the top part of the bended nacre beam.*

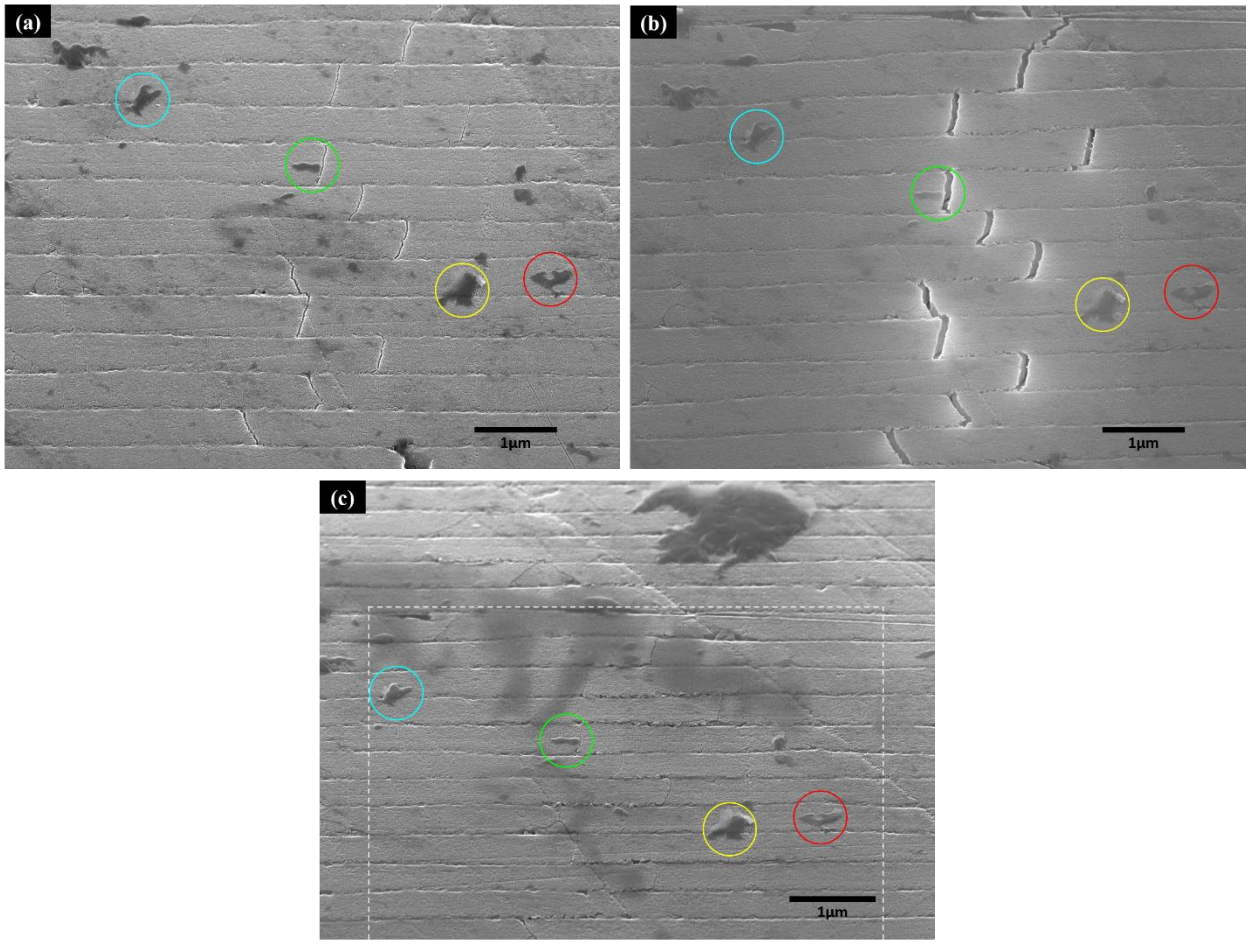

Figure 80. *SEM images were taken for the same sample at the same location under the condition of (a) 506.25µm maximum displacement bending, (b) 703.13µm maximum displacement bending, and (c) released.*

Those SEM images indicate the reversible tablet sliding. **Figure 80** shows that, when the maximum bending displacement is increased, i.e. the nacre beam is bent more, the gap between tablets expands. Upon releasing, the gap has almost disappeared, which indicates a degree of reversibility exits. The positions for the previously observed gaps are still distinguishable due to some permanent changes being produced.

In another sample, the low magnification SEM image for the bent and released beam were taken (**Figure 81**). The permanent deformation could be distinguished even at low magnifications. After releasing the sample, some residual displacement could still be observed. SEM images were taken at the exact same location for the bent and released scenarios (**Figure 82**). The location shown in **Figure 82 (a)** and **(b)** was determined to be the same by comparing the location details within the area.

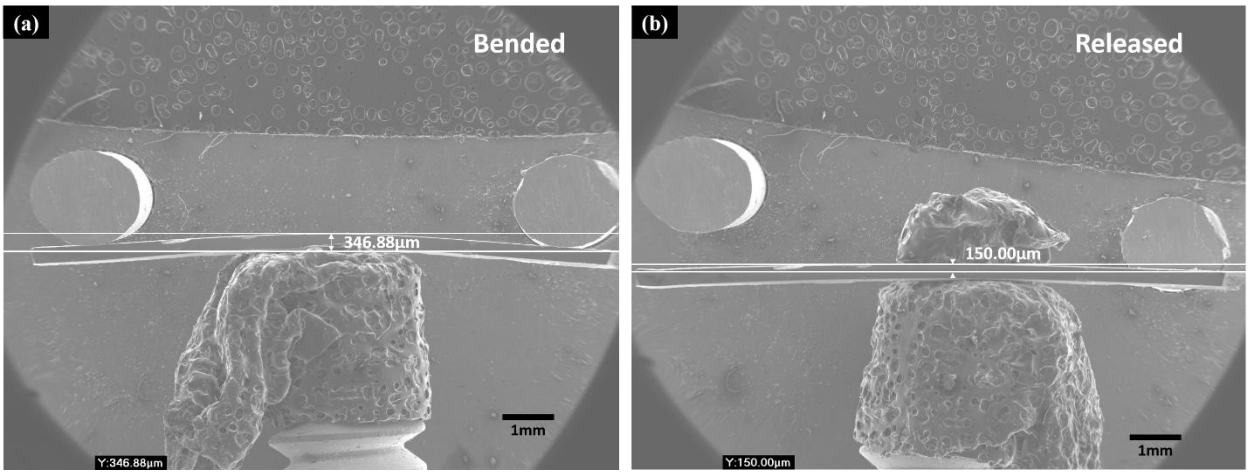

Figure 81*. The SEM images were taken for another sample when it is (a) bent and (b) released.*

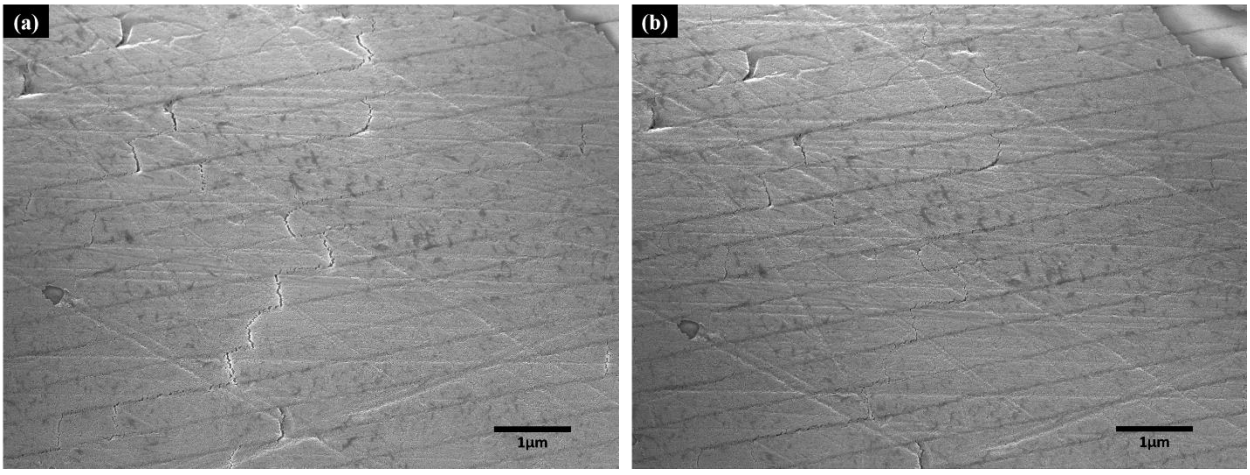

Figure 82*. The SEM images taken for the same location for the (a) bent and (b) released cases at a high magnification.*

By comparing the gap caused by tablet sliding shown by **Figure 81 (b)** and **Figure 82 (a)**, it can be seen that the gaps shown by **Figure 80 (b)** are wider than the ones shown in **Figure 82 (a)** with a comparable amount of bending displacement. A key difference between these two bending experiments is that the samples used in these two experiments were collected from two different individuals. The high magnification SEM images (**Figure 80** and **Figure 82**) indicate that the tablet inclination angle to the sample surface is different. The different tablet inclination angle might be the cause of the different sizes in gaps caused by the tablet sliding, and that the different observed locations could also show a different sliding gap.

These are only the initial attempts for the bending test for nacre. There are many challenges to be solved which will improve this experimental process. For example, with that simple 3-points bending device (**Figure 76**), it is difficult to have the before-bending image of the location shown in **Figure 80** as the sliding area is unknown before it is observed. Also, the bending displacement cannot be easily controlled with the simple mechanism. However, this simple bending still shows the reversible tablet sliding mechanism, which supports one of the assumptions of the deformation mechanism described above. For the other assumed deformation mechanism, more supportive evidence is still needed.

3.2.4.5 Conclusions

The high anisotropic elastic property introduced by the special architecture is quite unique. The investigation of the structure and the anisotropic elastic property generated by said structure it is important due to its potential promising applications.

The anisotropy of the elastic modulus of nacre was shown by collecting tested data from various samples with various structure orientations by use of the nanoindentation test. The distribution of

this data indicates that the elastic modulus has a sudden transition when the tablet inclination angle comes to a specific value around 45º. By combining the FIB milling technique and SEM imaging of the structure's behavior beneath the surface, the high anisotropy of the mechanical properties is assumed to be caused by the different deformation mechanisms which dominate under different structural orientations.

The assumptions for explaining the anisotropic elastic property under different structural orientations can be summarized as such:

- When the force is applied on the top side of the nacre, the elastic modulus depends mainly on the degree of the reversible tablet sliding.
- When the force is applied on the cross-section side of nacre, the elastic modulus depends mainly on the aragonite tablet itself and the space between tablets layers, which acts as the limiting factor in the tablets deformation determined by the Poisson's ratio.

The reversible tablet sliding was observed in the 3-point bending experiments applied on the nacre beams. This phenomenon supports the assumption made of the deformation mechanism when the force is applied on the top side of the nacre. For the case of the force being applied on the cross-section side of the nacre, more solid supportive evidence for the assumed mechanism is needed.

By these assumptions based on the observed evidence, the anisotropic elastic properties of nacre can be properly described. This approach may contribute to designing new composite materials with specific application purposes. For example, the reversible tablets sliding could be treated as a mechanism for developing the composite material with shape memory ability. The details of the elastic property of nacre structure inspire more comprehensive applications of nacre-like composite materials.

4. Future Work

The research included in this dissertation is expected to advance the knowledge of the nacre structure. More work may still be performed in order to show the application value of a nacre-like structure.

4.1 Mesolayer Growth

In the nacre and mesolayer growth investigation, more details of the mesolayer structure need to be characterized and the relationship between the outside environment and the isolated nacre growth environment has still yet to be seen.

Although the seawater environment is meant to mimic the natural sea, many differences are still there such as the space, the diversity of species, etc. Thus, more experiments focusing on the artificial environment could be expected to assist with revealing more details about the relationship between the creature and the environment condition. And, as the increasing temperature contributes to the mesolayer growth, the producing of a structure of the nacre with multiple mesolayer could be expected. And, the mechanical properties of the multilayered structure could be investigated.

This relation could not only help with the study of the biomineralization process, but also may provide new ideas for synthesizing composite materials with special properties.

4.2 Mechanical Properties of Nacre and Mesolayer

In the mechanical property of nacre and mesolayer investigation, much more work could be performed. For the mesolayer's elastic property, the cause for the variations in the collected data from test to test requires further exploration, as well as the role that the mesolayer plays in the

whole structure. For the anisotropic properties of nacre, the bent nacre beam inspired a possible new way to test the modulus of nacre by using the nanoindenter:

The elastic and plastic properties of nacre could be explored using a nacre beam prepared in a similar fashion to the ones prepared in the nacre beam bending test. One end of the nacre beam is fixed on the edge of an aluminum puck and a load is applied by the nanoindenter on the free end of the beam (**Figure 83**). A series nanoindentations with different beam length were applied on the beam. The corresponding dynamic stiffness of each beam length were collected and plotted together (**Figure 84**). The dynamic stiffness keeps increasing while the beam length decreasing.

In **Figure 84**, the average value of dynamic stiffness after 2000nm is treated as the stiffness of the corresponding beam length. As the nacre is built by the countless tablets and the tablets sliding was observed during the nacre bending, Timoshenko beam theory (**Equation 9**) should be applied here to analyze the data due to the consideration of the shear modulus [94]. By applying the boundary condition of the cantilever, the relation between the stiffness and beam length could be simplified into **Equation 10**. Based on the **Equation 10**, the data collected from the tests with different beam length of one sample is used for fitting the relation between the reciprocal of stiffness and the beam length.

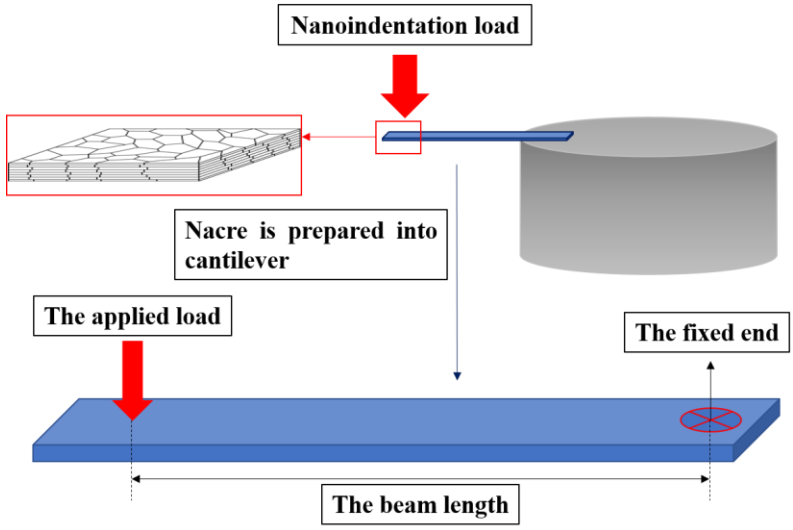

Figure 83*. One end of the nacre beam is fixed on an aluminum puck to be used as a cantilever beam. The nanoindentation load is applied on the free end.*

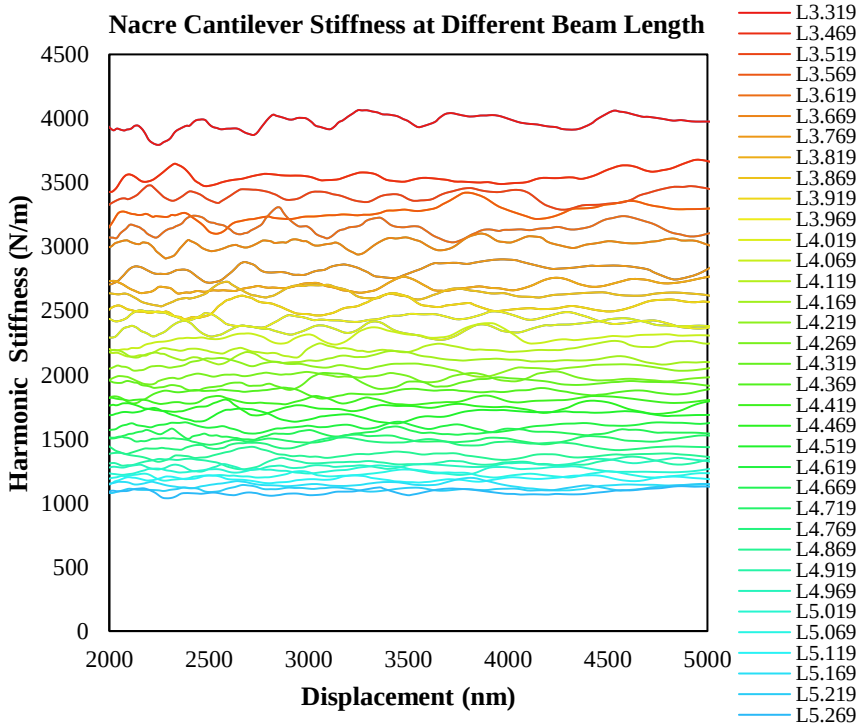

Figure 84. *The dynamic stiffness of the nacre cantilever beam with different beam length collected from the loading process by using the nanoindenter. The legend shows the beam length of each curve and the unite of beam length is mm.*

$$w(x) = \frac{P(L - x)}{\kappa AG} - \frac{Px}{2EI}\left(L^2 - \frac{x^2}{3}\right) + \frac{PL^3}{3EI}$$

Equation 9. *w – Beam deflection, P – Load, L – Complete beam length, A – Cross-section area, G – Shear modulus, E– Elastic modulus, I – The second moment of area, x – The location of the load (free end of the beam: x=0; constrained end of the beam: x = L), κ – The Timoshenko shear coefficient (κ =5/6 for the rectangular cross-section beam).*

$$\frac{1}{s} = \frac{L}{\kappa AG} + \frac{L^3}{3EI}$$

Equation 10. *s – The stiffness, L – Complete beam length, A – Cross-section area, G – Shear modulus, E– Elastic modulus, I – The second moment of area.*

Both the top side and cross-section side type of beams were tested in this way. A series tests with various beam length were applied on those two beams and the data was curve fitted based on **Equation 10** (**Figure 85**). And, the corresponding curve-fitting functions are listed in **Table 10**. By matching the teams in the functions with the **Equation 10**, the elastic modulus could be calculated.

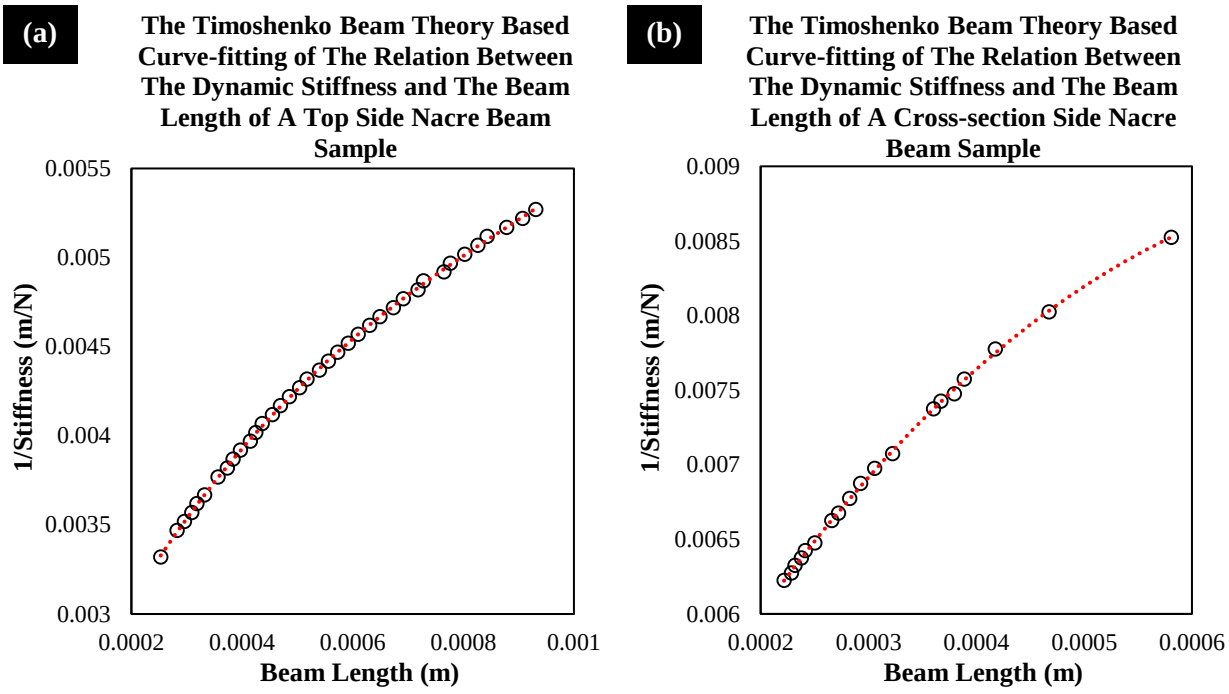

Figure 85. *The relation between the reciprocal of stiffness and the beam length of both (a) top side sample and (b) cross-section side sample is curve fitted through the Timoshenko beam theory.*

Sample Type	The Dimension of The Cross-section of The Beam	The Function Obtained by The Curve-fitting	Elastic Modulus (GPa)
Top side Beam	Width(b) - 596.25μm Thickness(h) - 299.11μm	$\frac{1}{s} = 1.0752\times10^{-2}\mathrm{L} + 5.9039\times10^{3}\mathrm{L}^{3}$	42.46
Cross-section Beam	Width(b) - 358.009μm Thickness(h) - 529.616μm	$\frac{1}{s} = 1.3884\times10^{-3}L + 8.8049\times10^{2}L^{3}$	85.42

Table 10. *The dimension of the involved beams and the Timoshenko beam theory based curve-fitting of the data of the corresponding beams.*

The elastic modulus collected from this test matches with the results obtained from the nanoindentation tests. However, there are still many deficiencies. And, many improvements are

expected such as the consideration of the tablets inclination angle. Besides, the accuracy of the beam dimension, the permanent deformation, etc. are all need to be considered and discussed. In additional, the strength of the organic matrix in the nacre structure could be quantitively determined by applying the bending and cantilever experiments on the nacre samples to the failure.

The hydration condition of the nacre is another concern. So far, most of the experiments included in this research focus on the dehydrated nacre. With the organic composition, the change of the mechanical property could be expected when the nacre is hydrated. However, as the nacre is a natural material with too many variables, some technique problems need to be solved to approach that future work.

The biomineralization process and the extremely fine structure with unique properties produced by it is being studied extensively as there are still many secrets yet to be revealed, and thus the future holds promise for a wider range of applications to be discovered for this material.

5. References

[1] Whitesides, G. M., & Grzybowski, B. (2002). Self-assembly at all scales. *Science*, *295*(5564), 2418-2421.

[2] Yin, Y., Lu, Y., Gates, B., & Xia, Y. (2001). Template-assisted self-assembly: a practical route to complex aggregates of monodispersed colloids with well-defined sizes, shapes, and structures. *Journal of the American Chemical Society*, *123*(36), 8718-8729.

[3] Meng, Q. B., Fu, C. H., Einaga, Y., Gu, Z. Z., Fujishima, A., & Sato, O. (2002). Assembly of highly ordered three-dimensional porous structure with nanocrystalline TiO_2 semiconductors. *Chemistry of Materials*, *14*(1), 83-88. DOI: 10.1021/cm0101576

[4] Kuang, D., Brillet, J., Chen, P., Takata, M., Uchida, S., Miura, H., ... & Grätzel, M. (2008). Application of highly ordered TiO_2 nanotube arrays in flexible dye-sensitized solar cells. *ACS nano*, *2*(6), 1113-1116.

[5] Simard, M., Su, D., & Wuest, J. D. (1991). Use of hydrogen bonds to control molecular aggregation. Self-assembly of three-dimensional networks with large chambers. *Journal of the American Chemical Society*, *113*(12), 4696-4698.

[6] Bigioni, T. P., Lin, X. M., Nguyen, T. T., Corwin, E. I., Witten, T. A., & Jaeger, H. M. (2006). Kinetically driven self-assembly of highly ordered nanoparticle monolayers. *Nature materials*, *5*(4), 265-270.

[7] Hu, G., Ma, D., Cheng, M., Liu, L., & Bao, X. (2002). Direct synthesis of uniform hollow carbon spheres by a self-assembly template approach. *Chemical Communications*, (17), 1948-1949.

[8] Maune, H. T., Han, S. P., Barish, R. D., Bockrath, M., Goddard III, W. A., Rothemund, P. W., & Winfree, E. (2010). Self-assembly of carbon nanotubes into two-dimensional geometries using DNA origami templates. *Nature nanotechnology*, *5*(1), 61-66.

[9] Zhukov, A. A., Goncharov, A. V., de Groot, P. A. J., Bartlett, P. N., & Ghanem, M. A. (2003). Magnetic antidot arrays from self-assembly template methods. *Journal of applied physics*, *93*(10), 7322-7324.

[10] Wang, D., & Möhwald, H. (2004). Template-directed colloidal self-assembly–the route to 'top-down'nanochemical engineering. *Journal of Materials Chemistry*, *14*(4), 459-468.

[11] Zeng, H., Li, J., Liu, J. P., Wang, Z. L., & Sun, S. (2002). Exchange-coupled nanocomposite magnets by nanoparticle self-assembly. *Nature*, *420*(6914), 395-398.

[12] Habibi, Y., Lucia, L. A., & Rojas, O. J. (2010). Cellulose nanocrystals: chemistry, self-assembly, and applications. *Chemical reviews*, *110*(6), 3479-3500.

[13] Alexandridis, P., & Lindman, B. (2000). *Amphiphilic block copolymers: self-assembly and applications*. Elsevier.

[14] Schaeferling, M., Schiller, S., Paul, H., Kruschina, M., Pavlickova, P., Meerkamp, M., ... & Kambhampati, D. (2002). Application of self-assembly techniques in the design of biocompatible protein microarray surfaces. *Electrophoresis*, *23*(18), 3097-3105.

[15] Cartwright, J. H., & Checa, A. G. (2007). The dynamics of nacre self-assembly. *Journal of the Royal Society Interface*, *4*(14), 491-504.

[16] Meldrum, F. C., & Cölfen, H. (2008). Controlling mineral morphologies and structures in biological and synthetic systems. *Chemical reviews*, *108*(11), 4332-4432.

[17] Falini, G., Albeck, S., Weiner, S., & Addadi, L. (1996). Control of aragonite or calcite polymorphism by mollusk shell macromolecules. *Science*, *271*(5245), 67.

[18] Heinemann, F., Launspach, M., Gries, K., & Fritz, M. (2011). Gastropod nacre: structure, properties and growth—biological, chemical and physical basics. *Biophysical chemistry*, *153*(2), 126-153.

[19] Weiner, S., Traub, W., & Parker, S. B. (1984). Macromolecules in mollusc shells and their functions in biomineralization. *Philosophical Transactions of the Royal Society of London B: Biological Sciences*, *304*(1121), 425-434.

[20] Kumar, M. N. R. (2000). A review of chitin and chitosan applications. *Reactive and functional polymers*, *46*(1), 1-27.

[21] Milton, G. W. (1992). Composite materials with Poisson's ratios close to—1. *Journal of the Mechanics and Physics of Solids*, *40*(5), 1105-1137.

[22] Parkhouse J. G. (1984). Structuring a process of material dilution. *In Proceedings of 3rd International Conference on Space Structures (Ed. Nooshin H.)*, 367–374.

[23] Lakes, R. (1991). Experimental micro mechanics methods for conventional and negative Poisson's ratio cellular solids as Cosserat continua. *ASME, Transactions, Journal of Engineering Materials and Technology*, *113*, 148-155.

[24] Lakes, R. (1993). Materials with structural hierarchy. *Nature*, *361*(6412), 511-515.

[25] Sun, J., & Bhushan, B. (2012). Hierarchical structure and mechanical properties of nacre: a review. *Rsc Advances*, *2*(20), 7617-7632.

[26] Evans, A. G., Suo, Z., Wang, R. Z., Aksay, I. A., He, M. Y., & Hutchinson, J. W. (2001).

Model for the robust mechanical behavior of nacre. *Journal of Materials Research*, *16*(09), 2475-2484.

[27] Espinosa, H. D., Juster, A. L., Latourte, F. J., Loh, O. Y., Gregoire, D., & Zavattieri, P. D. (2011). Tablet-level origin of toughening in abalone shells and translation to synthetic composite materials. *Nature communications*, *2*, 173.

[28] López, M. I., & Meyers, M. A. (2016). The organic interlamellar layer in abalone nacre: formation and mechanical response. *Materials Science and Engineering: C*, *58*, 7-13.

[29] Greenfield, E. M., Wilson, D. C., & Crenshaw, M. A. (1984). Ionotropic nucleation of calcium carbonate by molluscan matrix. *American Zoologist*, *24*(4), 925-932.

[30] Wheeler, A. P., & Sikes, C. S. (1984). Regulation of carbonate calcification by organic matrix. *American Zoologist*, *24*(4), 933-944.

[31] Smith, B. L., Schäffer, T. E., Viani, M., Thompson, J. B., Frederick, N. A., Kindt, J., ... & Hansma, P. K. (1999). Molecular mechanistic origin of the toughness of natural adhesives, fibres and composites. *Nature*, *399*(6738), 761-763.

[32] Song, F., Soh, A. K., & Bai, Y. L. (2003). Structural and mechanical properties of the organic matrix layers of nacre. *Biomaterials*, *24*(20), 3623-3631.

[33] Cölfen, H., & Mann, S. (2003). Higher-order organization by mesoscale self-assembly and transformation of hybrid nanostructures. *Angewandte Chemie International Edition*, 42(21), 2350-2365.

[34] Weiner, S., & Hood, L. (1975). Soluble protein of the organic matrix of mollusk shells: a potential template for shell formation. *Science*, *190*(4218), 987-989.

[35] Belcher, A. M., Wu, X. H., Christensen, R. J., & Hansma, P. K. (1996). Control of crystal phase switching and orientation by soluble mollusc-shell proteins. *Nature*, *381*(6577), 56.

[36] Thompson, J. B., Paloczi, G. T., Kindt, J. H., Michenfelder, M., Smith, B. L., Stucky, G., ... & Hansma, P. K. (2000). Direct observation of the transition from calcite to aragonite growth as induced by abalone shell proteins. *Biophysical Journal*, *79*(6), 3307-3312.

[37] Nudelman, F., Gotliv, B. A., Addadi, L., & Weiner, S. (2006). Mollusk shell formation: mapping the distribution of organic matrix components underlying a single aragonitic tablet in nacre. *Journal of structural biology*, *153*(2), 176-187.

[38] Cölfen, H., & Antonietti, M. (2005). Mesocrystals: inorganic superstructures made by highly parallel crystallization and controlled alignment. *Angewandte Chemie International Edition*, *44*(35), 5576-5591.

[39] Cölfen, H. (2006). Bio-inspired mineralization using hydrophilic polymers. *In Biomineralization II* (pp. 1-77). Springer Berlin Heidelberg.

[40] Currey, J. D., & Taylor, J. D. (1974). The mechanical behaviour of some molluscan hard tissues. Journal of Zoology, 173(3), 395-406.

[41] Currey, J. D. (1977). Mechanical properties of mother of pearl in tension. *Proceedings of the Royal Society of London B: Biological Sciences*, *196*(1125), 443-463.

[42] Wang, R. Z., Suo, Z., Evans, A. G., Yao, N., & Aksay, I. A. (2001). Deformation mechanisms in nacre. *Journal of Materials Research*, *16*(09), 2485-2493.

[43] Jackson, A. P., Vincent, J. F. V., & Turner, R. M. (1988). The mechanical design of

nacre. *Proceedings of the Royal Society of London B: Biological Sciences*, *234*(1277), 415-440.

[44] Sullivan, M., & Prorok, B. C. (2015). Controlling abalone shell architecture with temperature. In *Mechanics of Biological Systems and Materials, Volume 7* (pp. 27-31). Springer, Cham.

[45] Bruet, B. J. F., Qi, H. J., Boyce, M. C., Panas, R., Tai, K., Frick, L., & Ortiz, C. (2005). Nanoscale morphology and indentation of individual nacre tablets from the gastropod mollusc Trochus niloticus. *Journal of Materials Research*, *20*(09), 2400-2419.

[46] Menig, R., Meyers, M. H., Meyers, M. A., & Vecchio, K. S. (2000). Quasi-static and dynamic mechanical response of Haliotis rufescens (abalone) shells. *Acta Materialia*, *48*(9), 2383-2398.

[47] Barthelat, F., & Espinosa, H. D. (2007). An experimental investigation of deformation and fracture of nacre–mother of pearl. *Experimental mechanics*, *47*(3), 311-324.

[48] Barthelat, F., Li, C. M., Comi, C., & Espinosa, H. D. (2006). Mechanical properties of nacre constituents and their impact on mechanical performance. *Journal of Materials Research*, 21(8), 1977-1986.

[49] Sun, J. Y., & Tong, J. (2007). Fracture toughness properties of three different biomaterials measured by nanoindentation. *Journal of Bionic Engineering*, 4(1), 11-17.

[50] Lin, A. Y. M., Meyers, M. A., & Vecchio, K. S. (2006). Mechanical properties and structure of Strombus gigas, Tridacna gigas, and Haliotis rufescens sea shells: a comparative study. *Materials Science and Engineering: C*, 26(8), 1380-1389.

[51] Kearney, C., Zhao, Z., Bruet, B. J. F., Radovitzky, R., Boyce, M. C., & Ortiz, C. (2006).

Nanoscale anisotropic plastic deformation in single crystal aragonite. *Physical review letters*, *96*(25), 255505.

[52] Li, X., Chang, W. C., Chao, Y. J., Wang, R., & Chang, M. (2004). Nanoscale structural and mechanical characterization of a natural nanocomposite material: the shell of red abalone. *Nano letters*, 4(4), 613-617.

[53] Bonderer, L. J., Studart, A. R., & Gauckler, L. J. (2008). Bioinspired design and assembly of platelet reinforced polymer films. *Science*, *319*(5866), 1069-1073.

[54] Lin, A. Y. M., Chen, P. Y., & Meyers, M. A. (2008). The growth of nacre in the abalone shell. Acta Biomaterialia, 4(1), 131-138.

[55] Zaremba, C. M., Belcher, A. M., Fritz, M., Li, Y., Mann, S., Hansma, P. K., ... & Stucky, G. D. (1996). Critical transitions in the biofabrication of abalone shells and flat pearls. *Chemistry of Materials*, *8*(3), 679-690.

[56] Stanley, S. M., & Hardie, L. A. (1998). Secular oscillations in the carbonate mineralogy of reef-building and sediment-producing organisms driven by tectonically forced shifts in seawater chemistry. *Palaeogeography, Palaeoclimatology, Palaeoecology*, *144*(1), 3-19.

[57] Lowenstein, T. K., Timofeeff, M. N., Brennan, S. T., Hardie, L. A., & Demicco, R. V. (2001). Oscillations in Phanerozoic seawater chemistry: Evidence from fluid inclusions. *Science*, *294*(5544), 1086-1088.

[58] Porter, S. M. (2007). Seawater chemistry and early carbonate biomineralization. *Science*, *316*(5829), 1302-1302.

[59] Zhuravlev, A. Y., & Wood, R. A. (2008). Eve of biomineralization: Controls on skeletal mineralogy. *Geology*, *36*(12), 923-926.

[60] Erez, J. (2003). The source of ions for biomineralization in foraminifera and their implications for paleoceanographic proxies. *Reviews in mineralogy and geochemistry*, *54*(1), 115-149.

[61] Toyofuku, T., Kitazato, H., Kawahata, H., Tsuchiya, M., & Nohara, M. (2000). Evaluation of Mg/Ca thermometry in foraminifera: Comparison of experimental results and measurements in nature. *Paleoceanography*, *15*(4), 456-464.

[62] Fritz, M., Belcher, A. M., Radmacher, M., Walters, D. A., Hansma, P. K., Stucky, G. D., ... & Mann, S. (1994). Flat pearls from biofabrication of organized composites on inorganic substrates. *Nature*, *371*(6492), 49-51.

[63] Oliver, W. C., & Pharr, G. M. (1992). An improved technique for determining hardness and elastic modulus using load and displacement sensing indentation experiments. *Journal of materials research*, *7*(6), 1564-1583.

[64] Pharr, G. M., Oliver, W. C., & Brotzen, F. R. (1992). On the generality of the relationship among contact stiffness, contact area, and elastic modulus during indentation. *Journal of materials research*, *7*(3), 613-617.

[65] Simmons, G., & Wang, H. (1971). Single crystal elastic constants and calculated aggregate properties.

[66] Pharr, G. M., & Oliver, W. C. (1992). Measurement of thin film mechanical properties using nanoindentation. *Mrs Bulletin*, *17*(7), 28-33.

[67] King, R. B. (1987). Elastic analysis of some punch problems for a layered medium. *International Journal of Solids and Structures*, *23*(12), 1657-1664.

[68] Doerner, M. F., & Nix, W. D. (1986). A method for interpreting the data from depth-sensing indentation instruments. *Journal of Materials research*, *1*(4), 601-609.

[69] Zhou, B., & Prorok, B. C. (2010). A discontinuous elastic interface transfer model of thin film nanoindentation. *Experimental Mechanics*, *50*(6), 793-801.

[70] Chen, Y., Sullivan, M., Zhang, A., & Prorok, B. C. (2018). A new method to extract elastic modulus of brittle materials from Berkovich indentation. *Journal of the European Ceramic Society*, 38(1), 349-353.

[71] Sellinger, A., Weiss, P. M., Nguyen, A., & Lu, Y. (1998). Continuous self-assembly of organic-inorganic nanocomposite coatings that mimic nacre. *Nature*, *394*(6690), 256.

[72] Podsiadlo, P., Paternel, S., Rouillard, J. M., Zhang, Z., Lee, J., Lee, J. W., ... & Kotov, N. A. (2005). Layer-by-layer assembly of nacre-like nanostructured composites with antimicrobial properties. *Langmuir*, *21*(25), 11915-11921.

[73] Pugno, N. M. (2006). Mimicking nacre with super-nanotubes for producing optimized super-composites. *Nanotechnology*, *17*(21), 5480.

[74] Gao, H. L., Chen, S. M., Mao, L. B., Song, Z. Q., Yao, H. B., Cölfen, H., ... & Ni, Y. (2017). Mass production of bulk artificial nacre with excellent mechanical properties. *Nature Communications*, *8*.

[75] Corni, I., Harvey, T. J., Wharton, J. A., Stokes, K. R., Walsh, F. C., & Wood, R. J. K. (2012). A review of experimental techniques to produce a nacre-like structure. *Bioinspiration & biomimetics*, *7*(3), 031001.

[76] Nassif, N., Pinna, N., Gehrke, N., Antonietti, M., Jäger, C., & Cölfen, H. (2005).

Amorphous layer around aragonite platelets in nacre. *Proceedings of the National Academy of Sciences of the United States of America*, *102*(36), 12653-12655.

[77] Lopez, M. I., Chen, P. Y., McKittrick, J., & Meyers, M. A. (2011). Reprint of: Growth of nacre in abalone: Seasonal and feeding effects. *Materials Science and Engineering: C*, *31*(4), 716-723.

[78] Joubert, C., Linard, C., Le Moullac, G., Soyez, C., Saulnier, D., Teaniniuraitemoana, V., ... & Gueguen, Y. (2014). Temperature and food influence shell growth and mantle gene expression of shell matrix proteins in the pearl oyster Pinctada margaritifera. *PloS one*, *9*(8), e103944.

[79] Melzner, F., Stange, P., Trübenbach, K., Thomsen, J., Casties, I., Panknin, U., ... & Gutowska, M. A. (2011). Food supply and seawater pCO2 impact calcification and internal shell dissolution in the blue mussel Mytilus edulis. *Plos one*, *6*(9), e24223.

[80] Velev, O. D., Lenhoff, A. M., & Kaler, E. W. (2000). A class of microstructured particles through colloidal crystallization. *Science*, *287*(5461), 2240-2243.

[81] Sel, O., Kuang, D., Thommes, M., & Smarsly, B. (2006). Principles of hierarchical meso- and macropore architectures by liquid crystalline and polymer colloid templating. *Langmuir*, *22*(5), 2311-2322.

[82] Zhang, G., & Xu, J. (2013). From colloidal nanoparticles to a single crystal: New insights into the formation of nacre's aragonite tablets. *Journal of structural biology*, *182*(1), 36-43.

[83] Yang, L. J., Lee, C. C., Chen, P. H., & Hsu, C. W. (2011, February). Confined fractal

patterns in gelatin. In *Nano/Micro Engineered and Molecular Systems (NEMS), 2011 IEEE International Conference on* (pp. 49-52). IEEE.

[84] Giri, A., Dutta Choudhury, M., Dutta, T., & Tarafdar, S. (2012). Multifractal growth of crystalline NaCl aggregates in a gelatin medium. *Crystal Growth & Design*, *13*(1), 341-345.

[85] Choudhury, M. D., Dutta, T., & Tarafdar, S. (2015). Growth kinetics of NaCl crystals in a drying drop of gelatin: transition from faceted to dendritic growth. *Soft matter*, *11*(35), 6938-6947.

[86] Li, X., & Bhushan, B. (2000). Development of continuous stiffness measurement technique for composite magnetic tapes. *Scripta materialia*, *42*(10), 929-935.

[87] Wang, Z., Bei, H., George, E. P., & Pharr, G. M. (2011). Influences of surface preparation on nanoindentation pop-in in single-crystal Mo. *Scripta Materialia*, *65*(6), 469-472.

[88] Johnson, K. L. (1982). One hundred years of Hertz contact. *proceedings of the Institution of Mechanical Engineers*, *196*(1), 363-378.

[89] Bei, H., George, E. P., Hay, J. L., & Pharr, G. M. (2005). Influence of indenter tip geometry on elastic deformation during nanoindentation. *Physical Review Letters*, *95*(4), 045501.

[90] Zong, W. J., Wu, D., & He, C. L. (2017). Radius and angle determination of diamond Berkovich indenter. *Measurement*, *104*, 243-252.

[91] Barthelat, F., Tang, H., Zavattieri, P. D., Li, C. M., & Espinosa, H. D. (2007). On the mechanics of mother-of-pearl: a key feature in the material hierarchical structure. *Journal of the Mechanics and Physics of Solids*, *55*(2), 306-337.

[92] Li, X., Xu, Z. H., & Wang, R. (2006). In situ observation of nanograin rotation and deformation in nacre. *Nano letters*, *6*(10), 2301-2304.

[93] Barthelat, F., & Zhu, D. (2011). A novel biomimetic material duplicating the structure and mechanics of natural nacre. *Journal of Materials Research*, *26*(10), 1203-1215.

[94] Gere, J. M., & Timoshenko, S. P. (1997). Mechanics of materials, 1997. *PWS-KENT Publishing Company*, *ISBN 0*, *534*(92174), 4.

6. Publications

- Chen, Y., Sullivan, M., Zhang, A., & Prorok, B. C. (2018). A new method to extract elastic modulus of brittle materials from Berkovich indentation. Journal of the European Ceramic Society, 38(1), 349-353.

- Zhang, A., Chen, Y., Sullivan, M., & Prorok, B. C. (2017). The Growth and Mechanical Properties of Abalone Nacre Mesolayer. In *Mechanics of Biological Systems and Materials, Volume 6* (pp. 143-148). Springer International Publishing.

- Prorok, B., Zhang, A., Chen, Y., & Kristin, F. (2018). The Extended Abstract: The Growth and Mechanical Property of Mesolayer in Abalone Nacre. In *Mechanics of Biological Systems, Materials and other topics in Experimental and Applied Mechanics, Volume 4(pp. 65-69)*. Springer, Cham.

Appendix I. Photos of Those Main Instruments Included

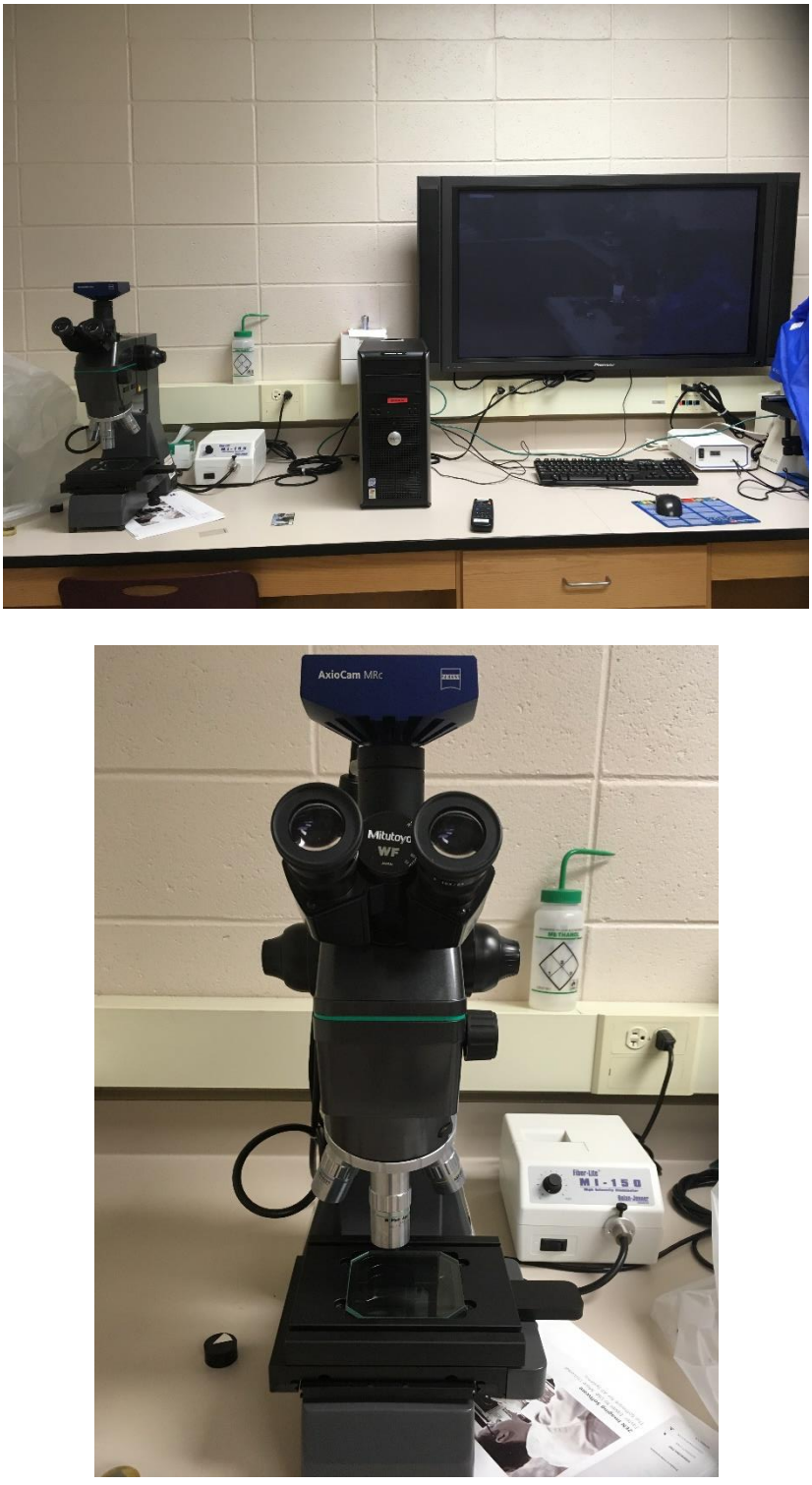

Figure 86. *The Optical Microscope work station and the Mitutoyo Corporation optical microscope.*

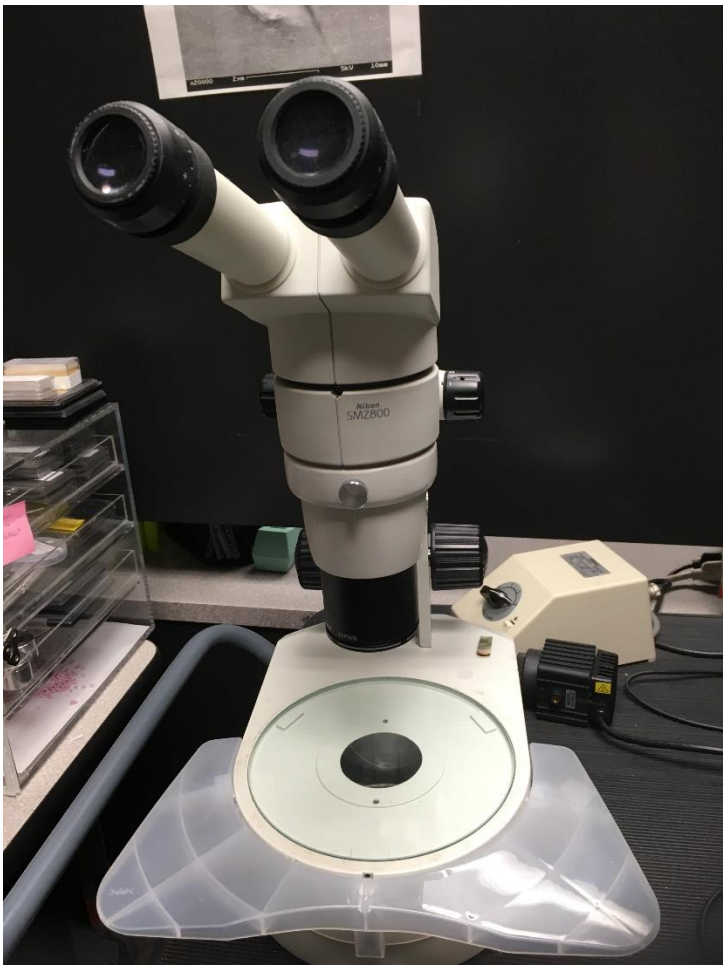

Figure 87. *The Nikon SMZ800 Optical Microscope.*

Figure 88. *The instruments used for grinding (top) and polishing (bottom).*

Figure 89. *The Denton Vacuum, LLC, DISCOVERY 18 Sputter in the clean room.*

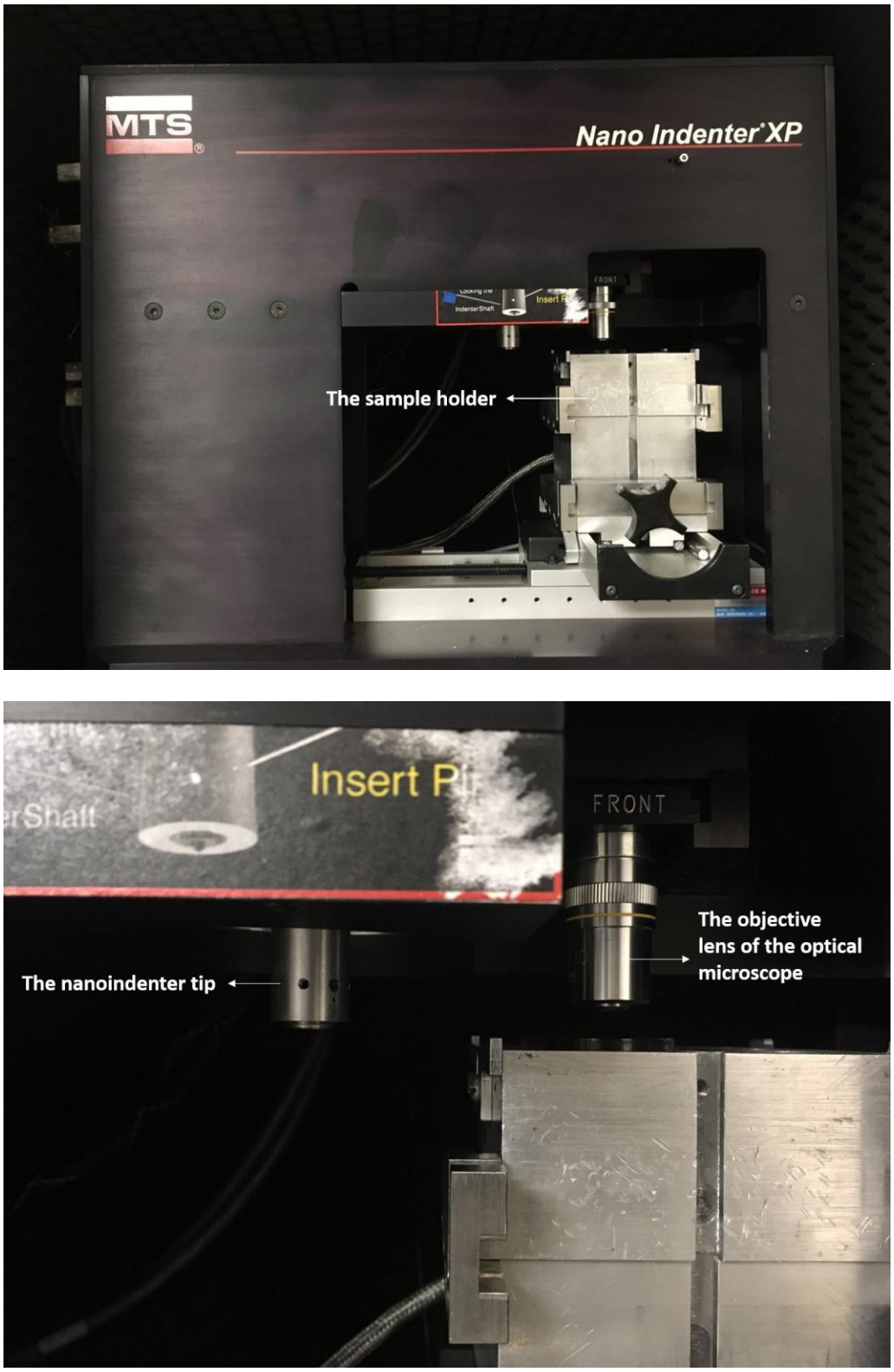

Figure 90. *The MTS Nano Indenter XP included in this research.*

Figure 91. *The Scanning Electron Microscope used in this research (top). The EDS detector shares the same vacuum chamber with the SEM.*

Figure 92. *The Abalone Lab.*